# *Physical, Chemical, & Nano Sciences Center*

# *Research Briefs*

*2005*

**Sandia National Laboratories**
**Albuquerque, New Mexico**

***A Multiprogram Laboratory***

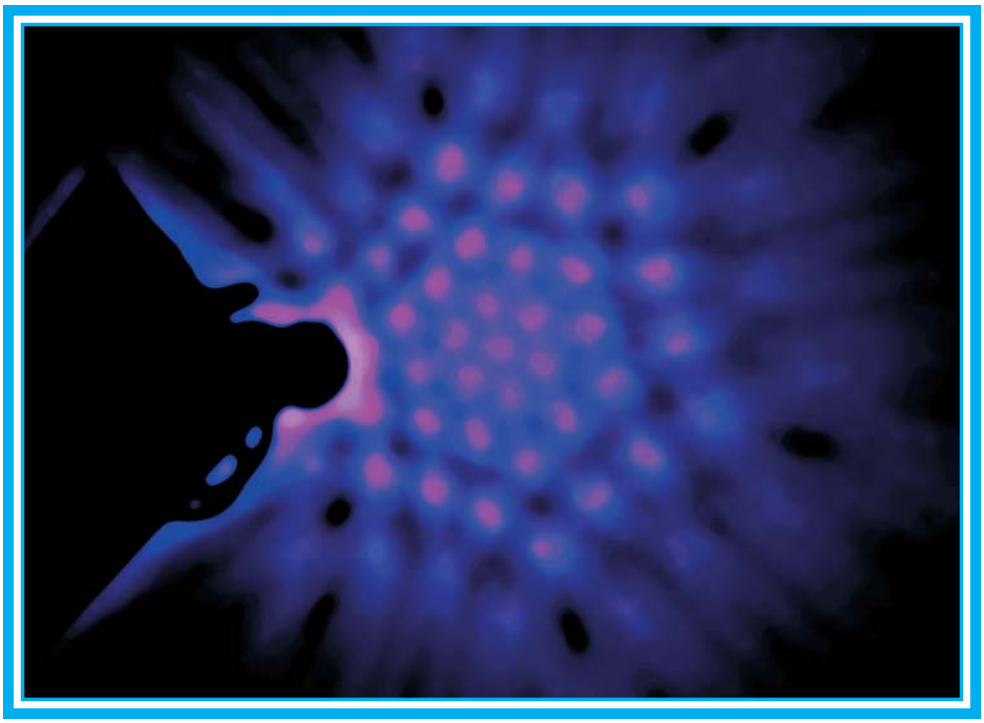

*Research Briefs* for the Physical, Chemical, & Nano Sciences Center is published by Sandia National Laboratories, a multiprogram laboratory operated by Sandia Corporation, a Lockheed Martin Company, for the United States National Nuclear Security Administration and the Department of Energy under Contract DE-AC04-94AL85000.

Additional complimentary copies are available by contacting:

**Julia M. Phillips**
**Physical, Chemical, & Biomolecular Sciences Center, 1100**
**Sandia National Laboratories**
**Albuquerque, NM 87185-1427**

**Phone: (505) 844-1071**
**Fax: (505) 844-6098**
**E-mail: jmphill@sandia.gov**
**url: http://www.sandia.gov/1100/index.htm**

*Research Briefs*

**Editors**
J. M. Phillips
J. A. Nichelason

**Production**
M. Sheila Wilson

**Cover Page:** "Far field emission patterns from a photonic crystal light emitting diode (LED), which has a strongly modified emission pattern due to scattering of waveguides modes out of the LED chip." See pages 38 and 39 for further details.

# Message from the Director

The Physical, Chemical, & Nano Sciences Center provides new scientific knowledge in support of Sandia's mission areas–nuclear weapons, energy and infrastructure assurance, nonproliferation and assessments, military technology and applications, and homeland security. We provide science-based solutions for the mission needs of our parent agency, the National Nuclear Security Administration (NNSA), particularly in areas where we have unique expertise. Of equal importance, we also perform focused long-term research in areas that are most likely to have impact on future Sandia missions and national security, particularly in the physical, chemical, and nano sciences that will enable future microsystems. This volume highlights representative research in our areas of emphasis, including Nanoscale Phenomena, Nanomechanics & Nanomanipulation, Wide Band-gap Semiconductor Materials & Devices, Electromagnetic Radiation Generation, Detection, & Spectroscopy, and Materials in Extreme Environments.

The activities of the Physical, Chemical, & Nano Sciences Center are supported by a diverse set of funding sources that reflect the broad impact of our work, both scientifically and programmatically. The research described in this volume illustrates the importance of a strong science base in the physical, chemical, & biomolecular sciences for the success of the Department of Energy's missions. Throughout this work, we have benefited immeasurably from our partnerships with colleagues across the labs, in universities, and in industry. We gratefully acknowledge their collaboration.

We appreciate your interest in our work and welcome your comments and inquiries.

**Julia M. Phillips**
*Director*

# Table of Contents

## Nanoscale Phenomena



## Nanomechanics & Nanomanipulation



## Wide Bandgap Semiconductor Materials & Devices

# Table of Contents Cont'd



## Electromagnetic Radiation: Generation, Detection, & Spectroscopy



## Materials in Extreme Enviornments: Radiation, Plasma, & Shock

# Table of Contents Cont'd

# Nanoscale Phenomena

# *Exploiting Interfacial Water Properties for Desalination and Purification Applications*

*by* **P. J. Feibelman (with R. T. Cygan, B. C. Bunker, C. J. Brinker, and T. M. Nenoff)**

**Motivation**—Dearth of potable water plagues half the world's population, causing death, disease, and international political tension. Improved understanding of water behavior in porous purification systems will have a profound impact on water supply, decontamination, and desalination technologies. Significant improvements over conventional water treatment processes will, however, require novel approaches, based on fundamental understanding of nanoscale and atomic interactions at interfaces between aqueous solution and materials. A group of about 20 Sandia scientists has accordingly formed to study how the structure and composition of materials surfaces affect the molecular arrangement, transport and chemistry of adjacent, impure water, and how confinement in pores modifies these properties.

**Accomplishment**—We held a workshop in April 2005, aimed at identifying key unresolved scientific issues and fostering collaborations. A summary of discussions and key conclusions, by R. T Cygan and J. A. Greathouse, is available at www.sandia.gov/water/waterworkshop.

Research now begun is divided into 2- and 3-dimensional components. The 2D work (Fig. 1) takes advantage of the ability to "see" what is happening at a water interface with a flat, high quality surface, and to use the high degree of control in a "surface science" environment to isolate the surface properties that control interfacial water structure and transport. By applying a wide range of analytical techniques, now being tested, we have a reasonable chance of discovering the nature of what we know to be a very complicated interfacial environment.

Our 3D work focuses on understanding how interplay of pore structure and composition controls pore function. (Fig. 2) One thread is to use SNL expertise in synthesis to fabricate model pores of desired size, shape and surface-functionality, allowing quasi-realistic tests of concepts for improved purification. Another involves synthesizing "molecular sieves," and systematically relating composition and structure to ion-exchange capabilities.

The broad range of expertise at Sandia is critical to eventual success. Currently, we are building and validating 2-d approaches based on NMR, non-linear optics (sum-frequency generation), interfacial-force, atomic-force and scanning-tunneling microscopies. 3-d efforts involve self-assembly, focused particle beam lithographies, and atomic layer deposition to create the membrane platform allowing structural and functional characterization of individual nanopores. Neutron spectroscopy is our key probe of water behavior in zeolite membranes. Analyzing our results via ab-initio and classical simulations is a common theme of our group project. Theorists, working closely with our experimenters, will support data interpretation, suggest experimental directions and develop new concepts.

**Significance**—Learning to increase water flux through porous membranes by even one order of magnitude would have worldwide impact on desalination and purification technologies. By establishing a scientific basis for identifying and overcoming the critical roadblocks to improved purity and flow, we will guide R&D efforts to optimal impact.

**Sponsors for various phases of this work include:** Laboratory Directed Research & Development

**Contact:** Peter J. Feibelman, Surface and Interface Sciences, Dept. 1114
Phone: (505) 844-6706, Fax: (505) 844-1197, E-mail: pjfeibe@sandia.gov

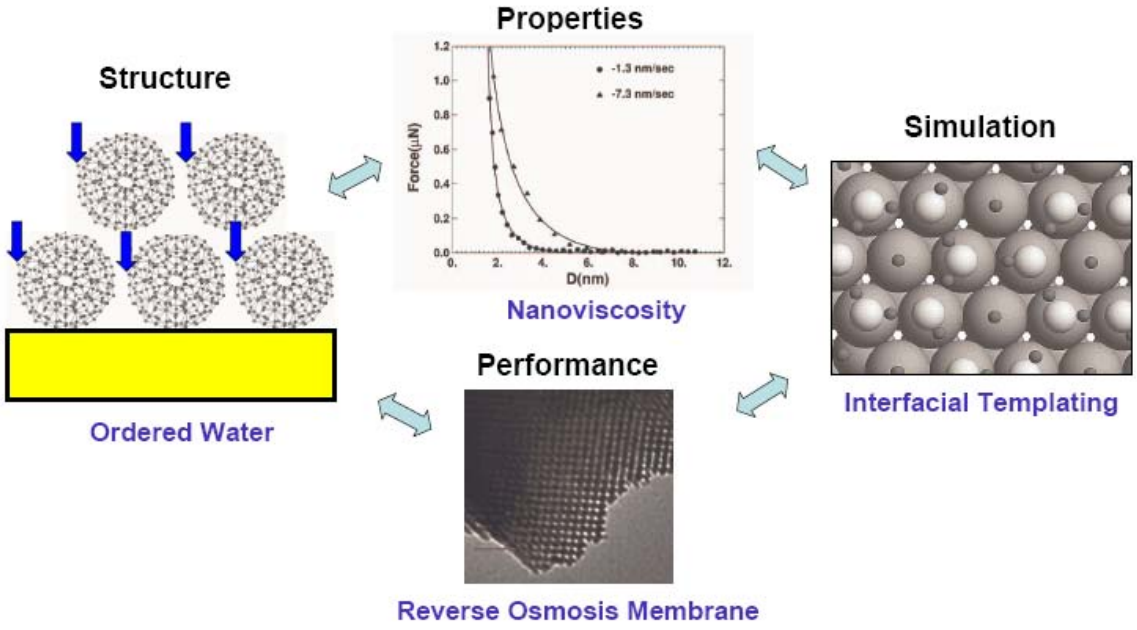


**Figure 1**. To learn how surface structure and properties affect water treatment technologies, 2D studies of "interfacial water" and its behavior will be conducted on model surfaces whose structure and chemistry can be systematically varied.

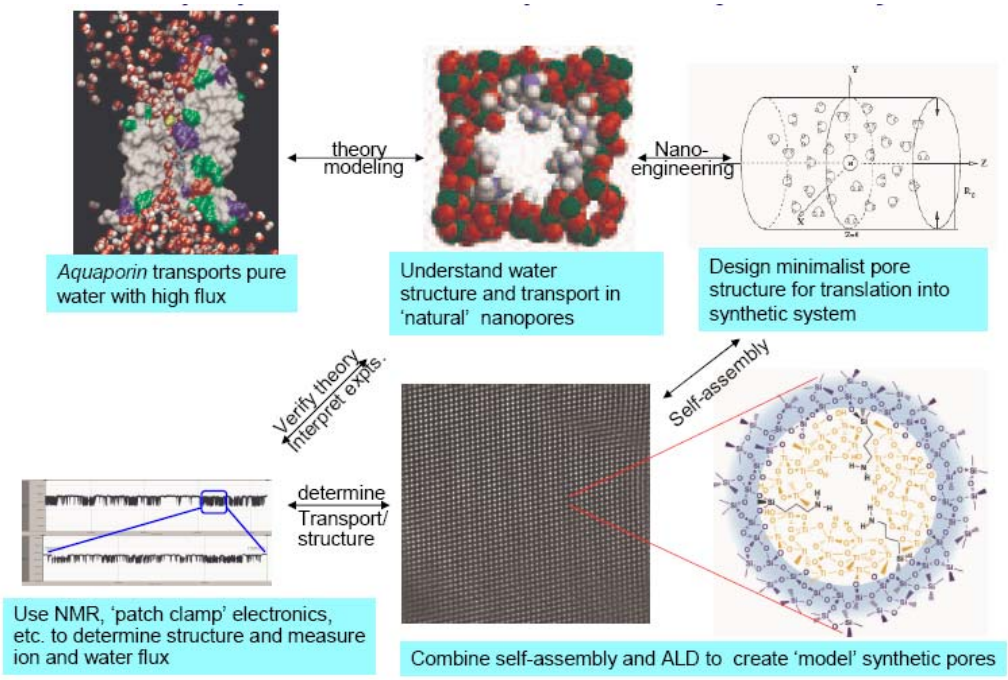


**Figure 2**. 3D studies will combine theory, modeling, synthesis and characterization to teach us how to embody properties of natural pores in synthetic systems.

# *Investigations of the Role of Cl on Pit Initiation in Aluminum Using STEM-EDS Spectral Imaging*

*by* **N. A. Missert, D. Elswick, P. G. Kotula, J. J. Hren, C. M. Johnson and R. G. Copeland**

**Motivation—**Although it is well known that the presence of chloride in an electrolyte can initiate pitting in passive metals, the precise mechanisms responsible for pit initiation are still under debate. The local Cl concentration, the critical location either at the surface, within the oxide or at the metal-oxide interface, and the nature of the bonding between Cl and the passive film are all thought to be important for pit initiation. In order to distinguish between these factors, ion implantation has been used to control the concentration, location and source of Cl in the aluminum thin film system, and Scanning Transmission Electron Microscopy-Energy Dispersive Spectroscopy (STEM-EDS) spectral imaging has allowed the discovery of the resulting Cl-rich nanostructures that influence corrosion pitting.

**Accomplishment—**Samples were implanted at ambient temperature using 35 keV $Cl^+$ ions with fluences ranging from 1 – 7 x$10^{16}$ions/cm$^2$. When the films are polarized in a halogen-free electrolyte, an increase in pitting probability is observed with increasing implanted Cl concentration. STEM-EDS was performed on cross-sections prepared with a focused ion beam and on conventional plan-view specimens. The Cl distributions were measured using a spectral imaging analysis technique developed at Sandia. At each 2 nm pixel, the x-ray spectrum excited by the electron beam is collected and a multivariate statistical analysis is performed to correlate pixels with the same spectrum. Each pixel can be coded according to its spectrum in order to create a map that shows the spatial distribution for each spectrum. Figure 1 shows the bright field image (plan view) and the Cl distribution observed for the samples implanted with a fluence of 1 x $10^{16}$/cm$^2$ (a), and 5 x $10^{16}$/cm$^2$ (b), where the intensity of the Cl-containing spectrum increases as the color scale goes from blue to red. These results show that when the Cl fluence is high enough such that the pitting probability increases substantially, the Cl distribution changes from relatively uniform and homogeneous (Fig. 1a) to heterogeneous nanostructures (Fig. 1b). The larger ~ 10 nm Cl-rich nanostructures have a preference for forming along the grain boundaries in the films where the pitting probability is high. Diffraction patterns obtained from the films implanted with a Cl fluence of 5 x $10^{16}$/cm$^2$ show lattice spacings consistent with $AlCl_3$ in addition to the Al lattice. If these nanostructures occur close enough to the passive oxide layer, they could be responsible for stabilizing pitting corrosion.

**Significance**—Pitting corrosion in passive metals occurs in the presence of aggressive halogens such as $Cl^-$. This work shows that in order to stabilize pitting in a halogen-free electrolyte, a critical Cl concentration, accompanied by the formation of high Cl–content nanostructures is required. Further work is underway to determine whether the observed distribution is stable as the films are polarized towards pitting. The ability to measure local changes in Cl concentration with the high spatial resolution attainable using this technique is expected to lead to further understanding of the role of Cl in pit initiation.

**Sponsors for various phases of this work include:** DOE Office of Basic Energy Sciences

**Contact:** Nancy A. Missert, Nanostructure & Semiconductor Physics, Dept. 1112
Phone: (505) 844-2234, Fax: (505) 844-1197, E-mail: namisse@sandia.gov

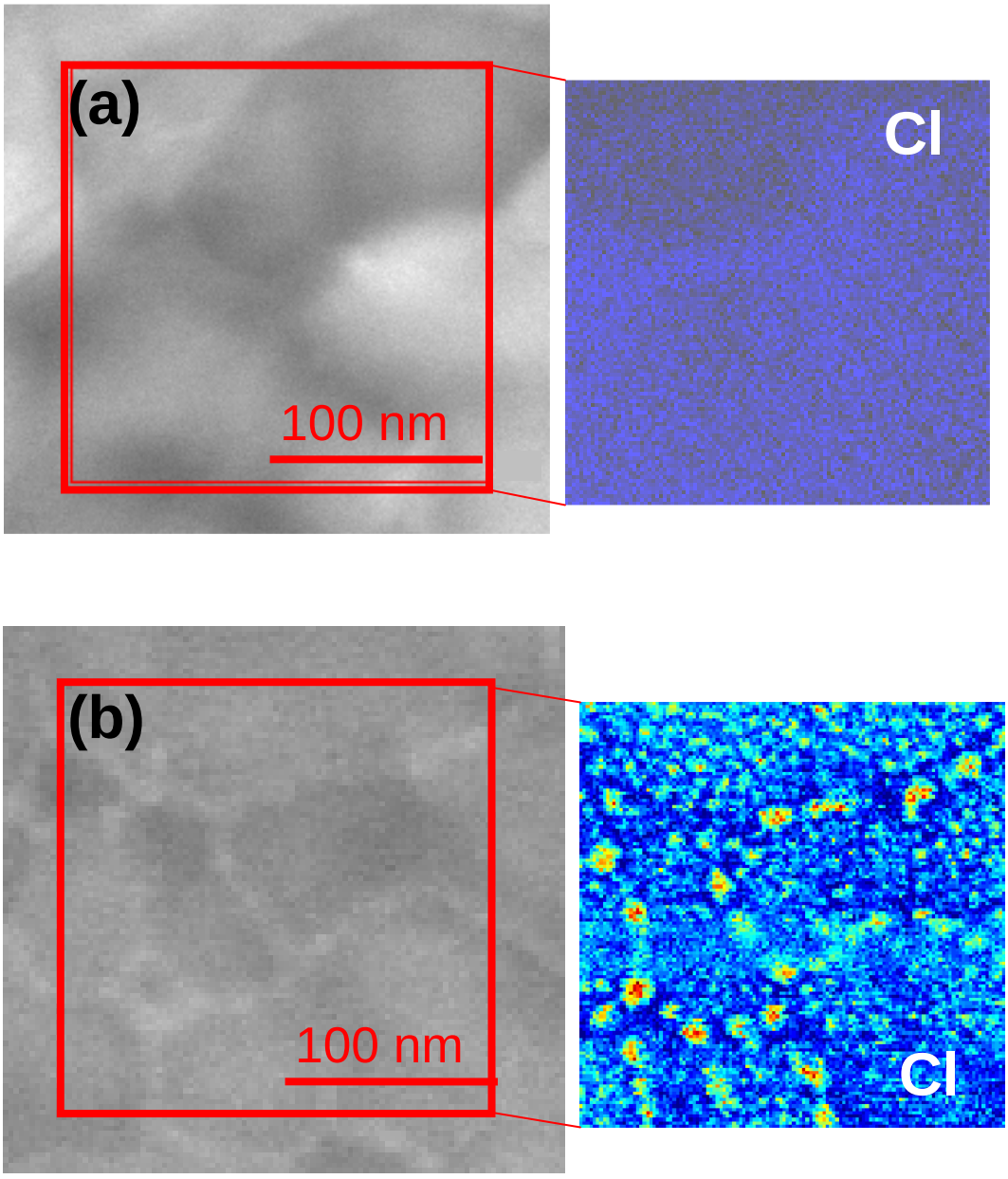


**Figure 1.** (a) Bright field TEM image of Al thin film implanted with a Cl fluence of 1 x $10^{16}$/cm$^2$, the spectral image for the homogeneous Cl-rich component is shown to the right (b) Bright field TEM image of Al thin film implanted with a Cl fluence of 5 x $10^{16}$/cm$^2$, the spectral image for the Cl-rich component on the right shows evidence of nano-cluster formation, with the largest clusters along the grain boundaries.

# *Precise Positioning of Quantum Dot Molecules by Directed Self-Assembly*

*by* **J. A. Floro**

**Motivation**—In order to overcome the fundamental limits that will prevent continued shrinking of microelectronics, revolutionary new quantum computing schemes will be needed within the next two decades. However, if we are to realize the extraordinary information processing potential offered by quantum logic, control at near-atomic length scales is required to build devices based on ordered assemblies of nanoscale quantum dots. While such structures are well beyond the capabilities of standard lithographic techniques, *directed self-assembly* approaches are already demonstrating how complex 3D nanostructures can be constructed via manipulation of the natural processes associated with their growth. We self-assemble quantum dot nanostructures by exploiting intrinsic strain relaxation processes during heteroepitaxial growth of thin SiGe alloy films on Si substrates. This growth/materials strategy is well aligned with current device fabrication procedures, making its acceptance by the microelectronics industry far more likely than other techniques for quantum dot production.

**Accomplishment**—While existing research has emphasized formation of individual quantum dots, we have extended our investigations to self-assembly of quantum dot *molecules*, (QDMs) — size-selecting nanostructures consisting of four quantum dots elastically bound together by a central "anti-dot". QDMs normally self-assemble at random locations, as shown in Fig. 1, which is incompatible with nanologic device requirements. This year we have shown that QDMs can be precisely located using patterns established *ex situ* by focused ion beam (FIB) treatments of a Si substrate. The FIB was used to create periodic arrays of nanoscale holes in the Si, with varying depths and spacings, as shown in Fig. 2. These patterned substrates were then subjected to our standard, kinetically controlled, growth regimen for SiGe on Si that produces QDMs on unpatterned substrates. By controlling the Si buffer layer thickness and the FIB dose, we can precisely locate QDMs in one-to-one correspondence with the FIB hole array, as shown in Fig. 3 for several pattern spacings. Note that a one-to-one correspondence of QDMs to FIB features actually represents a four-to-one correspondence of quantum dots to FIB features, which is efficient. Very small FIB doses can be used to locate QDMs, but "missing pixel" errors start to crop up at low dose. While we observe spurious nucleation of QDMs on the patterned substrates, this is minimized by reducing ion dose and increasing pattern density.

**Significance**—The ability to put QDMs where we want them is critically important to their application in quantum computing. An example is the use of QDMs in a logic architecture based on *quantum cellular automata (QCA)*, which requires the use of four-fold QDMs (acting as charge-switching logic elements) arranged in specific patterns. QCA logic relies on electrostatic interactions and therefore does not require interconnects between the individual QDMs, as long as proper positioning, size-selection and spacing can be achieved. Our directed self-assembly process results in pre-specified patterns of elastically bound, four-fold quantum dot structures that exhibit narrow size distributions. Hence we are already achieving many of the critical requirements for self-assembly of semiconductor QCA.

**Sponsors for various phases of this work include:** DOE Office of Basic Energy Sciences and National Science Foundation

**Contact:** Jerrold A. Floro, Surface & Interface Sciences, Dept. 1114
Phone: (505) 844-4708, Fax: (505) 844-1942, E-mail: jafloro@sandia.gov

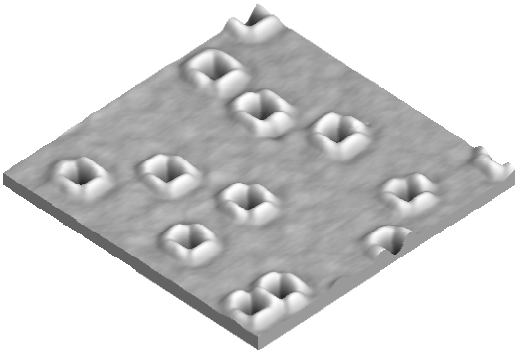

**Figure 1.** Heteroepitaxial QDMs in $Si_{0.7}Ge_{0.3}$ on unpatterned Si. Atomic force microscope image, 2x2 μm.

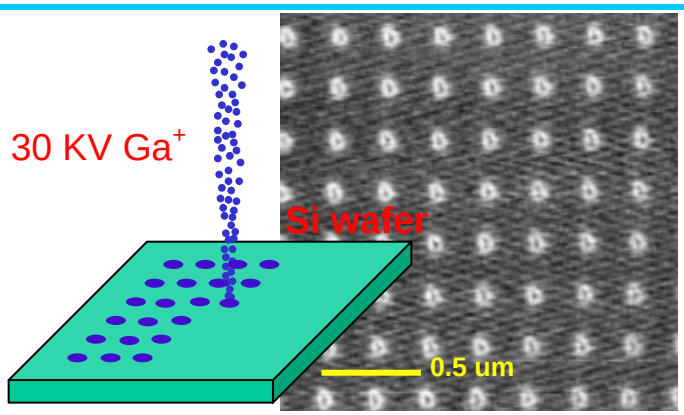


**Figure 2.** A focused ion beam is used to write an array of shallow, nanoscale holes in a Si wafer, as shown schematically. An atomic force microscope image of an actual hole array is also shown.

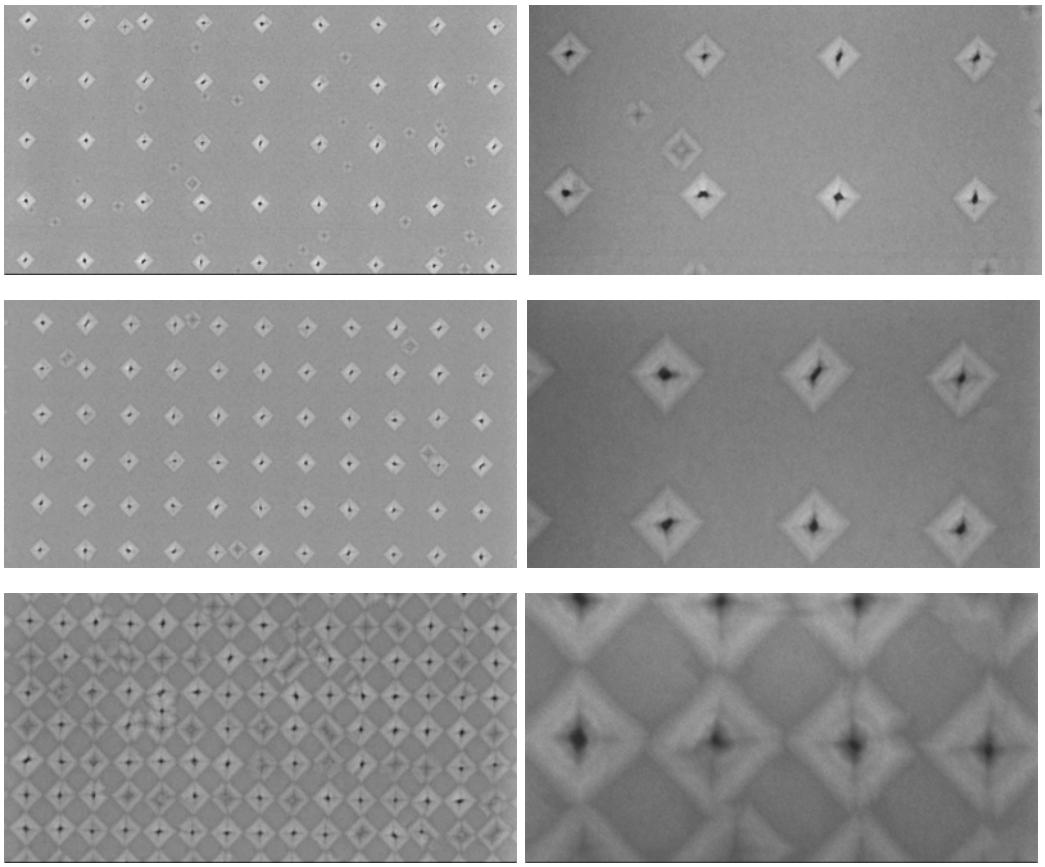

Figure 3. $Si_{0.7}Ge_{0.3}$ QDM arrays on FIB-patterned Si, at low (images on left) and high (images on right) magnification. Upper panel: 0.75 μm feature spacing; middle panel: 0.5 μm feature spacing; lower panel: 0.25 μm feature spacing. Scanning electron microscope images.

# *DFT+U Studies of MnP Adsorption on Au(111) Surface and Electric Field Effects*

*by* **K. Leung, S. Rempe, P. Schultz, M. Chandross, and C. Medforth**

**Motivation—**Transition metal porphyrin molecules exhibit a wide range of electronic and magnetic properties. They have the potential to be deposited on metal electrodes and used as memory and molecular electronics elements, sensors, and other nanoscale devices. Recently, Shelnutt, Medforth, and coworkers proposed a novel nanomechanical application of "bridled" Ni(II) porphyrins based on a ligand-binding induced increase of the $Ni^{2+}$ effective radius (Fig. 1).[1] This molecule can potentially exhibit nano-tweezer motion that can be used to grab on to/release toxin or drug molecules, and thus have national security implications. In this theoretical work, we consider Mn(II) porphine (MnP) deposited on Au(111) as a simple mimic of nickel porphyrin which may exhibit similar effective metal ion size changes when subject to an electric field.

**Accomplishment—**Accurate modeling of this composite Mn(II)P/Au(111) system is extremely challenging. Density Functional Theory (DFT) with the Perdew-Burke-Brazerhof (PBE) exchange correlation functional, routinely used in surface science calculations, is accurate for the Au(111) surface but does not predict the correct spin state for isolated MnP. Quantum chemistry methods work much better for the latter but are not feasible (~100 times more costly than PBE) to apply to a periodically replicated model of a gold electrode.

Here we apply for the first time the DFT+U method to a 1st row transition metal center in a molecule.[2] DFT+U has been successfully used to treat strongly correlated electron systems such as nickel (II) oxide and $LaCoO_3$ (related to the colossal magentoresistence materials). We parameterize the "U" in DFT+U (the intra-d band coulomb term) with spin-spittings predicted using quantum chemistry method.

Table 1 illustrates the success of this approach for the isolated MnP molecule. PBE predicts incorrect spin states and molecular geometries. Tuning U=4.2, DFT+U yields both the correct high-spin ground state and a Mn(II)-N bond length similar to experimental values.

Figure 2 depicts MnP deposited on Au(111) and the resulting change in its electron density distribution. The binding energy is 0.7, and the spin polarization changes from s=5/2 to s=2, consistent with a change of the Mn(III) oxidation state and the interpretation that Mn has donated an electron to the gold substrate. This apparent electron transfer can be reversed by applying a 0.7 eV/A electric field, which recovers the high spin state associated with Mn(II). The field-induced 0.13 A increase in Mn-N distance is reminiscent of that in bridled nickel porphyrins, and suggest that manganese porphyrins (or expanded porphyrins) may be tailor-made into electric-field triggered, switchable molecular devices.

**Significance**—Our theoretical predictions provide impetus to future atomic force microscope experiments aimed at demonstrating and exploiting switchable molecular devices assembled on gold electrodes. Our novel application of the DFT+U method will enable *ab initio* molecular dynamics studies of reactions involving 1st row transition metals in aqueous and biological environments, and open up new areas of theoretical research.

[1]Song, *et al.*, J. Am. Chem. Soc. 127:1179 (2005)
[2]Liechtenstein *et al.*, Phys. Rev. B 60:8257 (1994).

**Sponsors for various phases of this work include:** Laboratory Directed Research & Development

**Contact:** Kevin Leung, Surface & Interface Sciences, Dept. 1114
Phone: 844-1588, Fax: 844-5470, E-mail: kleung@sandia.gov

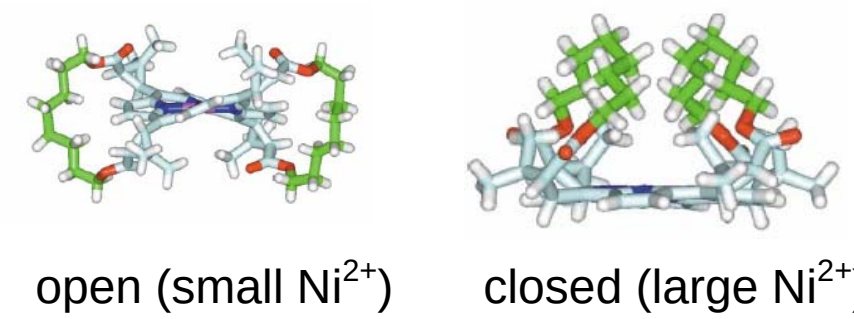


**Figure 1.** Open and closed conformation of a bridled Ni(II) porphyrin [1].

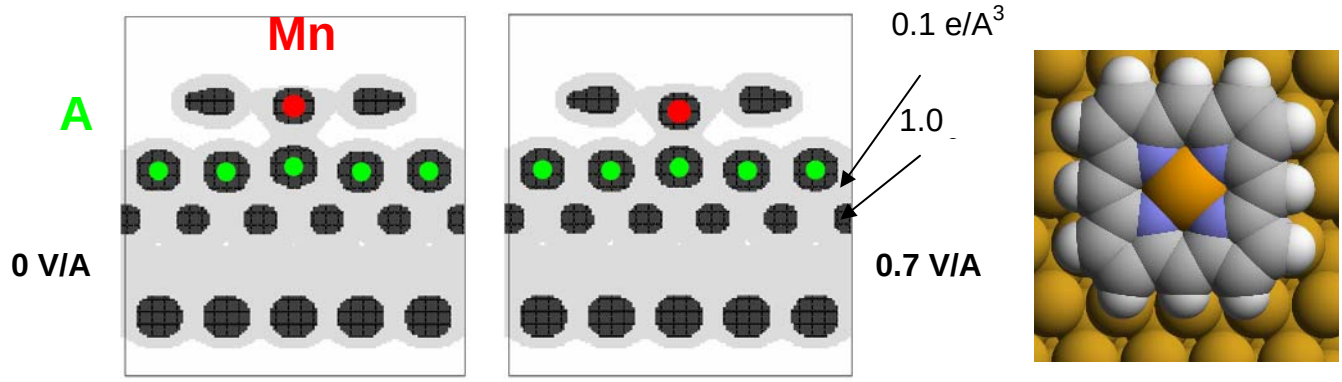


**Figure 2.** MnP deposited on Au(111): electron charge densities in absence/presence of electric field.

| | Mn(II)P | Mn(II)P* | MnP/Au(111) | MnP/Au(111)+field | MnP/Au +field* |
|---|---|---|---|---|---|
| d(Mn-N) | 2.09 A | 2.05 A | 2.02 A | 2.15 A | 2.02 A |
| $E_{bind}$ | NA | NA | 0.7 eV | 0.1 eV | 0.2 eV |
| total spin | 5/2 | 3/2 | 2 | 5/2 | 3/2 |

**Table 1:** The Mn-N distance in the porphine ring, the binding energy on Au(111), and total spin polarization of manganese (II) porphines. Computed using the DFT+U method except where marked by an asterisk (those use the PBE functional, which is inadequate for isolated manganese porphines).

# *Programming Dynamic Self-Assembly: Theory and Simulations*

*by* **A. M. Bouchard, C. E. Warrender, and G. C. Osbourn**

**Motivation—**Our goals are to: (1) Understand how living systems dynamically self-assemble, reconfigure, and disassemble materials. (2) Harness energy-consuming proteins, such as microtubules and directional motor proteins, outside of cells, as molecular self-assembly "construction crews." (3) Program these processes in non-cellular environments, to build hierarchical, dynamic materials.

**Accomplishment—**We have developed a set of stochastic simulations of microtubules (MTs) and kinesin motor proteins that illustrate several types of programmable dynamic self-assembly. The dynamic and statistical properties of the MT dynamic instability and kinesin transport along the MTs were matched to experimental behaviors.

The first simulation was designed to mimic the dynamic optical properties of melanophores (color-changing skin cells of fish and amphibians). We were seeking a minimal set of protein types that would enable repeatable, nano-scale pigment particle condensation (for transparent volumes) and dispersal (for opaque volumes). We succeeded using only MT-organizing centers, MTs, and pigment granules coated with two types of motor proteins: an inward-walking motor and a genetically engineered outward-walking motor that can be reversibly "locked" to prevent transport. Our engineered system requires far fewer protein types to achieve this optical control than the actual melanophore cells use. Simulation results, showing the system in the condensed and dispersed states, are shown in Fig. 1.

The second simulation was designed to illustrate sorting and patterning of mixtures of two nano-scale particle types. This was achieved by coating one particle type with only outward-walking motors and the other with only inward-walking motors before introducing them into the mixture. By controlling the placement of multiple MT-organizing centers, the simulation showed that we can create volumes that exclude one particle type and condense the second. In addition, if there is a boundary on the space that blocks MT growth, then that boundary is decorated with the single excluded particle type. See Fig. 2.

The third simulation (Fig. 3) was designed to illustrate selective harvesting of nano-particles from a mixture, then delivering the harvested particles at a controlled time to a destination labeled by MT stabilizers. This required genetically engineered switches for both inward- and outward-walking motors, selective coating of the particles to be harvested with both motors, and placement of MT-organizing centers in the mixture region.

**Significance**—These simulations demonstrate multiple ways in which disordered and mixed nano-particles can be ordered using energy-expending protein networks. An interesting aspect of these results is that we harness stochastic mechanisms to produce order in a reliable way, in imitation of biological self-assembly processes. Our stochastic simulation capability provides a testbed for predicting the structures and yields of dynamic self-assembly processes that can be realized experimentally. The results presented here represent key components of a much broader set of programmable self-assembly processes that we will explore in the future.

**Sponsors for various phases of this work include:** DOE Office of Basic Energy Sciences

**Contact:** Ann M. Bouchard; Lasers, Optics, & Remote Sensing; Dept. 1128
Phone: (505) 845-0552, Fax: (505) 844-5459, E-mail: bouchar@sandia.gov

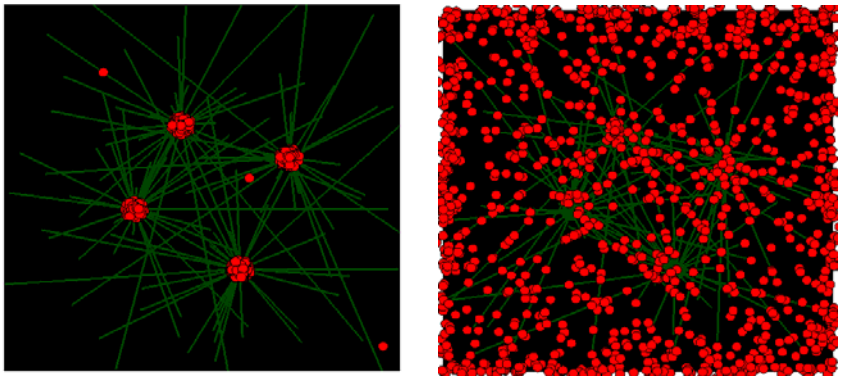

**Figure 1.** Results from melanophore simulation, showing condensed (left) and dispersed (right) states. Pigment granules are red, MTs are green.

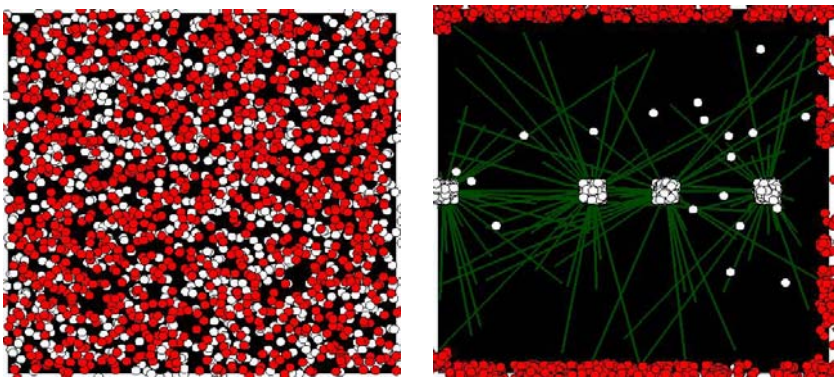

**Figure 2.** Initial disordered state (left). White (red) particles have inward-walking (outward-walking) motors. After ~10 minutes simulation time, red particles are excluded from the volume and decorate the boundary, while white particles are collected at the MT-organizing centers along the mid-line.

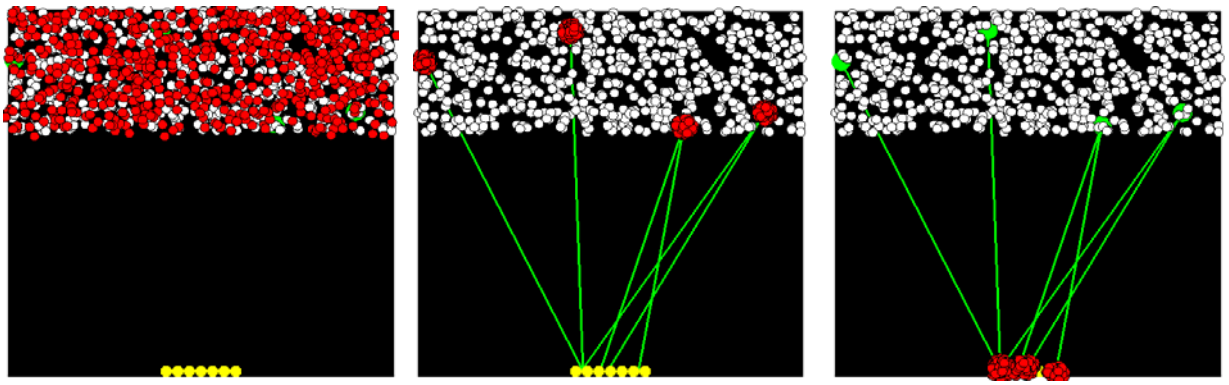

**Figure 3.** Initial state (left) with mixed particles (red and white) and MT-organizing centers (green) in upper portion of space, MT stabilizers (yellow) along the bottom. Red particles have lockable inward-and outward-walking motors; initially outward motors are locked. White particles have no motors. After ~7 minutes simulation time (center), red particles are harvested to the MT-organizing centers and MTs (green) grow a bridge to the stabilizers. Then, the harvested particles' outward motors are unlocked and inward motors are locked, so that the red particles are transported to their destination, at the MT stabilizers at the bottom (right).

# *RF-to-Millimeter Wave AC Conductivity of Carbon Nanotubes*

*by* **C. Highstrete, M. Lee, and A. Talin**

**Motivation**—Carbon nanotubes (CNTs) are predicted to have novel electrodynamic properties that could be exploited to push nanotechnology into the rf-thru-millimeter wave frequency domain. For example, pure CNTs are thought to support ballistic charge transport that can be used to construct power-efficient, frequency-agile oscillators and detectors. Chemically functionalized with molecule-specific receptors, CNTs can serve in an entirely new capacity: *chemically* tunable AC components for ultra-sensitive chem/bio sensors. Development of CNTs for high frequency will require far more advanced empirical knowledge of basic electrodynamic properties than exists. This is particularly true in view of the suspected ballistic nature of charge transport, which if true means that the conventional Drude model of high frequency conductivity will not apply. The goal of our research is to perform experiments that will elucidate clearly and quantitatively the electrodynamic properties of CNTs.

**Accomplishment**—We designed and fabricated a broadband, flexible experimental platform to measure the real and imaginary conductivity of CNTs from 0.01 to 50 GHz in frequency and from 300 K down to 4 K in temperature. The experimental platform is based on a co-planar waveguide (CPW) onto which CNTs are directly assembled across the dielectric gaps, see Fig. 1. The difficult constraint was that the CPW dimensions had to be large enough so that the waveguide impedance remained approximately 50 Ω to match the high-frequency measurement instrumentation impedance, and small enough to support CNT directed assembly by AC dielectrophoresis. The AC dielectrophoresis method offers reasonably well-controlled numbers of CNTs to be assembled on the CPWs so that the CNT axis is polarized along the electric field of the propagating electromagnetic radiation in the waveguide mode.

We measured the CPW's complex reflection and transmission coefficients before and after CNT assembly using a vector network analyzer on a broadband probe station. Initial results are shown in Fig. 2. Clearly observable are changes in reflection and decreased transmission (i.e. increased dissipation) due to the CNTs. Interestingly, characterization of these first samples indicate that only a very small number of individual CNTs assembled at a few random positions along the 5 mm waveguide. The reflection oscillations shown in Fig. 2 are believed to arise from the interference of reflections by a few CNTs along the waveguide. While we cannot yet determine the exact number and positions of the CNT assembly, these data show that our measurement methods are sensitive to only a small number of CNTs.

**Significance**—The data shown in Fig. 2 represent the first broadband measurement of the intrinsic rf-to-millimeter wave AC conductivity properties of CNTs. Once we have refined the experimental procedure so that the assembled CNTs can be counted and localized, such data will deliver clear and quantitative information about the important physical electrodynamic properties of these widely used nanomaterials. This knowledge and the techniques we develop will open the door to exploiting CNT nanotechnology in high-frequency devices.

**Sponsors for various phases of this work include:** DOE Office of Basic Energy Sciences

**Contact:** Mark Lee, Semiconductor Material & Device Sciences, Dept. 1123
Phone: (505) 844-5462, Fax: (505) 844-4045, E-mail: mlee1@sandia.gov

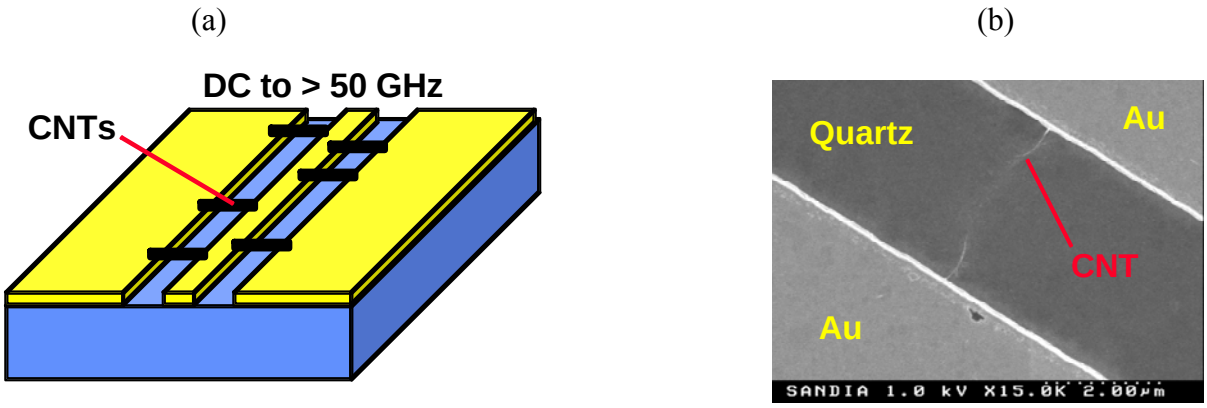


**Figure 1.** (a) Sketch of a broadband co-planar waveguide geometry. The yellow indicates gold electrodes, and the blue represents the dielectric substrate. A few carbon nanotubes (CNTs) are depicted assembled across the gaps. (b) Plan view scanning electron micrograph of a single CNT assembled across a 3 µm wide quartz gap in a co-planar waveguide. The CNT is continuous but sags slightly out of the focus plane in the center of the gap.

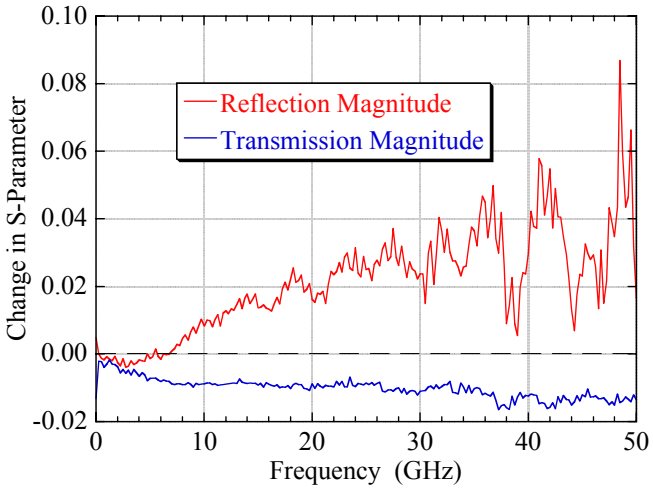


**Figure 2.** Change in reflection and transmission magnitudes as a function of frequency for the same co-planar waveguide before and after CNT assembly by AC dielectrophoresis. This waveguide was assembled in the same manner as the one depicted in Fig. 1(b). A reference waveguide on which no CNTs were assembled showed no measurable change in repeated measurements.

# *Tunneling Spectroscopy in Vertically Coupled Quantum Wires*

*by* **M. P. Lilly, E. Bielejec, J. L. Reno, and S. K. Lyo**

**Motivation**—Tunneling measurements provide a tool to directly measure the density of states and the impact of Coulomb interactions both within and between low dimensional systems. Interpretation for two-dimensional (2D) systems is well defined in the Fermi liquid framework. Our group has focused on extending tunneling measurements to one-dimensional (1D) quantum wires. In 1D systems there remains an open question about the use of non-interacting theory to describe the tunneling and modifications due to interactions.

**Accomplishment**—We have measured tunneling spectroscopy in both 2D and 1D systems and compared the results to a non-interacting theory for tunneling. In 2D, differential conductance results are shown in Fig. 1a. The energy and momentum dependence of the tunneling events are captured using a voltage between the layers and an in-plane magnetic field. Qualitatively, the "fish" shape is well described by a theory for non-interacting electrons shown in Fig. 1b; interaction effects are subtle. The main features are due to overlap of the Fermi surface with the dispersion curves in the other layer. To measure 1D tunneling, we fabricated a vertical double quantum wire (Fig. 2a)[1]. The 1D density is directly controlled in each wire using the split gates. Independent contact to each wire is achieved using the depletion gates. In Figs. 2b and 2c tunneling spectra are shown for 1D densities chosen such that a single subband (2b) or two subbands (2c) are occupied in each wire. The effect of increasing the number of subbands is to nest the "fish" structure, and this nesting is clearly observed at high magnetic fields where a single crossing is observed for one subband (2b, B=3.5 T), and two crossings are observed for two subbands (2c, B=3.5T and 4.0T). While some qualitative comparison to tunneling theory for non-interacting electrons is successful, we note a number of deviations, as well. Most significantly, the structure at low fields for a single 1D subband (Fig. 2b) is more complicated than that observed for 2D tunneling (Fig. 1a). We also observe broad resonant features at all 1D densities when a much more narrow and well defined resonance is expected. To further our understanding of the deviations, we are considering finite size effects and the role of many-body Coulomb interactions in the double quantum wire system.

**Significance**—1D tunneling in a split-gate-defined double quantum wire is measured for the first time. The split gate provides explicit control over the density and number of occupied subbands in each wire. The experimental tunneling spectroscopy for the 2D system is in good agreement with theory, and provides a demonstration of the technique. A number of features in the 1D spectroscopy can be clearly explained using a non-interacting picture for the electrons, but other features (broad resonance, structure in 1,1) cannot be so easily understood. Interactions within and between the wires is one possible explanation. The techniques used to create this interacting nanoelectronic structure can easily be used to fabricate a wide range of nanoelectronic systems for further studies of interactions at the nanoscale, coherent transport, single charge and spin measurement and quantum computing.

[1]E. Bielejec, J. A. Seamons, J. L. Reno, and M. P. Lilly, Appl. Phys. Lett. **86**, 83101 (2005).

**Sponsors for various phases of this work include:** DOE Office of Basic Energy Sciences and Laboratory Directed Research & Development

**Contact:** Michael P. Lilly, Semiconductor Material & Device Sciences, Dept. 1123
Phone: (505) 844-4395, Fax: (505) 844-1197,E-mail: mplilly@sandia.gov

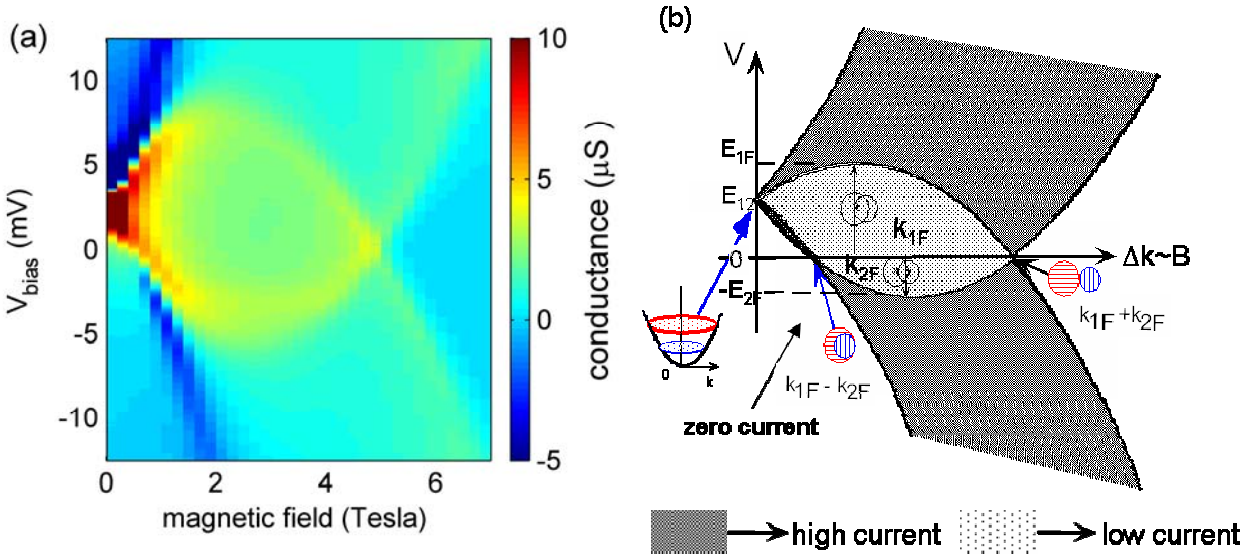


**Figure 1.** (a). Tunneling conductance (dI/dV) between 2D layers at T=0.3 K separated by a 10 nm barrier. The 2D densities are $n_1=1.96\times10^{11}$ cm$^{-2}$ and $n_2=1.16\times10^{11}$ cm$^{-2}$. (b). Theory for tunneling in a non-interacting system. Diagrams indicate relative positions of the dispersion curves. Energy difference is the y-axis in each plot, and the wave vector difference (proportional to the in-plane magnetic field) is the x-axis. The features present in the experiment are well described by the theory.

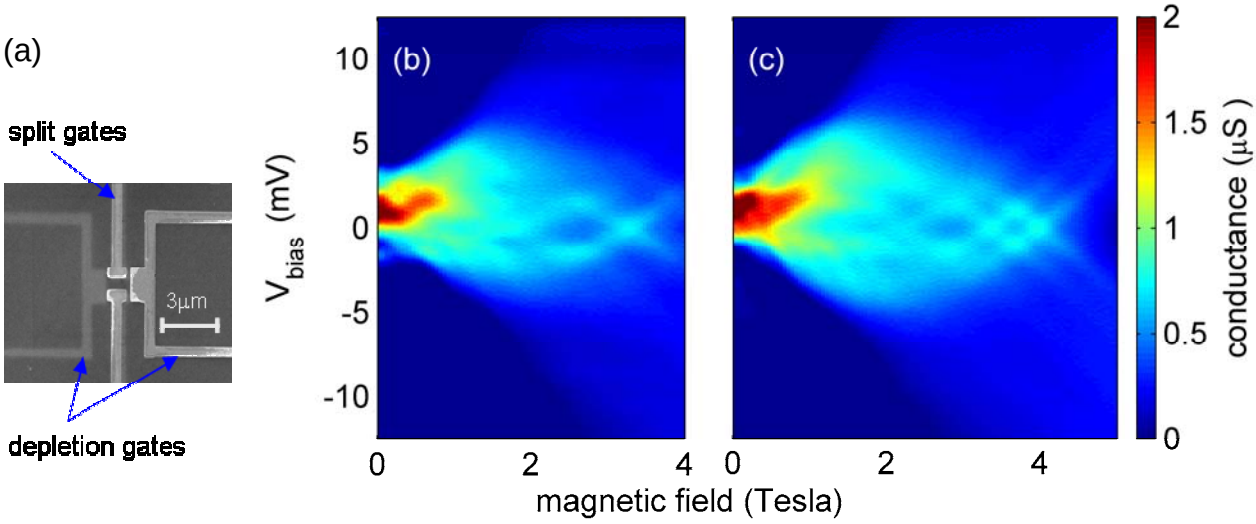


**Figure 2.** (a) SEM of a double quantum wire device. (b,c) Tunneling conductance for two quantum wires at T=30mK separated by a 7.5 nm barrier. In (b), a single 1D subband is occupied in each wire. In (c), two subbands are occupied. The non-interacting theory in Fig. 1 can account for some features, such as the crossings at high fields [1 in (b), and 2 in (c)] but cannot account for the additional complication at low magnetic fields.

# *Drag and Drift of Excitons by a Two-Dimensional Electron Current*

*by* **S. K. Lyo**

**Motivation—**Excitons are a good storage source of light energy and play an increasingly important role in opto-electronic applications. Motion of excitons has been studied for a long time. While desirable, it is very difficult to control the motion of excitons, because excitons cannot be accelerated by an external electric field due to their charge neutrality. We propose a mechanism whereby an exciton gas can be dragged efficiently by an external field into a desired direction with a controllable and significant drift velocity.

**Accomplishment—**We have demonstrated theoretically that an exciton gas in a two-dimensional quantum-well layer can be dragged by an electric current in an adjacent well over a drift length estimated to be tens of microns during their lifetime of a few nanoseconds. Figure 1 shows this electron-exciton double quantum well structure with a thick center barrier to prevent tunneling. The drag velocity can be a significant fraction ($f$) of the drift velocity of the electrons, which can be very large for a high-mobility two-dimensional electron gas. For example, for an electron gas with mobility of ten million $cm^2$/Vsec, with velocity ratio $f$ = 0.1, and an applied field of 1 Volt/cm, the drift velocity of the exciton gas can be $10^6$ cm/sec, which is much faster than the sound velocity. Figure 2 displays the calculated ratio $f$ of the drift velocities of the exciton and electron gases as a function of the temperature for different electron densities and quantum well parameters. We have also shown that the exciton lifetime and therefore the drift length can be enhanced significantly due to the fact that moving excitons cannot emit photons.

The drag of the excitons is induced by the momentum transfer via monopole-dipole interaction from the electrons in the adjacent QW drifting under an external field. This inter-layer interaction is strong only when the masses of the electron and the hole of the exciton are asymmetric, namely very different as shown in Fig. 2. The inter-layer drag force is balanced by the resistive force applied to the excitons through electron-phonon scattering and interface-roughness scattering. These exciton scattering rates are small at low temperatures and for wide quantum wells, yielding small resistive force and thus large drag ratio $f$. This drag phenomenon is similar to the well-established Coulomb drag between two electron layers, where the electric current in one layer drags the electrons in the adjacent layer through Coulomb interaction inducing a voltage drop. Another mechanism known so far for dragging excitons is through surface acoustic waves, which drag excitons with the velocity of sound.

**Significance**—Tools for driving excitons in a given direction with a controllable speed over a long distance are useful in opto-electronic applications. The mechanism we have proposed relies on an external electric field to drag excitons with a speed faster than the sound velocity and enhances the exciton lifetime, yielding an increased exciton drift length. This work was published in Physical Review B **71**, 115317 (2005).

**Sponsors for various phases of this work include:** DOE Office of Basic Energy Sciences and Laboratory Directed Research & Development

**Contact:** S. Ken Lyo, Semiconductor Material & Device Sciences, Dept. 1123
Phone: (505) 844-3718, Fax: (505) 844-1197, E-mail: sklyo@sandia.gov

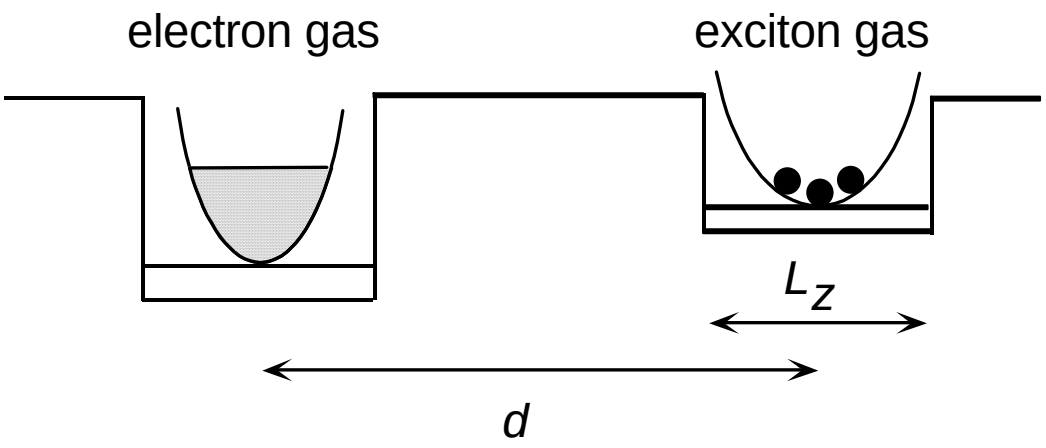


**Figure 1.** A schematic diagram of a double-quantum-well (QW) structure with an electron gas in the left QW and an exciton gas in the right QW. The two QWs are separated by a wide barrier to prevent tunneling. The quantity $d$ is the center-to-center distance and $L_z$ is the width of the right QW.

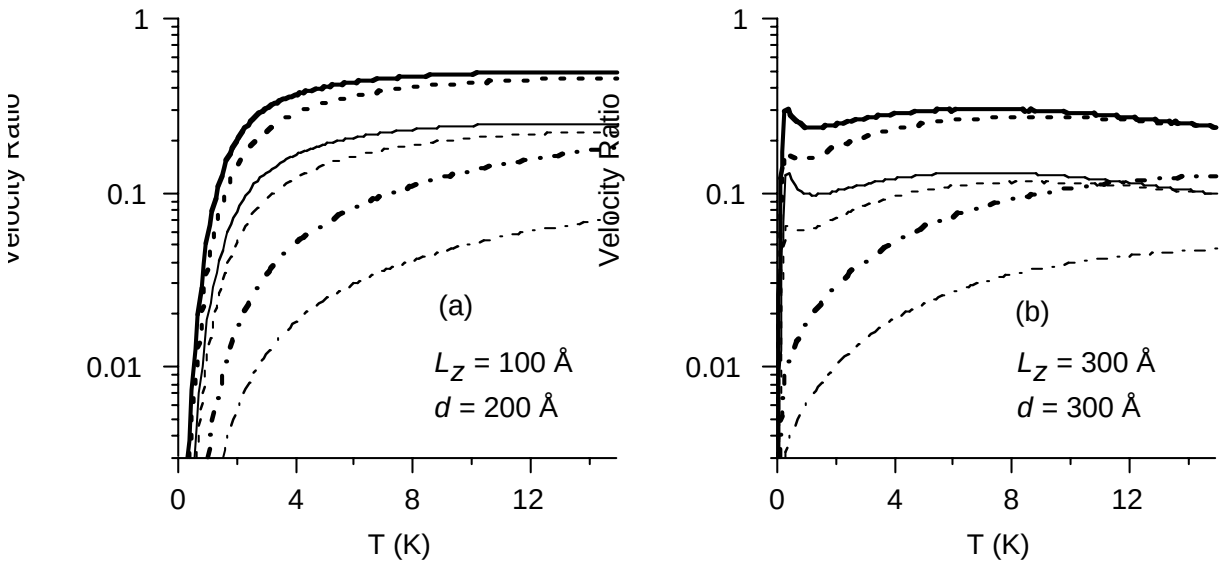


**Figure 2.** Ratio of the drift velocities of the excitons and the electrons with exciton-phonon and exciton-surface-roughness scattering for two sets of parameters (a) $d$ = 200 Å, $L_z$ = 100 Å and (b) $d$ = 300 Å, $L_z$ = 300 Å for $N_{2D} = 10^{11}$ cm$^{-2}$ (thick curves) and $N_{2D} = 2310^{11}$ cm$^{-2}$ (thin curves). The hole mass equals $m_h = 0.45m_o$ (solid curves), $m_h = 0.35m_o$ (dashed curves), and $m_h = 0.14m_o$ (dash-dotted curves). The actual hole mass is (a) $m_h < 0.14m_o$ in the narrow QW and (b) $m_h < 0.45m_o$ in the wide QW.

# Nanomechanics & Nanomanipulation

# *Temperature Dependent Mechanical Properties of Materials: A Study Using Micromechanical Oscillators*

*by* **J. P. Sullivan, D. A. Czaplewski, T. A. Friedmann, and J. R. Wendt**

**Motivation**—Micromechanical oscillators have been developed for an increasing number of applications, including miniaturized acoustic, chemical or biological sensors (e.g., for Homeland Security), clocks and filters for high frequency electrical circuits, and resonant detectors of small force for scanning probe microscopy. For many of these applications, the critical signal to be measured is the absolute resonant frequency or a change in the resonant frequency of the oscillator. One confounding issue is that the resonant frequency of an oscillator changes with changing temperature due to the temperature dependence of the mechanical properties of the material. This work describes the development of an experimental capability to measure the temperature dependence of the full elastic properties of a thin film material through the use of flexural and torsional micromechanical oscillators.

**Accomplishment**—Flexural and torsional micromechanical oscillators were fabricated out of tetrahedral amorphous carbon, ta-C, which is one material that has been used in a variety of micromechanical oscillator applications. The flexural oscillators were comprised of cantilevers of varying lengths, from 10s to 100s of microns. The torsional oscillators were fabricated as paddle oscillators with beam widths of 0.5 microns and lengths of 10s of microns (see Fig. 1). E-beam lithography and surface micromachining processes were used to create the structures. These micromechanical oscillators were then mounted onto a resistive heater element bonded to a piezoelectric actuator with the entire system being inside a vacuum system. Light interferometry was used to measure oscillator resonant frequencies. Measurements of the oscillator properties were made over the temperature range from 300 K to 873 K. The Young's modulus, E, and shear modulus, G, were evaluated at each temperature by fitting the data of oscillator frequency as a function of oscillator length and applying linear elastic beam theory. Ta-C is a completely amorphous material, so it behaves as a true isotropic solid with only two independent elastic constants. The Poisson's ratio, $\nu$, is calculated using $\nu = 0.5(E/G)-1$. Similarly, the three elastic constants, $C_{11}$, $C_{12}$, and $C_{44}$ may also be obtained from knowledge of E and G. With the elastic constants thus obtained, the temperature dependence may be expressed using $2^{nd}$ order polynomial fits. Figure 2 shows the temperature dependent Young's and shear moduli of ta-C and the subsequent polynomial fits. In both cases, a decrease in modulus of about 3% was observed over the temperature range from 300 K to 873 K.

**Significance**—Knowledge of the temperature dependent mechanical properties of a micromechanical oscillator enables the complete prediction of the oscillator resonance frequency at any temperature. This information is critical in order to account for and adjust for temperature-induced drift of the oscillator frequency–an important correction for oscillators used as frequency sources/filters or for sensing applications. The approach described here to obtaining the temperature dependent properties of thin film micro-mechanical oscillator materials is quite generic, and currently studies are being extended to the characterization of amorphous silicon nitride and polycrystalline diamond oscillators.

**Sponsors for various phases of this work include**: Laboratory Directed Research & Development and DOE Office of Basic Energy Sciences

**Contact:** John P. Sullivan, Nanostructure & Semiconductor Physics, Dept. 1112
Phone: (505) 845-9496, Fax: (505) 844-4045, E-mail: jpsulli@sandia.gov

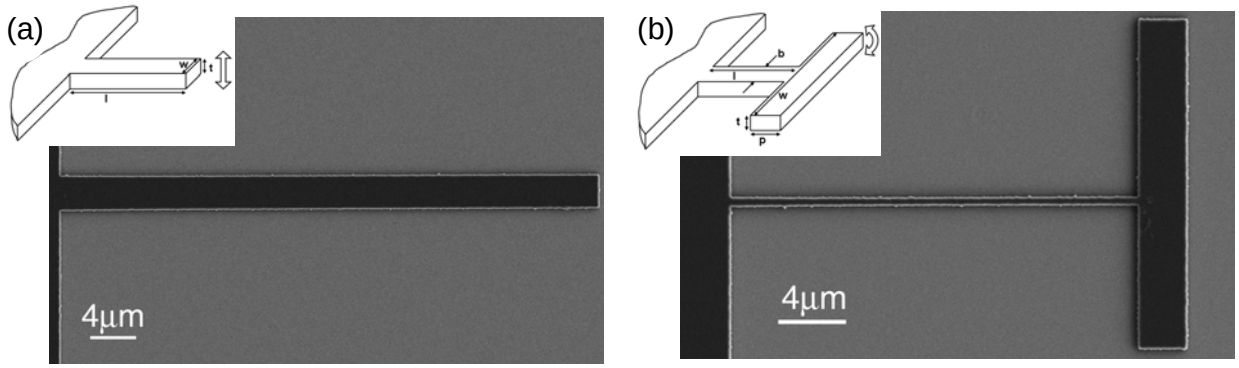


**Figure 1.** Schematic (insets) and SEM images of tetrahedral amorphous carbon (a) flexural oscillators and (b) torsional oscillators that were used in this study.

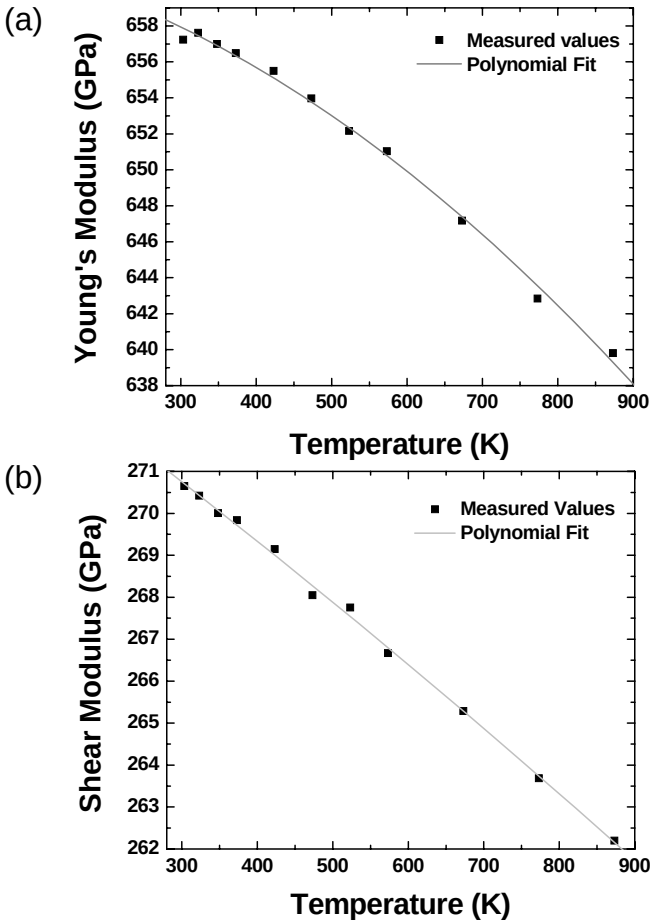


**Figure 2.** The measured temperature-dependent (a) Young's and (b) shear moduli of tetrahedral amorphous carbon. The solid lines are 2nd order polynomial fits to the data.

# *Stress Creation During NiMn Electrodeposition*

*by* **S. J. Hearne, J. A. Floro, M. A. Rodriguez, R. T. Tissot, C. S. Frazer, L. Brewer, P. Hlava, S. Foiles, and A. Feldhaus**

**Motivation**—Stress creation during thin film deposition has been a concern for over a century due to the limits it places on applications. This is particularly true for electrodeposited films such as Ni and its alloys, for which stresses range from hundreds of MPa compression to hundreds of MPa tension depending on the bath chemistry and growth conditions. Recent efforts to increase the high-temperature (~600°C) strength of Ni have utilized co-deposition of 1 to 2 at% Mn during plating, but the resultant alloy possesses a significantly higher tensile stress. To overcome this, pulse plating procedures were developed that reduce the mean film stress. However, in these studies, there were no investigations into the actual stress evolution during deposition or the possible sources of these stresses. In this report, we have correlated the stress evolution during electrodeposition of NiMn with *ex-situ* microstructural measurements to examine the source of stress active during electrodeposition.

**Accomplishment**—The stress evolution and microstructure of NiMn electrodeposited from a sulfamate-based bath was investigated as a function of Mn concentration and current density. As shown in Fig. 1, the NiMn stress evolution with film thickness exhibited an initial high transitional stress region, followed by a region of steady-state stress with a magnitude that depended on deposition rate, similar to the previously reported stress evolution in electrodeposited Ni (Hearne and Floro, *J. Appl. Phys.* **97**, 014901-1 (2005)). Based on transmission electron microscopy (TEM) analysis, it was determined that the transition stress was a result of the (111) NiMn grains growing semi-coherently with the underlying (111) Au grains, which resulted in a tensile stress during the early stages of growth. The origins of the steady-state stress are more difficult to identify. Figure 2 shows that the incorporation of increasing amounts of Mn resulted in a linear increase in the steady-state stress. Neither x-ray diffraction (XRD) nor TEM found any significant change in microstructure as a function of Mn concentration. Additionally, the observed increase in resistivity with Mn content was consistent with the weighted average resistivity of the two constituents. The only other trait that was observed to track with the manganese content was the XRD measured micro-stress, which was likely the result of lattice distortions due to the substitutional incorporation of Mn. We are currently performing atomistic simulations to verify this hypothesis. To conclude, we observed that the origins of the steady-state stress were not due to the microstructure, but were likely the result of point defect generation, and/or grain boundary coalescence. Research is ongoing to validate this hypothesis.

**Significance**—Understanding the origins of stress is critical in setting the bounds for device fabrication and application. This is particularly true for systems such as NiMn, where the primary goal is enhanced mechanical strength. This work has provided a foundation for the understanding of the physical processes creating stress during growth as a function of deposition conditions. Through this enhanced understanding, we will help to make more reproducible microsystems from electro-deposited metals–like the components formed in precision molds by the LIGA process and metal MEMS structures used in RF communications.

**Sponsors for various phases of this work include:** DOE Office of Basic Energy Sciences, Laboratory Directed Research & Development, and Nuclear Weapons/LIGA

**Contact:** Sean J. Hearne, Nanostructure & Semiconductor Physics, Dept. 1112
Phone: (505) 845-0804, Fax: (505) 844-1197, E-mail: sjhearn@sandia.gov

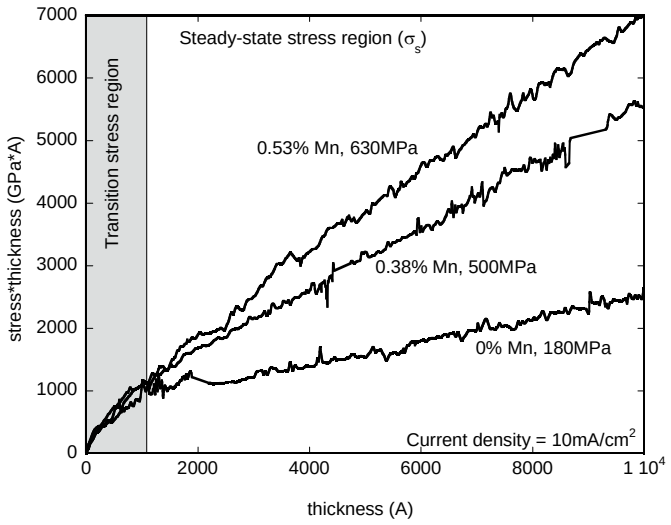


**Figure 1.** Stress-thickness versus thickness plot for three samples grown using a 5.0 g/L Mn bath. The upper and lower curves were deposited at constant rates of 15 mA/cm$^2$ and 3 mA/cm$^2$, respectively, and the current density in the middle curve was cycled between 15 mA/cm$^2$ and 3 mA/cm$^2$, for 0.67 sec. and 4.4 sec., respectively.

.

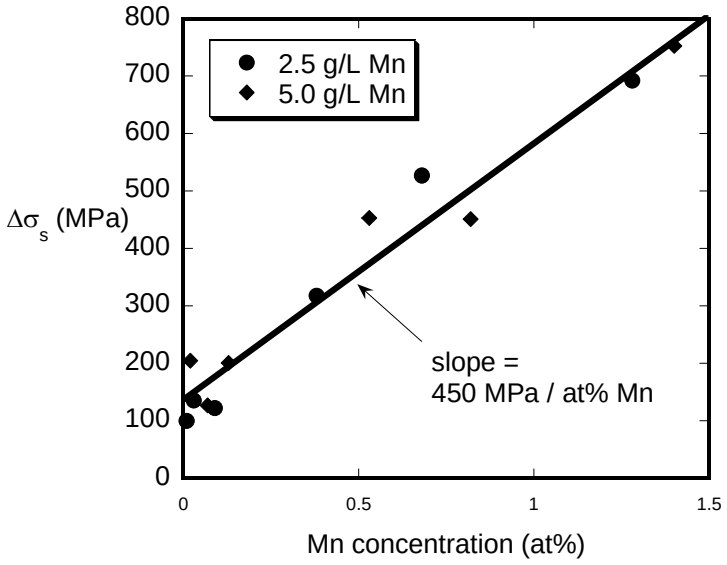


**Figure 2.** Difference between the $\sigma_S$ stress as function of Mn concentration at constant current density for the three baths, 0 g/L Mn, 2.5 g/L Mn, and 5.0 g/L Mn.

# *A Local-Probe Analysis of the Rheology of a "Solid Liquid"*

*by* **J. E. Houston**

**Motivation—**Polymer composites have become increasingly important in materials science and engineering and have found ever-broadening application in commercial products. Fiber and particulate-reinforced composites show considerable improvement in overall performance. However in both cases, matrix aging can cause serious degradation in long-term performance. In order to study the details of the aging process it is necessary to go beyond bulk mechanical testing methods and explore the local adhesive and viscoelastic properties in the interphase region near the dispersed-agent/matrix boundary and local-probe techniques offer potential in this area.

**Accomplishment—**We have recently taken advantage of the unique capabilities of the Sandia-developed Interfacial Force Microscope (IFM) to demonstrate its application to the local viscoelastic properties of a material which is often referred to as a "solid liquid" but is more commonly known as Silly Putty™ (SP) (Registered trademark of Binney and Smith, Inc.). This material was chosen as a test case, not only because of its interesting properties, but because it represents a "worst-case" example of a viscoelastic material from an experimental standpoint. As any child born after 1950 knows, SP readily bounces off a hard surface but when sitting on the same surface it gradually deforms into a thin pancake. In addition, it tends to stick to most any surface. This combination makes the material very difficult to study and certain strategies have to be developed in order to produce quantitative results.

In recent experiments, we have used a 50 micron diameter spherical tip, Fig. 1, and relaxation measurements in order to acquire the frequency response of the material. We first establish an initial contact, the dimensions of which can be measured optically (Fig. 2). After this contact is established, the tip is then suddenly pushed further into the surface by a small amount, while recording the force as the SP responds to being deformed. The result is shown in Fig. 3. From this data we see that the material will support a high force over only short times, but rapidly relaxes to insignificant levels within a few seconds. The relaxation data can be made quantitative in terms of the material's relaxation function, i.e., stress as a function of time, through the use of a classic contact-mechanics formalism by knowing the shape and size of the tip, the initial contact dimensions and the extent of the step deformation. In addition, the time dependence of Fig. 2 can be cast in terms of the frequency response for both the real and imaginary components of the shear modulus through the use of a standard Fourier analysis. Figure 4 shows the results of this process directly compared to those obtained by a commercial vibrating pendulum rheometer. In this instrument, a bulk SP sample is placed between two pads, one of which oscillates with the pendulum and the data of Fig. 4 consists of 10 individual measurements of amplitude and phase of the SP deformation at each frequency. In contrast, the IFM results were done on a relatively local level and the data acquisition for the entire frequency response took less than 10 sec. Although these measurements were not taken at a level necessary to analyze the interphase of a typical fiber-reinforced composite, there is no reason why this level cannot be achieved with the present instrument.

**Significance**—This work shows that truly nano-scale rheology is possible with presently available IFM technology.

**Sponsors for various phases of this work include:** DOE Office of Basic Energy Sciences

**Contact:** Jack E. Houston, Surface & Interface Sciences, Dept. 1114
Phone: (505) 844-8939, Fax: (505) 844-5470, E-mail: jehoust@sandia.gov

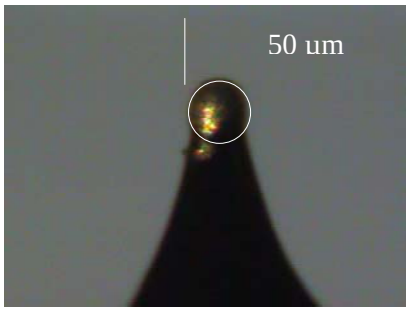


**Figure 1.** The IFM tip is a flame-annealed glass rod Au platted to enable coating with a passivating film.

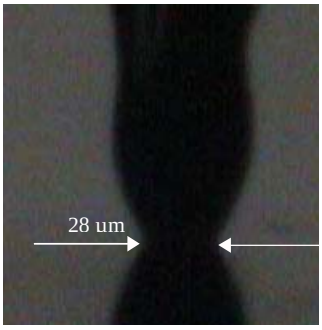


**Figure 2.** The IFM tip is at the top in contact with SP at the arrows indicating the contact diameter. Below is the reflection of the tip off the SP surface.

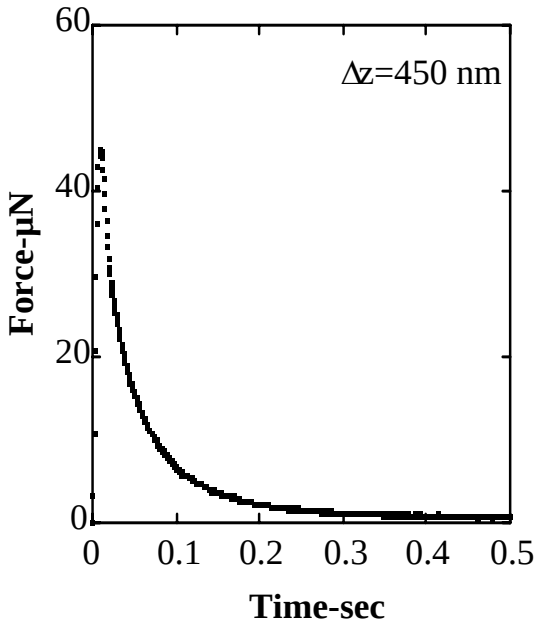


**Figure 3.** Relaxation results for a 450 nm step deformation at t=0 sec showing a rapid exponential relaxation after reaching a high initial force.

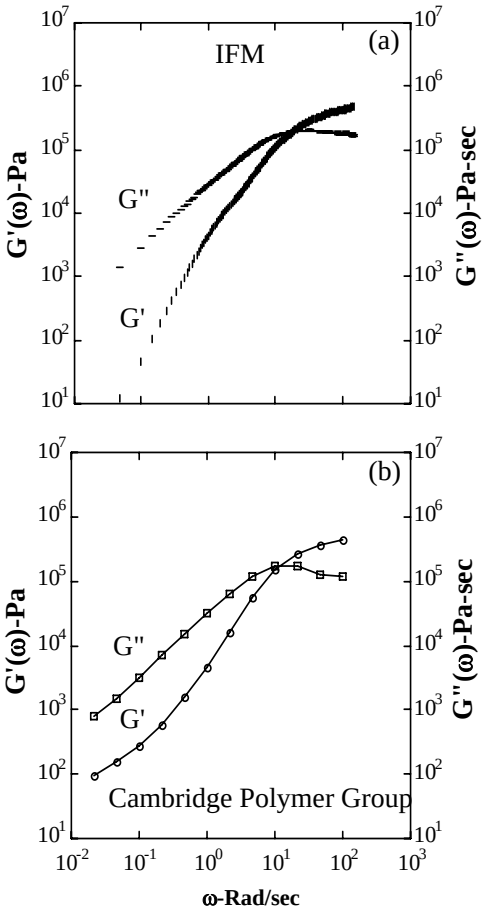


**Figure 4.** (a) the SP frequency response obtained from the analysis and (b) the point-by-point response obtained with a commercial vibrating-pendulum rheometer by the Cambridge Polymer Group, Boston, MA.

# *Cavitation in the Interaction Between Superhydrophobic Surfaces*

*by* **F. B. van Swol, J. E. Houston, S. Singh, P. Shah, and C. J. Brinker**

**Motivation—**The unique interaction of hydrophobic surfaces in water has been implicated in such diverse effects as protein folding, micelle assembly and the large-scale, ordered assembly of specifically functionalized components. In addition, there has been considerable debate over the last 20 or so years over the so called long-range hydrophobic force, which is often seen to decay exponentially with interfacial separation, is stronger by one or two orders of magnitude than that expected from the van der Waals force and ranges over several tens of nm. We have probed the interaction of Sandia-developed superhydrophobic (SH) surfaces in water with the Interfacial Force Microscope (IFM) in an attempt to shed light on this elusive force and have compared the results with state-of-the art calculations.

**Accomplishment—**The experiments consist of using the IFM to measure the force as a SH tip and surface approach. The SH surfaces are a porous silica gel functionalized to be hydrophobic. The several 100 nm scale surface roughness renders these surfaces superhydrophobic in a manner similar to a Gecko's foot pad or the Lotus leaf. Water contact angles near 170° indicate that water does not want to be near this surface. As the IFM tip approaches, we observe the sudden nucleation of a cavity (bubble) between the tip and sample creating a large attractive force on the tip (Fig. 1). Continuing the tip motion inward signals tip/substrate contact by the appearance of a rapidly increasing repulsive force. This allows the IFM to obtain the distance from contact over which the cavity nucleates. Surprisingly, this distance is often found to be larger then a micron, a fact which is hard to accept on the basis of simple surface tension arguments.

In order to try to get a better understanding of the process and the role of fluctuations, we have undertaken molecular dynamics simulations of cavitation. We studied cavitation in a slit-like pore with wall-fluid interactions chosen to produce a contact angle of zero degrees (complete wetting). To mimic the experiment an SH stripe was created on each wall. Two hemicylindrical vapor bubbles start to develop. Mechanical and chemical equilibrium conditions imply that these two new menisci must grow and adopt the same radius of curvature as the two outer vertical menisci. This process eventually leads to merging, i.e. cavitation. This phase transition is preceded by intense fluctuations that ultimately produces the rupture of the thin liquid film. The vapor pressure of the newly emerged vapor bridge is initially too high, and the system quickly restores mechanical equilibrium by simultaneously expanding the bubble and changing the curvature of the menisci to convex.

**Significance**—Although cavitation, or capillary evaporation as it is sometimes called, is expected to occur when two SH surfaces are brought closely together, the gap size for which this takes place in the IFM experiment is larger by several orders of magnitude than would be predicted on the basis of simple surface tension arguments. Although the vapor bridge connecting both surfaces may be the stable configuration when the gap is approximately micron-sized, one would ordinarily expect a configuration of the liquid film separating the two independent vapor regions to continue to be quite stable, indicative of the presence of a free energy barrier. The experimental observations suggest therefore that the liquid film must somehow be destabilized. Fluctuations are a likely candidate for this scenario, and this is substantiated by the MD results, albeit that the simulation represents a much smaller length scale. Visual observations also indicate significant density fluctuations just prior to cavitation.

**Sponsors for various phases of this work include:** DOE Office of Basic Energy Sciences, Air Force Office of Scientific Research, and Laboratory Directed Research & Development

**Contact:** Frank B. van Swol, Surface & Interface Sciences, Dept. 1114
Phone: (505) 272-7631, Fax: (505) 844-4045, E-mail: fbvansw@sandia.gov

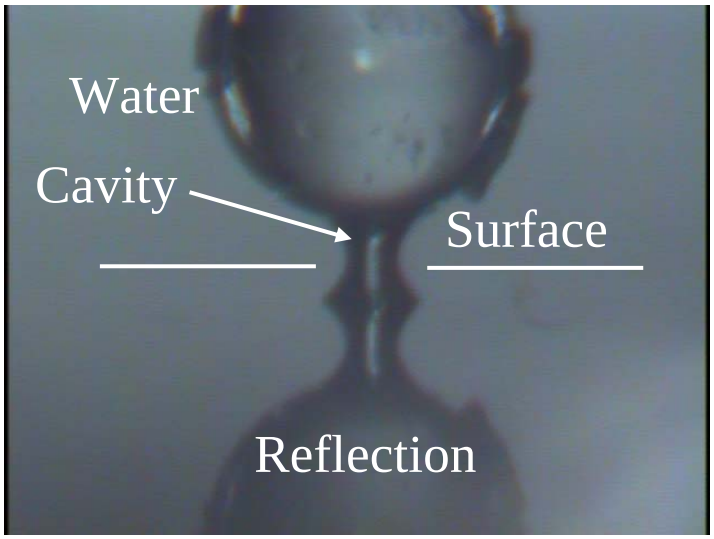


**Figure 1.** The IFM tip is shown at the top, while the SH surface is indicated by the horizontal lines. The tip and cavity reflection is shown at the bottom of the figure.

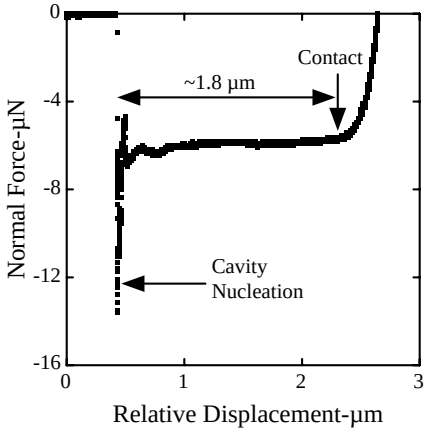


**Figure 2.** The IFM tip is approaching from the left and nucleates the cavity creating a large attractive (negative) force. It then moves an additional 1.8 µm before contacting the substrate.

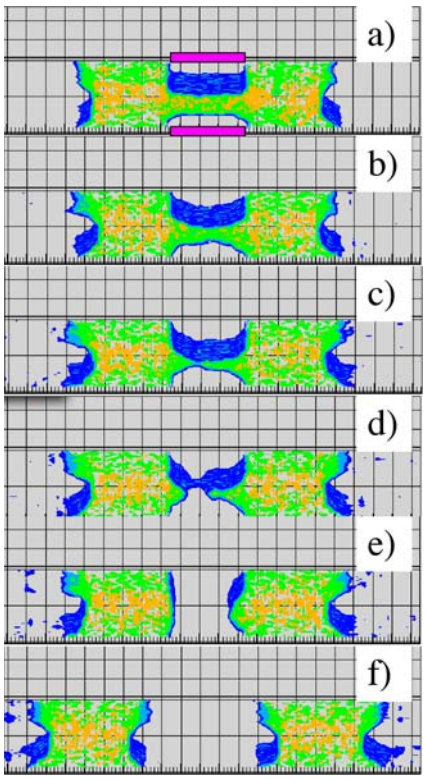


**Figure 3.**. Molecular dynamics results of cavitation inside a capillary slit. At time is zero a SH patch (indicated by purple bars) is created on the walls of an otherwise hydrophilic slit. The SH patch stimulates the growth of two vapor bubbles (a-c), separated by a thin liquid bridge. The liquid bridge ruptures (c-d) corresponding to cavitation. Panel (f) shows the final equilibrium state when all menisci have reached the correct curvature.

# *Nanomanipulation Using Combined Scanning Probe Microscope and Scanning Electron Microscope*

*by* **B. S. Swartzentruber**

**Motivation**—Nano-scale structures have properties that differ from bulk values due to their inherently small size and their high surface-to-bulk atom ratio. Potential applications using nanostructures include: high frequency resonators; novel electronic devices; and highly sensitive chemical sensors; among others. One stumbling block in the development of such devices is the difficulty to precisely position nanostructures exactly where they are needed. The problem is two-fold–imaging the nanostructures and their surroundings, and manipulating them on the nanometer length scale.

**Accomplishment**—I designed and constructed a fully functional scanning probe microscope (SPM) inside the imaging chamber of a commercial (LEO-1430) scanning electron microscope (SEM). Using piezoelectric actuators, this SPM instrument can position the apex of a probe tip with sub-nm precision within ~10 x 10 x 10 $\mu^3$. Mounting the SPM on three orthogonal, electronically-driven, translation stages allows coarse positioning over 7 mm in three dimensions. The SEM images the probe tip and nanostructures in real-time providing visual feedback for manipulation.

The initial work with this system involved the manipulation of various nano-whisker/wire samples–multi-walled carbon nanotubes, semiconducting tungsten-oxide whiskers, silicon whiskers, and germanium whiskers. All of these samples were grown on substrates containing catalytic nano-particles, resulting in a 'nest' of whiskers, anchored to the substrate, ranging in size from 20 to 100 nm in diameter and 300 to 10,000 nm in length, depending on the material system and growth parameters.

Building a three-dimensional structure occurs in two stages. First, the probe tip is used to extract a single whisker from the nest. Second, the whisker is transferred and placed in an appropriate position. In Fig. 1, I show a hooked probe tip pulling a germanium whisker from the nest. Once extracted, the whisker is moved to another area where, either its electronic properties are determined through IV measurements through the whisker between the probe and a gold pad, or it is positioned in a well-defined structure. Figure 2 shows the germanium whisker being placed across the gaps in a lithographically defined circuit element.

**Significance**—Using custom actuation hardware and software, I am determining the control parameters for pick up, transfer, and placement of nanowires. I can also probe the electrical characteristics of individual nanowires to explore their conduction mechanisms. The visualization afforded by SEM coupled with the precise placement of scanning-probe-like actuators enables a top-down approach to fabricate and manipulate nanostructures unattainable by conventional means. This combined SEM-Nanomanipulation capability is among only a handful world-wide.

**Sponsors for various phases of this work include:** DOE Office of Basic Energy Sciences/Robotics

**Contact:** Brian S. Swartzentruber, Surface & Interface Sciences, Dept. 1114
Phone: (505) 844-6393, Fax: (505) 844-5470, E-mail: bsswart@sandia.gov

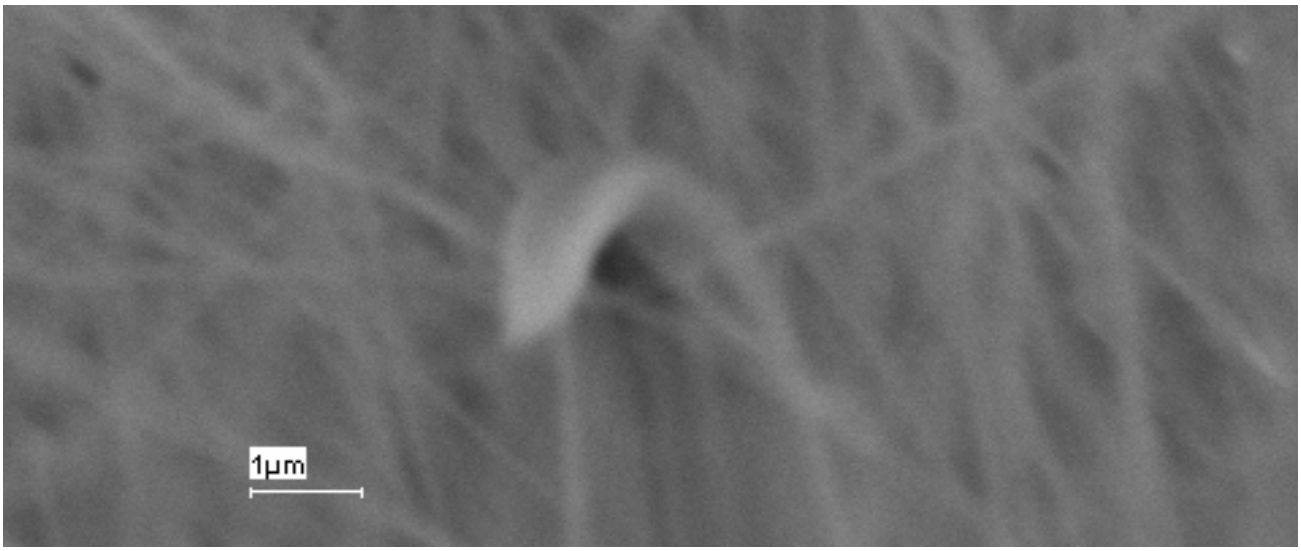


**Figure 1.** Extraction of a germanium nano-whisker using a hooked probe tip.

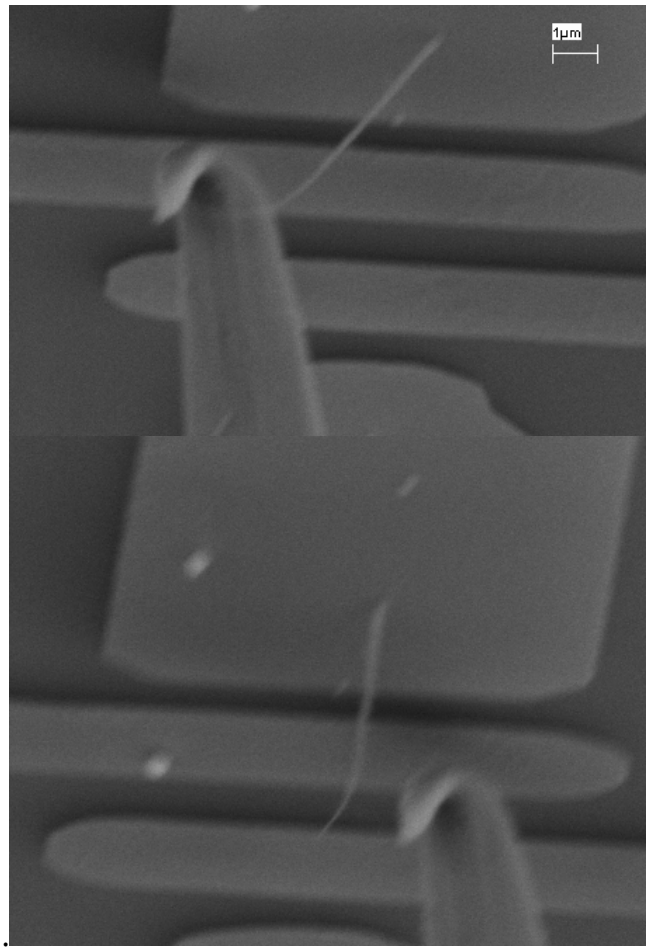


**Figure 2.** Placement of the germanium whisker across the gap in a gold circuit. Top: in contact with the upper pad. Bottom: after placement and release from probe tip.

# Wide Bandgap Semiconductor Materials & Devices

# *Improved Power and Reliability of AlGaN-based Deep Ultraviolet LEDs*

*by* **M. H. Crawford, A. A. Allerman, A. J. Fischer, S. R. Lee, and K. H. A. Bogart**

**Motivation—**Solid-state deep ultraviolet (UV) light emitting diodes (LEDs) are needed for a range of applications, including fluorescence-based sensing of bioagents, non-line-of-sight communications, and portable water purification systems. Recently developed deep UV (270-280 nm) LEDs based on AlGaN semiconductor alloys show promise to meet the requirements of these applications, but to date have been limited in both output power and device lifetime. Our research has focused on advancing AlGaN epitaxial material quality to enable significant LED performance advances in these critical areas.

**Accomplishment—**A key challenge to advancing the performance of AlGaN LEDs is reducing the high density of threading dislocations which are predicted to act as non-radiative recombination centers and may contribute to device failure. These defects originate at the initial stage of epitaxial growth with the nucleation of AlN epilayers on lattice-mismatched sapphire substrates. Our materials optimization efforts have focused on modifying the metal-organic vapor-phase epitaxial growth process at this critical nucleation stage to reduce dislocation densities. Through this optimization process, we have succeeded in reducing the dominant edge-component dislocation density from ~$3x10^{10}$ $cm^{-2}$ to ~$7x10^{9}$ $cm^{-2}$. We fabricated AlGaN LEDs on these lower dislocation density AlN epilayers by employing a p-i-n LED structure shown schematically in Figure 1. In Figure 2, we show the light output versus current (L-I) and current-voltage (I-V) characteristics of a 1 mm x 1 mm sized device with emission at 276.8 nm. For 600 mA DC current operation, this device yielded 2.4 mW of optical output power, exceeding the output of our previous devices by a factor of two.

While the exact mechanisms that limit AlGaN LED reliability are not completely understood, our device lifetime studies revealed distinct signatures associated with optical power degradation. LEDs operated under constant current conditions and demonstrating at least 50% output power degradation have consistently shown increased current leakage. Non-uniform light emission patterns were also observed in some cases. We hypothesized that threading dislocations may contribute to the current leakage, and non-uniform current injection due to epitaxial surface roughness may also factor into device degradation. We therefore implemented new p-AlGaN and p-GaN growth conditions for improved surface morphologies in concert with our efforts to lower dislocation densities. Device lifetime studies were performed on 300 μm x 300 μm sized LEDs employing these material improvements. The devices were operated at 30 mA DC and yielded output powers up to 0.18 mW. In Figure 3, we show lifetest data from one such LED that demonstrated less than 50% power degradation over 1500 hours. This performance shows dramatic improvement beyond the 10's-100's of hour lifetimes of previous devices.

**Significance**—The demonstration of compact, solid-state deep UV sources at milliwatt power levels and with improved reliability has accelerated their implementation into fluorescence-based bioagent detectors and non-line-of-sight communications systems. These devices offer new capabilities for applications of great interest to national security.

**Sponsors for various phases of this work include:** Defense Advanced Research Projects Agency/Semiconductor Ultraviolet Optical Sources and Laboratory Directed Research & Development

**Contact:** Mary H. Crawford, Semiconductor Material & Device Sciences, Dept. 1123
Phone: (505) 284-9380, Fax: (505) 844-3211, E-mail: mhcrawf@sandia.gov

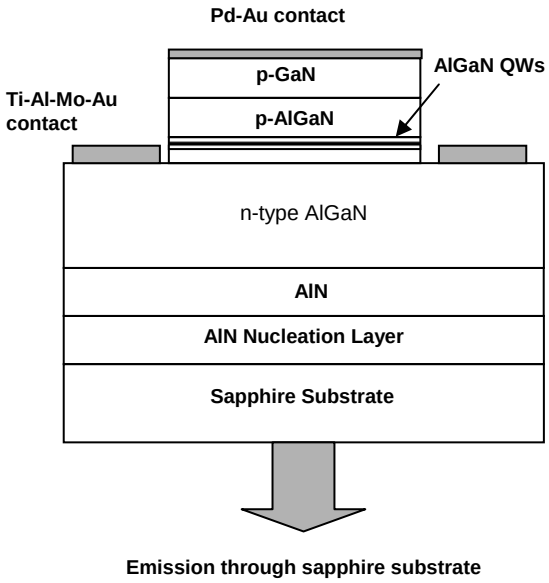


**Figure 1.** Schematic of a deep UV AlGaN LED. The devices reported herein consist of three 2 nm thick $Al_{0.47}Ga_{0.53}N$ quantum wells with 7 nm thick $Al_{0.58}Ga_{0.42}N$ barriers, a 25 nm thick $Al_{0.70}Ga_{0.30}N$ electron block layer on the p-side of the device and a 1.4 µm thick n-type $Al_{0.61}Ga_{0.69}N$ layer. Al compositions and layer thicknesses are estimated from growth calibration structures and XRD measurements.

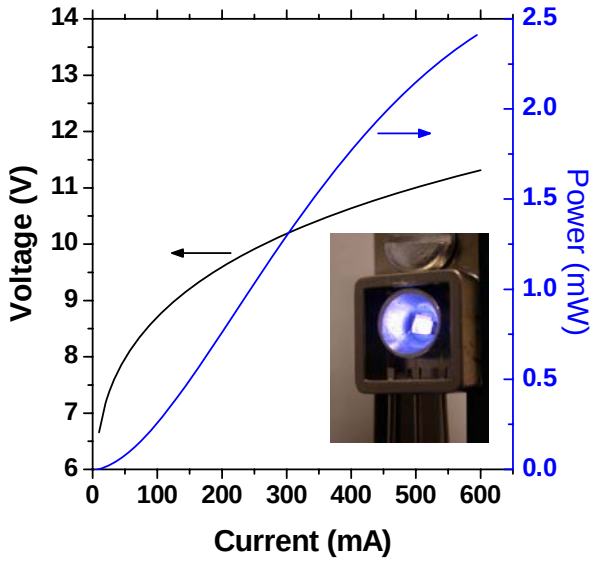


**Figure 2.** L-I-V data for a 1 mm x 1 mm LED with peak emission at 276.8 nm at 600mA. The inset shows a photograph of the flip-chip bonded LED packaged in a TO-257 header with an aluminum reflector.

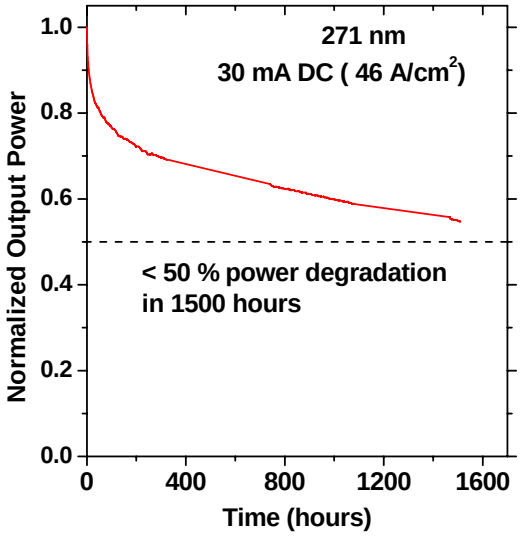


**Figure 3.** Lifetest data for a 300 µm x 300 µm sized device at 30 mA with peak emission at 271 nm. Output power is monitored by a silicon photodiode.

# *Photonic Crystals for Improved InGaN LED Efficiency*

*by* **A. J. Fischer, J. R. Wendt, J. J. Wierer[1], M. R Krames[1], D. Li[2], S. R. J. Brueck[2], R. J. Shul, S. H. Kravitz, K. W. Fullmer, and C. F. Schmidt**

**Motivation—**Light Emitting Diodes (LEDs) based on InGaN will be used in future high efficiency lighting applications. Currently available semiconductor-based white light emitters, which are based on InGaN LEDs, have efficiencies better than incandescent light bulbs, but still much lower than fluorescent tubes. The efficiency is limited by poor internal quantum efficiency as well as poor light extraction efficiency. Photonic crystals offer a potential solution to both of these problems. Internal quantum efficiency can be enhanced via the Purcell effect where the radiative recombination rate is increased by placing the quantum well emitters inside an optical cavity. At the same time, a photonic crystal can be used to improve light extraction by diffracting waveguided modes out of the semiconductor.

**Accomplishment—**In addition to problems associated with low internal quantum efficiency, InGaN LEDs are limited by the extraction of light from the high index semiconductor chip. Light is generated inside of the semiconductor and bounces around due to total internal reflection. There is a high probability that the light will be absorbed before it can escape from the semiconductor. Figure 1 shows a schematic diagram of a photonic crystal LED. For typical InGaN LEDs, a large fraction of the light is emitted into waveguided modes internal to the semiconductor rather than into radiation modes. By incorporating a photonic crystal into an InGaN LED these waveguided modes can be extracted improving the total device efficiency.

Fabrication of photonic crystals in GaN is complicated by the difficulty of etching GaN, which is extremely hard and chemically inert. Photonic crystals are fabricated by dry-etching GaN using a Cl-based plasma. Submicron patterning is performed using e-beam, interferometric, or nano-imprint lithography. Figure 2 shows a focused-ion-beam scanning electron microscope (FIB-SEM) image of a photonic lattice etched into GaN. The photonic lattice pattern shown here is a triangular lattice with a pitch of 205nm and a hole diameter and depth of 110nm and 380nm, respectively. The straight sidewalls and high aspect ratio (depth to width) of greater than 3:1 are very desirable features for efficient light extraction.

Photonic crystal LEDs have been fabricated by combining LED processing and photonic crystal processing to make an electrically-injected InGaN LED. Figure 3 shows the far field emission patterns for a photonic crystal LED compared to a control LED with no photonic crystal. The photonic crystal LED shows a strongly modified far field pattern with a triangular symmetry. This pattern is due to the extraction of waveguided modes. InGaN LEDs with photonic crystals showed a 1.5X increase in efficiency compared to control LEDs.

**Significance**—Many InGaN LED performance improvements are still required including increased efficiencies, higher power lamps, and lower cost per lamp. Photonic crystals have the potential to dramatically increase InGaN LED efficiency. This work is a first step towards improving the efficiency of InGaN LEDs such that white light efficacies of 200 lm/W will become a reality.

[1]Lumileds Lighting, [2]University of New Mexico

**Sponsors for various phases of this work include:** Laboratory Directed Research & Development and DOE Office of Energy Efficiency and Renewable Energy (EERE)

**Contact:** Arthur J. Fischer, Advanced Materials Sciences, Dept. 1123
Phone: (505) 844-6543, Fax: (505) 844-3211, E-mail: ajfisch@sandia.gov

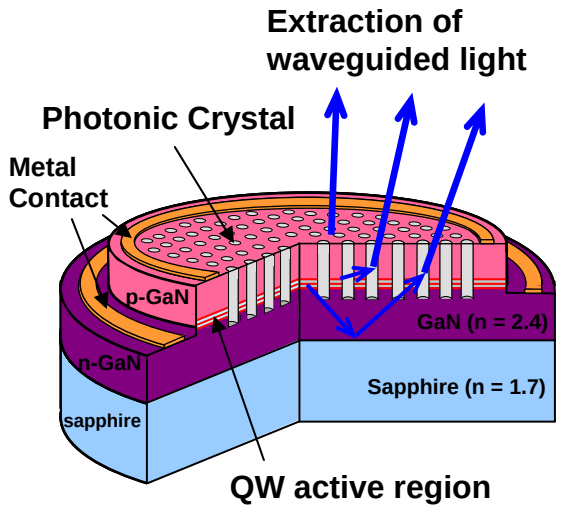


**Figure 1.** Schematic diagram of an InGaN photonic crystal light emitting diode.

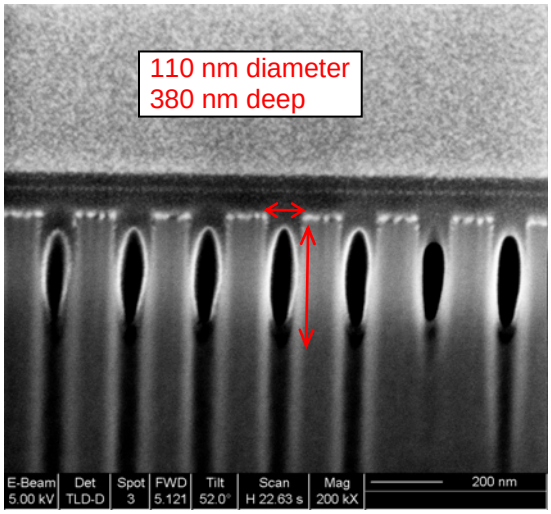


**Figure 2**. Focused ion-beam scanning electron microscope image of a photonic crystal etched in GaN. This photonic crystal has a lattice constant of 205nm.

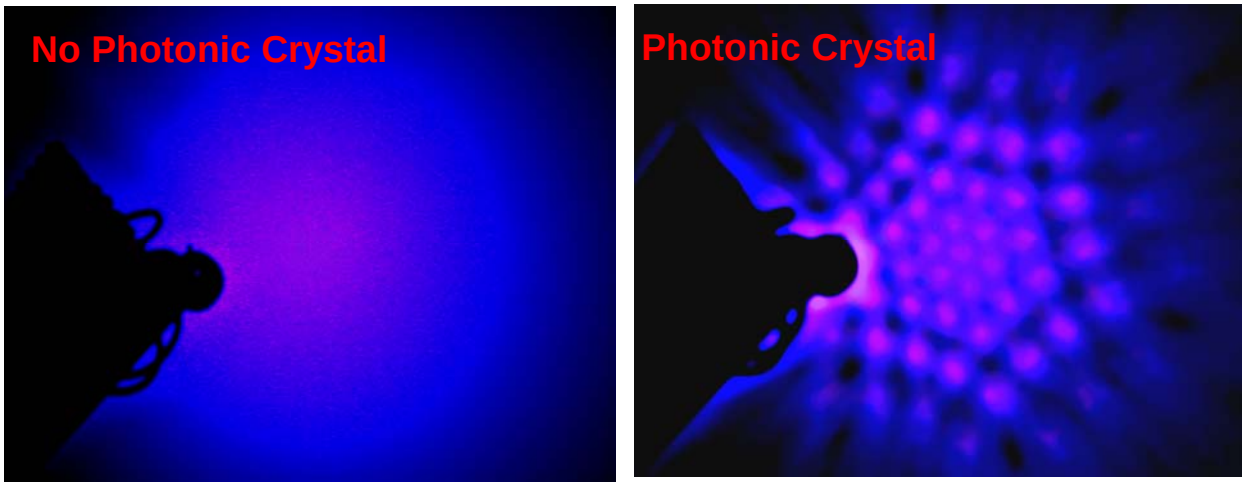


**Figure 3.** Far field emission patterns from a photonic crystal light emitting diode (LED) and a control sample with no photonic crystal. The photonic crystal LED has a strongly modified emission pattern due to scattering of waveguides modes out of the LED chip.

# *Optimization of Indium Incorporation in InGaN Multi-Quantum Wells*

*by* **D. D. Koleske, S. R. Lee, A. J. Fischer, M. E. Coltrin, M. H. Crawford, and M. J. Russell**

**Motivation—**Light-emitting diodes (LEDs) are poised to replace traditional incandescent and fluorescent lights by virtue of their potential for more energy-efficient generation of white light. The most efficient solid-state white-lighting sources will combine red, blue, and green LEDs. While efficient red and blue LEDs exist, high-efficiency green LEDs have proven difficult to produce using the alloys of either AlInGaP, or more recently, InGaN.

Two major issues limit the structural quality and light-emitting efficiency of InGaN/GaN materials presently grown by MOCVD. First, lower growth temperatures must be used to incorporate the higher indium compositions needed for deep-green emitters. Second, as the composition increases, the lattice-mismatch strain of InGaN epitaxy on GaN also increases. Lower growth temperatures combine with higher InGaN strains to cause a variety of materials defects and nanostructures as these alloys push towards green. The present research seeks to understand both the mechanisms leading to defect formation and the impact of these defects on luminescent efficiency.

**Accomplishment—**Recent work has focused on the successful installation of a new Veeco D-125 MOCVD reactor and subsequent optimization of this reactor to grow state-of-the-art InGaN materials for fundamental studies of luminescence. Optimization studies have examined the influence of growth parameters such as temperature, pressure, growth rate, precursor flow, and carrier-gas flow on both indium incorporation and attendant materials defects. These studies have led to Sandia's first multi-milliwatt blue LEDs and Sandia's first green LEDs emitting near 515 nm.

Structural and optical feedback for these studies was provided by x-ray diffraction (XRD), atomic-force microscopy, Nomarski optical microscopy, photoluminescence spectroscopy (PL), and electroluminescence quick tests. Figure 1 shows typical XRD data for a multi-quantum well (MQW) that emits blue-green light at 490 nm. The MQW structure was evaluated using dynamical diffraction simulations of the measured XRD rocking curve. The excellent agreement between simulation and experiment indicates the presence of a structurally coherent MQW superlattice containing few v-defects, indium-metal inclusions, or misfit dislocations. Figure 2 shows the PL-emission wavelengths observed for various MQW samples grown during our studies. As indium composition increases, the redshift of the MQW emission relative to the bulk bandgap also increases. Since indium compositions beyond ~20% are difficult to obtain, this well-width-tunable redshift is crucial for reaching deep-green wavelengths. The redshift results from piezoelectric Stark shifts and InGaN-alloy compositional fluctuations that are the subject of ongoing studies. Finally, Fig. 3 shows the dramatic effect of epitaxial strain on indium incorporation. While coherent InGaN layers are indeed limited to ~20% indium, strain-relaxed layers readily incorporate up to 40% indium. Thus, efficient green LEDs may require improved substrates with a better lattice match to InGaN.

**Significance**—Our research program is providing the fundamental knowledge needed to make energy-efficient solid-state white lighting a practical reality. Such a reality could ultimately reduce American energy expenditures for lighting by as much as $30 billion/year.

**Sponsors for various phases of this work include:** DOE Office of Basic Energy Sciences and Laboratory Directed Research & Development

**Contact:** Daniel D. Koleske, Advanced Materials Sciences Department, 1126
Phone: (505) 284-4531, Fax: (505) 844-3211, E-mail: ddkoles@sandia.gov

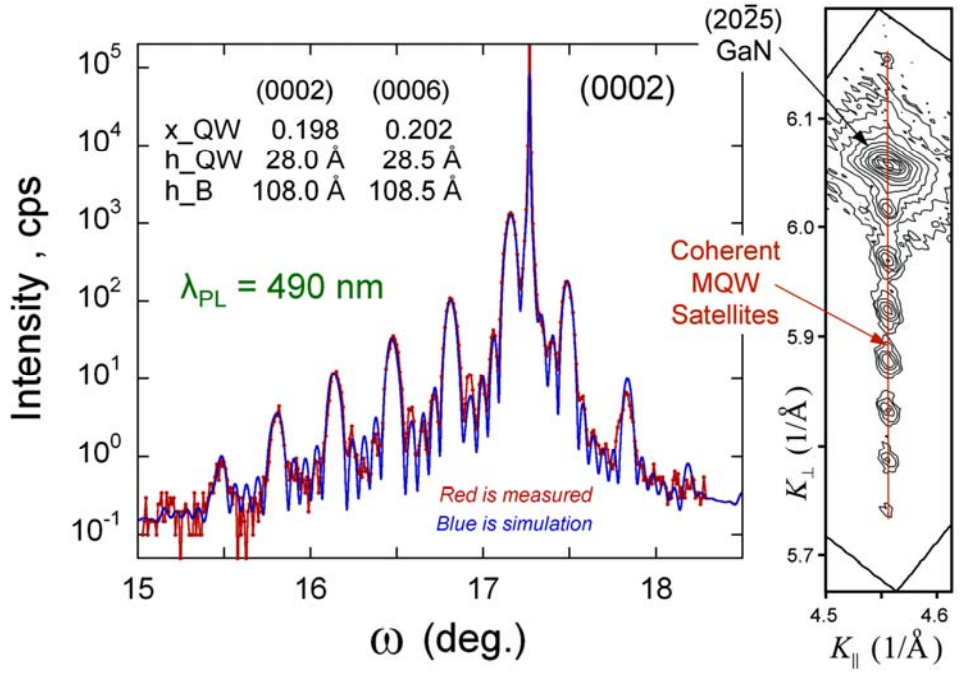


**Figure 1.** XRD analysis of a 5-period InGaN/GaN MQW grown on GaN/sapphire. Using dynamical x-ray diffraction theory, we simulated the (0002) rocking-curve data and found that the MQW consists of 28 Å thick $In_{0.20}Ga_{0.80}N$ wells and 108 Å thick GaN barriers; (0006) data confirm the (0002) results. The (20-25) reciprocal space map at the right demonstrates that the MQWs are coherently strained to the underlying GaN lattice, as assumed in the simulations.

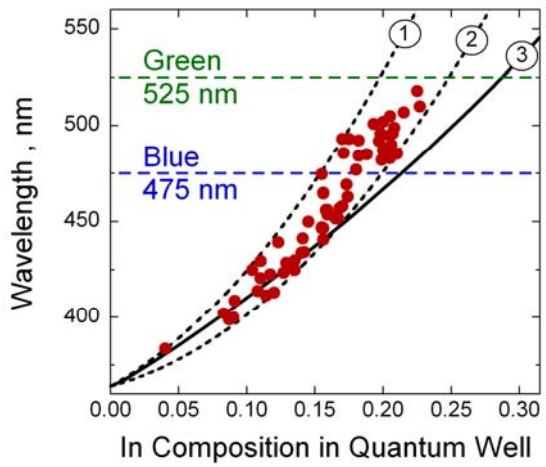


**Figure 2.** PL measurements of MQW-emission wavelength vs. MQW composition. Lines 1 and 2 bound the measurements; line 3 shows the emission wavelengths of bulk InGaN alloys. As In content rises, piezoelectric Stark shifts and compositional fluctuations also rise, which causes the MQW emission to redshift.

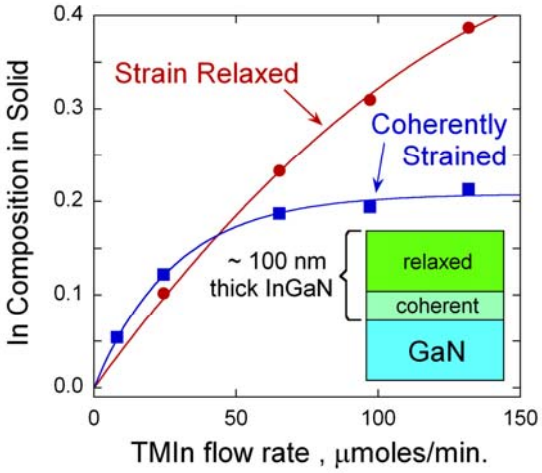


**Figure 3.** XRD measurements of the composition of 100 nm thick InGaN films grown on GaN at 760 °C. Initially coherent $In_xGa_{1-x}N$ films are limited to $x$=0.20 at high TMIn flow rates. Strain relaxation occurs as the film grows thicker, which yields a second layer with much greater In content at the same high flow rates.

# *Chemistry of AlGaN Particulate Formation*

*by* **M. E. Coltrin and J. R. Creighton**

**Motivation—**GaN and AlGaN alloys are extremely important materials with widespread applications for optoelectronics (e.g. solid state lighting) and high power electronics. The growth of AlGaN thin films by metalorganic chemical vapor phase deposition (MOCVD) is often complicated by parasitic gas-phase chemical reactions that diminish the deposition efficiency and make it difficult to control alloy composition. The growth rate and alloy composition depend sensitively on temperature and other reactor variables, making the process difficult to control and optimize. Our earlier work showed that gas-phase particulates form during AlGaN MOCVD, and are responsible for many of these growth complications.

**Accomplishment—**We have used a combination of experiments and reactor modeling to investigate parasitic chemical reactions that occur during AlGaN MOCVD. Growth rates for GaN, AlN, and AlGaN were measured over a wide range of reactor conditions. Our results indicate that the parasitic chemical reactions require high temperatures and occur in the boundary layer near the growing surface. These reactions ultimately lead to the formation of nanoparticles, which we have recently observed using *in situ* laser light scattering. Thermophoresis keeps the nanoparticles from reaching the surface, so the material tied up in nanoparticles cannot participate in the thin film deposition process. We have developed a relatively simple, 9-reaction mechanism in which activated (i.e., temperature-dependent) chemical reactions form reactive intermediate chemical species that go on to nucleate the gas-phase particles. Once the particles have been formed, we propose that the particles grow further by an MOCVD-type mechanism, which is similar to the mechanism for the (desired) thin-film growth. The chemistry model includes steps describing Ga-precursor decomposition, Al-adduct formation and methane elimination, particulate nucleation, and particle growth in the AlGaN system. Reacting flow simulations were used to predict film growth rates and were compared with our rotating-disk reactor experiments. As seen in Fig. 1, the measured AlGaN growth rate drops with increasing temperature (a signature of the activated parasitic chemistry) and with increasing Al-precursor flow rate. Our model calculates both trends quantitatively. The solid AlGaN composition as a function of growth temperature is shown in Fig. 2. The aluminum fraction of the alloy, $X_s(Al)$, increases with inlet gas mole fraction, $X_g(Al)$, but is always smaller in magnitude. As temperature is increased, and thus as the parasitic reaction pathways become more and more important, the ratio $X_s(Al) / X_g(Al)$ gets significantly smaller. Our model reproduces the general trends exhibited in Fig. 2, although not the strength of the curvature at the highest Al/III ratio.

**Significance**—The non-linear and non-ideal behavior of the AlGaN MOCVD has greatly impeded the growth and utilization of AlGaN material. Our investigations of the chemical mechanisms responsible for parasitic particle growth have led to a quantitative computer model of the growth process. This model will enable further reactor design modifications and process optimization to improve AlGaN growth and control of material quality.

**Sponsors for various phases of this work include:** DOE Office of Basic Energy Sciences

**Contact:** Michael E. Coltrin, Advanced Materials Sciences, Dept. 1126
Phone: (505) 844-7843, Fax: (505) 844-3211, E-mail: mecoltr@sandia.gov

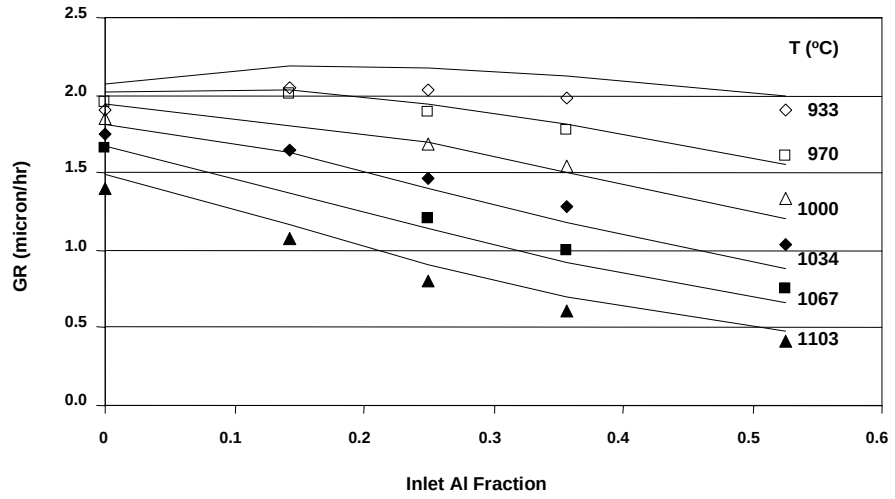


**Figure 1.** AlGaN growth rate as a function of growth temperature and Al/III (Al flow divided by total Group-III flow).

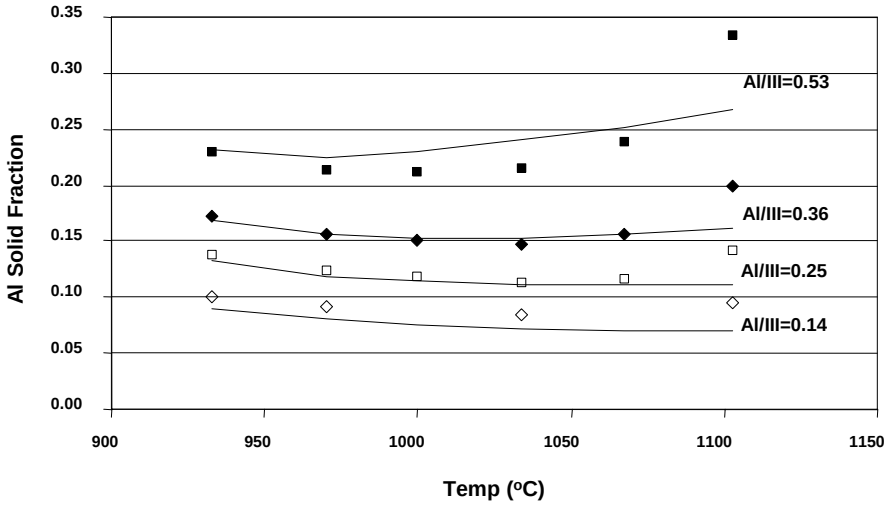


**Figure 2.** Al fraction in AlGaN alloy as a function of growth temperature and gas-phase Al fraction (Al flow divided by total Group-III flow).

# *Near-UV Pyrometry for Group-III Nitride MOCVD*

*by* **J. R. Creighton, D. D. Koleske, M. J. Russell and C. C. Mitchell**

**Motivation—**Temperature measurement during InGaN MOCVD is particularly difficult due to the transparency of the substrates (e.g., sapphire) and epilayers at the near-IR wavelengths (e.g. 900-1000 nm) normally used for pyrometry. In fact, with the exception of our technology, there is currently no readily available method that measures the true wafer surface temperature during deposition. The problem is particularly severe because the InGaN composition (and therefore emission wavelength) is extremely sensitive to temperature in the 700-800°C range. Due to errors in existing temperature measurement techniques, drifts of 10-20°C are common, leading to InGaN devices that emit outside the target wavelength window.

**Accomplishment—**This work extends our previous development of a near ultraviolet-violet emissivity-correcting pyrometer (NUV-ECP) that we installed and tested on our single-wafer research reactor, CVD1. We have now extended this method to our multiwafer Veeco D-125 MOCVD reactors, which required additional technology development, mostly requiring signal synchronization to the actual wafer position. The optics also required a redesign to optimize signal in a more constrained environment. The collection/injection optics installed on one of our D-125 reactors (DNZ) is shown in Fig. 1. This NUV pyrometry approach relies on the opacity of the GaN epilayer at wavelengths above the bandgap. Fortunately, the GaN bandgap red-shifts substantially with temperature: from ~350 nm at room temperature to ~ 430 nm at 1000°C. The shift in bandgap is essential for success. For example, at 800°C there is ~$10^{6\text{-}7}$ less signal at 400 nm compared to the typical pyrometer detection wavelength (~1000 nm). The very weak thermal emission signal near 400 nm requires a number of substantial modifications to the typical pyrometer design. The payoff has been the first true surface temperature measurements during GaN and InGaN MOCVD. All other techniques have directly or indirectly measured the temperature of the wafer holder, which is **never** equal to the actual wafer temperature. Measurement of the true surface temperature will result in better control of the desired InGaN composition, and therefore better control of the emission wavelength. This will result in higher yield of the epitaxial process, and lower cost of the final LED product. Two examples of the true surface temperature during InGaN multiquantum well growth are shown in Fig. 2. The 8°C temperature drift that occurred during the "bad" example will cause a quantum well emission wavelength shift of ~12 nm.

**Significance**—This research will impact the DOE SSL Mission/Goal, because precise temperature measurements in production-class multiwafer group-III MOCVD reactors will substantially increase the InGaN yield and lower the final LED cost. Lumileds Lighting is currently using a variation of this technology on a large number of their production MOCVD systems. We also expect this technology to significantly impact and accelerate InGaN epitaxy research earlier in the R&D cycle due to improved reproducibility of the GaN and InGaN epitaxial growth processes. A major cause of the irreproducibility is the lack of a true wafer temperature measurement method, which has now been addressed.

**Sponsors for various phases of this work include:** Laboratory Directed Research & Development, DOE National Energy Technology Laboratory, and DOE Office of Basic Energy Sciences

**Contact:** J. Randall Creighton, Advanced Materials Sciences, Dept. 1126
Phone: (505) 844-3955, Fax: (505) 844-3211, E-mail: jrcreig@sandia.gov

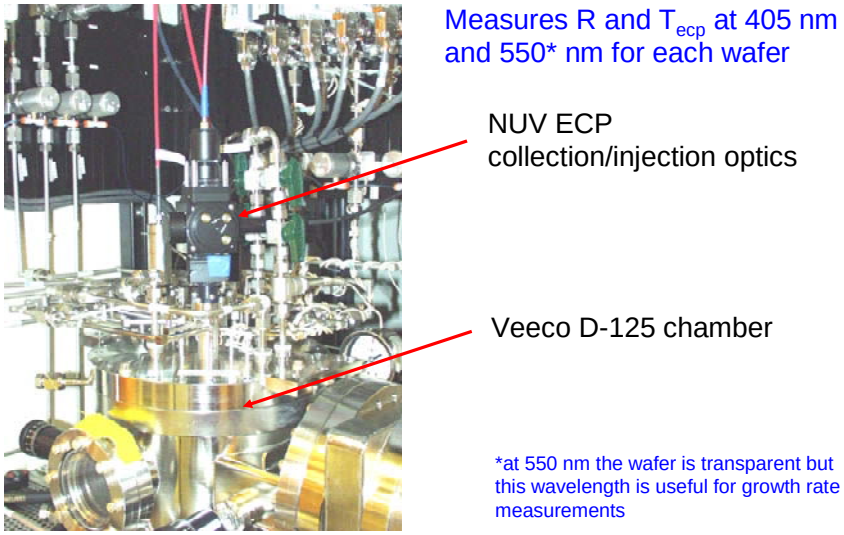


**Figure 1.** Photo showing installation of NUV-ECP collection/injection optics on a Veeco D-125 MOCVD system used to grown AlGaInN thin films.

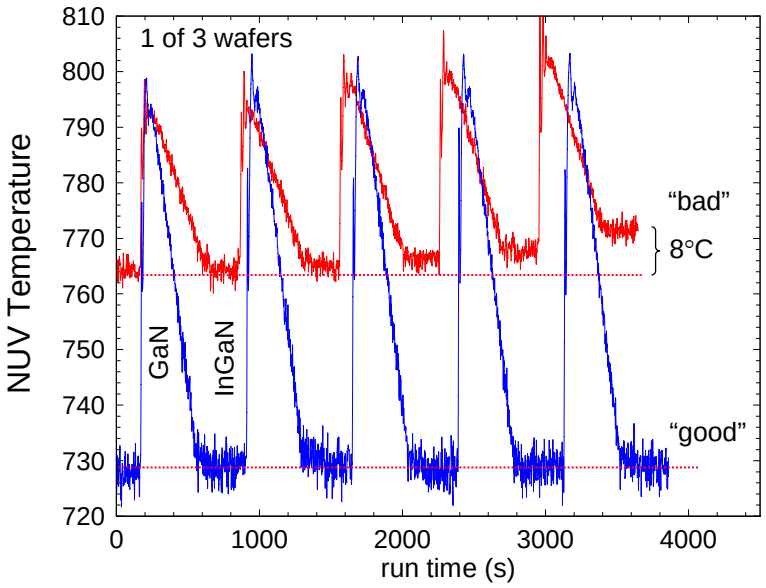


**Figure 2.** Two examples of the NUV-ECP temperature measured during InGaN multiquantum well deposition. In one case the temperature stayed constant during the InGaN step (good), while in the other example a substantial temperature drift occurred (bad). For reference, an 8°C drift will shift the quantum well emission wavelength by ~12 nm.

# Electromagnetic Radiation: Generation, Detection, & Spectroscopy

# *Modeling High Power Fiber Lasers and Amplifiers*

*by* **A. V. Smith, R. L. Farrow, and G. R. Hadley**

**Motivation—**Fiber lasers and amplifiers pumped by diode lasers can efficiently generate high quality beams with a continuous power of kilowatts or a pulse energy of millijoules. Fiber lasers are often more compact, more rugged, more efficient, and generate better beams than lasers based on a bulk gain medium. These attributes make fiber lasers promising coherent sources for a wide range of applications such as remote sensing of chemical and biological agents or for nonproliferation monitoring, for laser welding, for pumping nonlinear optical converters to shift the wave length to the mid infra red for countermeasure applications, and for direct optical initiation of explosives. However, many of these applications require that the laser operate near the upper limits of power or pulse energy, and achieving this requires careful balancing of a large number of design factors. Our research is centered on pulsed fiber lasers that produce nanosecond or picosecond pulses, a time range where the power is limited by self focusing and the fluence is limited by optical damage of the fiber core. Large cores have higher damage threshold energies but produce poorer quality beams. Long fibers have higher pulse energies and gains but encourage the parasitic processes of stimulated Raman scattering and amplified stimulated emission. Carefully balancing these factors is necessary in optimizing the fiber laser for each application, and this can be done efficiently only if we develop the appropriate fiber laser models.

**Accomplishment—**We are developing a suite of numerical models that individually address the most important power or energy limiting processes in fiber lasers. Our models include semi analytical (SA) and fully numerical finite difference time domain (FDTD) models that calculate transverse mode profiles and their radiative loss for both straight and bent fibers. Other completed modules numerically propagate beams with arbitrary transverse profiles to study the influence of the intensity-dependent refractive index ($n_2$) which is responsible for the self focusing that limits power transmission through a fiber and is also responsible for self phase modulation which alters the spectrum of a pulse as it propagates through the fiber. We are also developing a graphical user interface and integrating the models under it so they will be relatively easy to maintain and use.

**Significance**—The transverse mode computations are critical because bending the fibers is necessary to make the devices compact, and it is also used to discriminate against the high order transverse modes to maximize beam quality. The degree of discrimination depends on the tightness of the bend, the refractive index profile of the core and cladding, and the profile of the $Yb^{+3}$ gain ions in the core. Our models include all of the important factors that determine the beam quality. The critical power for self focusing for pure silica is approximately 4 MW. It is probably impossible to exceed this significantly by optimizing the fiber design, but we will test this using our models. Doping the core with $Yb^{+3}$ changes $n_2$ by unknown amounts and probably reduces the critical power. Quantitative comparisons with laboratory measurements are part of the modeling project, and we anticipate that these comparisons between model and measurement will lead to higher fiber energy and power limits.

**Sponsors for various phases of this work include:** Laboratory Directed Research & Development

**Contact:** Arlee V. Smith; Lasers, Optics, & Remote Sensing, Dept. 1128
Phone: (505) 844-5810, Fax: (505) 844-5459, E-mail: arlsmit@sandia.gov

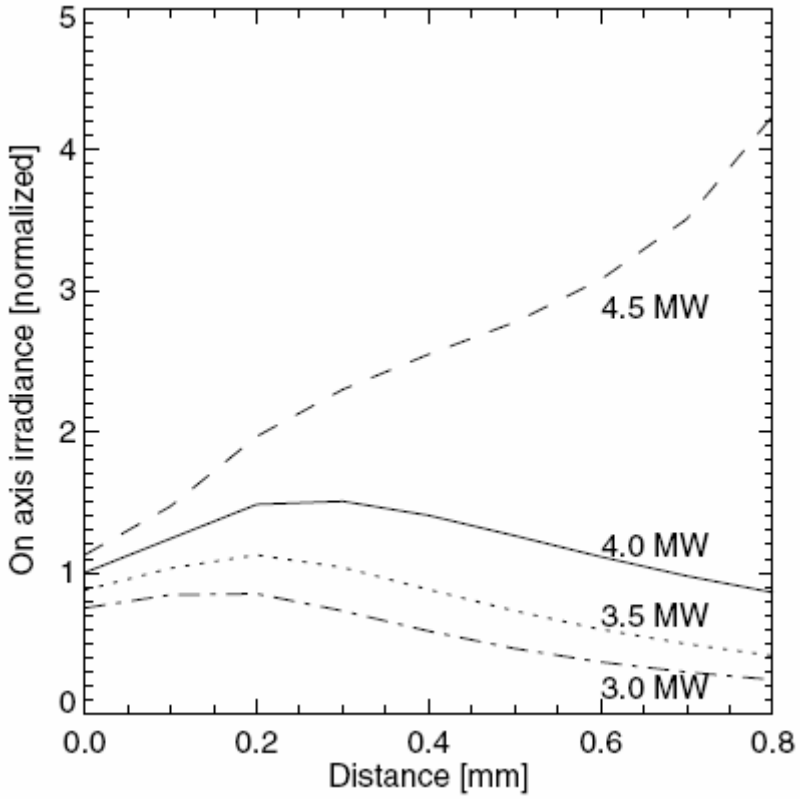


**Figure 1.** On-axis irradiance versus propagation distance for different powers launched into a fiber with $n_2=2.7x10^{-20}$ W/m$^2$. The self focusing power for this value of $n_2$ is 4.3 MW.

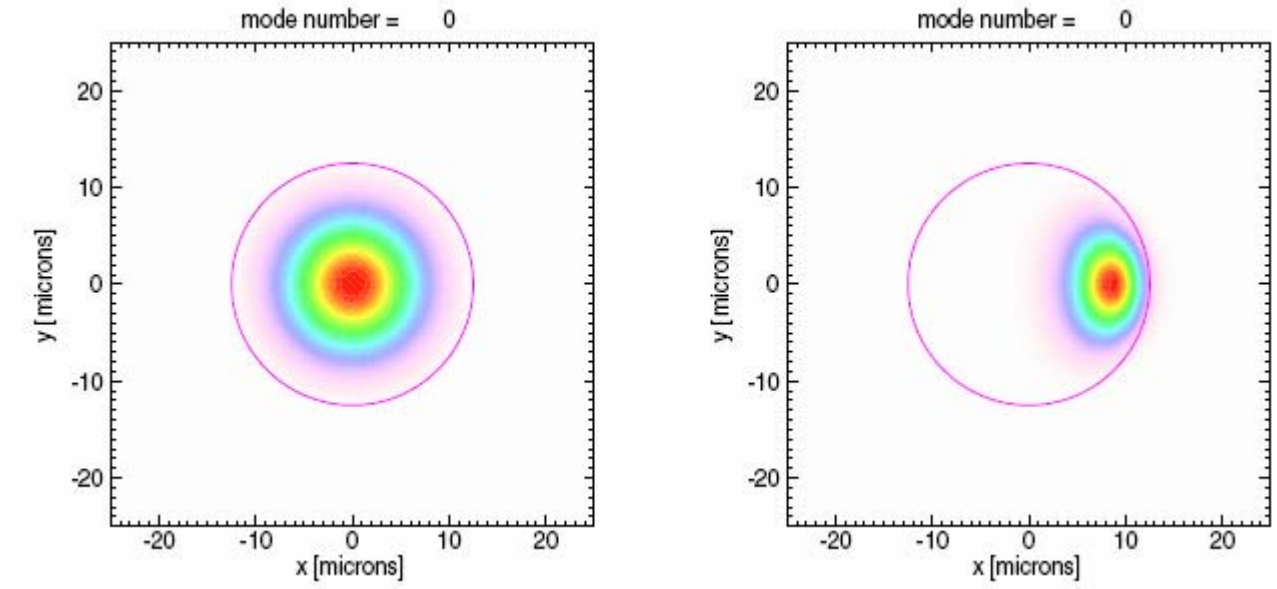


**Figure 2.** Transverse mode profiles for a straight fiber (left) and for same fiber when it is tightly bent (right).

# *High Efficiency UV Generation*

*by* **D. J. Armstrong and A. V. Smith**

**Motivation**—Tunable, high-pulse-energy UV light is required for a wide range of remote sensing missions, including standoff detection of airborne chem-bio agents, verification of nuclear and WMD nonproliferation, and for measuring concentrations of atmospheric gases such as stratospheric ozone. UV sources used for remote sensing can be deployed in ground-, air-, or satellite-based platforms, with the latter two requiring efficient, durable, and robust systems capable of operating under widely varying environmental conditions. Essentially all UV generation systems use nonlinear-optical (NLO) frequency conversion, where fixed laser wavelengths such as the harmonics of Nd:YAG are shifted in frequency to UV wavelengths of interest. However, conventional NLO technology rarely meets the specifications for efficiency, durability, and robustness required for remote sensing. Recent advancements in NLO technology developed in Dept. 1128 address these shortcomings.

**Accomplishment**—Using the Sandia-patented RISTRA optical parametric oscillator (OPO) shown in Fig. 1, we have developed a Nd:YAG-laser pumped UV generation system that is efficient, robust, and resistant to optical damage. The image-rotating RISTRA is ideal for high-energy UV generation because of its excellent beam quality. It's also ideal for remote sensing applications because its quasi-monolithic design is stable and mechanically robust, and, owing to its non-planar geometry, it requires no cavity mirror adjustments.

Our UV generation system uses sum-frequency generation (SFG) to mix a cavity-resonant 803 nm signal wave with the 532 nm pump wave (Nd:YAG second harmonic) to generate 320 nm light. Its design results from a comprehensive approach based on extensive numerical modeling and thorough laboratory testing. Its key features include image rotation, which works in conjunction with crystal birefringence to produce excellent beam quality; pulsed injection seeding, which reduces cavity build-up time so the pump and signal temporal profiles match in time; the use of beams with flat-top spatial profiles for optimum mixing efficiency; large beam diameters for low fluence and reduced risk of optical damage; and intra-cavity SFG, which takes advantage of the resonantly-enhanced intra-cavity signal fluence to increase SFG efficiency.

Our results are shown by the efficiency curves in Fig. 2(a), where the maximum optical-to-optical efficiency (1064 nm to 320 m) is 24%, and the maximum UV energy is 140 mJ. Figure 2(b) compares the energy of the UV output pulse under various operating conditions to illustrate the gains in efficiency achieved by our design.

**Significance**—High-efficiency, high-energy UV generation using stable, mechanically robust RISTRA OPO's opens the door to a variety of remote sensing applications. When combined with diode-pumped solid-state pump lasers, RISTRA-based UV generators can achieve high overall system efficiency in small packages that are suitable for deployment in the harsh environments of airborne- or satellite-based platforms.

**Sponsors for various phases of this work include:** Work for Others/National Aeronautics & Space Administration (NASA) Langley Research Center (LaRC) and Nuclear Weapons

**Contact:** Darrell J. Armstrong; Lasers, Optics, & Remote Sensing, Dept. 1128,
Phone: (505) 844-4757, Fax: (505) 844-5459, E-mail: darmstr@sandia.gov

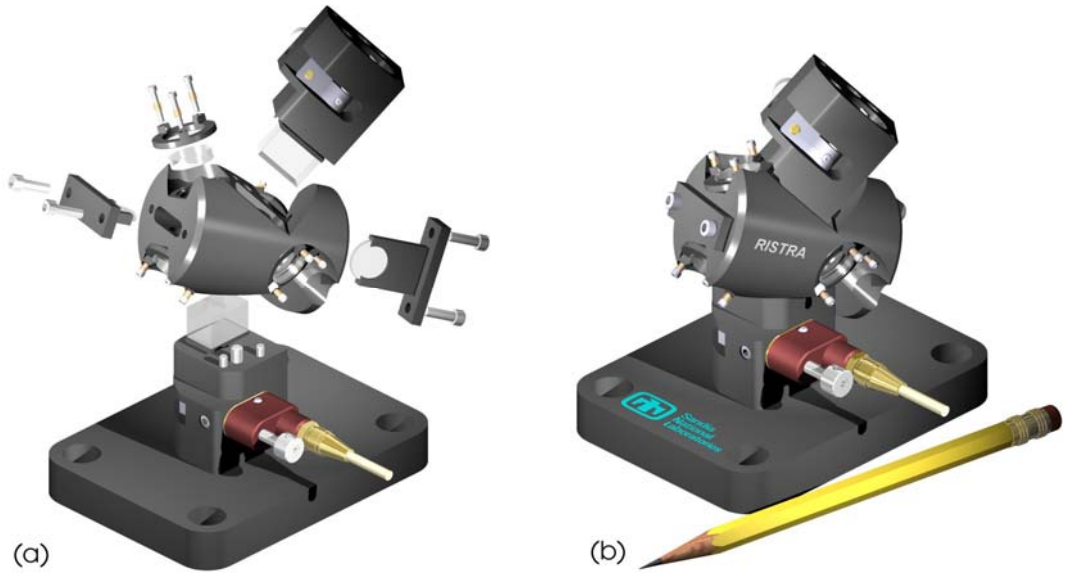


**Figure 1.** (a) Exploded view of a two-crystal RISTRA OPO, denoting rotated image singly-resonant twisted rectangle. Cavity mirrors require no tilt adjustments and are held against machined faces on the cylinder by spring-loaded retainer rings. λ/2 plates insert into each end of the cylinder to control intra-cavity polarization. For UV generation, the OPO is pumped by 532 nm light from an injection-seeded Nd:YAG laser, with a potassium-titanyl-arsenate crystal in the upper leg generating an 803 nm signal and 1576 nm idler. A β-barium-borate SFG crystal in the lower leg mixes the cavity-resonant 803 nm signal with the 532 nm pump to generate 320 nm light. The OPO is pulse-injection-seeded for high efficiency, and the pump and pulsed-seed beams have flat-top spatial profiles. (b) Assembled two-crystal RISTRA OPO. The length of the cylindrical body is 1.97 in.

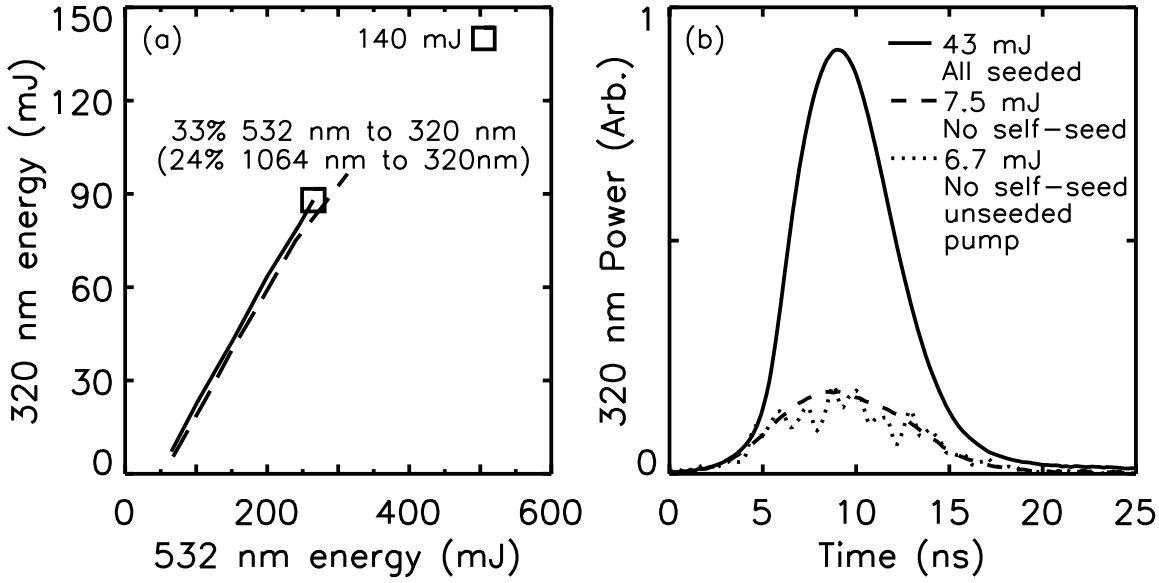


**Figure 2.** (a) UV energy versus pump energy for the intra-cavity SFG RISTRA OPO. (b) UV pulses and their energies under various operating conditions, including pulse injection-seeded oscillation, unseeded oscillation, and unseeded oscillation using a broadband pump pulse.

# *Photonic Lattice vs. Blackbody Radiation*

*by* **W. W. Chow**

**Motivation—**Modification of spontaneous emission is one of the many novel optical phenomena exhibited by photonic lattices. A photonic lattice can funnel radiation into narrow energy bands, where exceedingly high intensities at photonic lattice band edges have been predicted theoretically and observed experimentally. A question is whether the peak intensities exceed those of a blackbody under similar experimental conditions. The answer is important for scientific understanding and impacts the development of new light sources.

**Accomplishment—**We have calculated the emission from a radiating source embedded in a photonic lattice. The analysis considers the photonic lattice and free space as a combined system. Furthermore, the radiating source and electromagnetic field are quantized. We found that the photonic lattice spectrum deviates from the Planck distribution, with intracavity emission suppressed at certain frequencies and enhanced at others (Fig. 1). In the presence of rapid population relaxation, where the photonic lattice and blackbody populations are described by the same equilibrium distribution, the enhancement does not result in output intensity exceeding that of the blackbody at the same frequency (Fig. 2).

Looking ahead towards applications such as photonic lattice lasers, we have extended the investigation to study nonequilibrium situations. There, the photonic lattice population has a greater tendency to deviate from thermal equilibrium because the collisions are unable to replenish the population depleted by the strong intracavity field at the photonic bandedges. Then, output intensities exceed those of the blackbody, even when both structures are identically pumped.

**Significance—**There is much debate concerning the output intensity of an active photonic lattice compared to that of a blackbody. The answer has scientific and engineering importance. Arriving at an answer is difficult experimentally because of the difficulty in ensuring that the comparison is made under similar conditions. Theoretically, the challenge lies with the long-standing quantum-optics problem of electromagnetic field quantization for an open system. We have unambiguously answered the question.

**Sponsors for various phases of this work include:** Laboratory Directed Research & Development

**Contact:** Weng W. Chow, Advanced Materials Sciences, Dept. 1123
Phone: (505) 844-9088, Fax: (505) 844-3211, E-mail: wwchow@sandia.gov

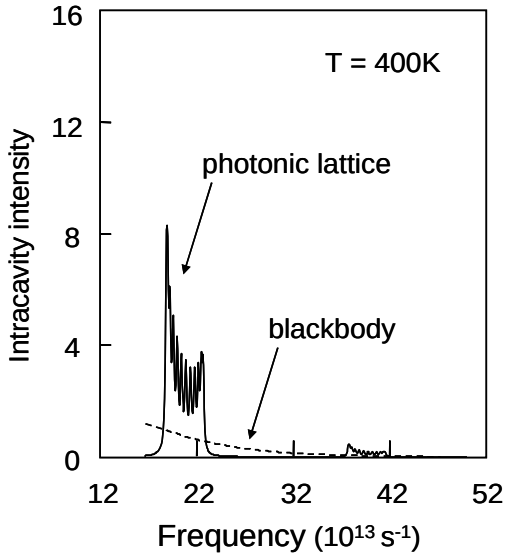


**Figure 1.** Photonic-lattice (solid curve) and blackbody (dashed curve) intracavity emission spectra, showing enhancement of intracavity intensity with a photonic lattice.

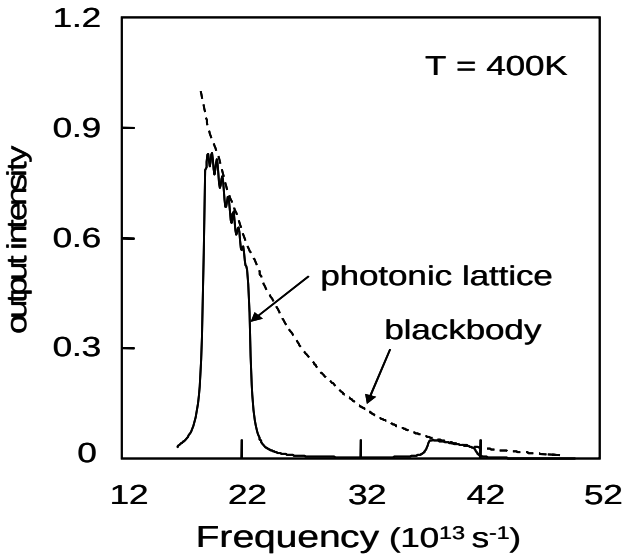


**Figure 2.** Photonic-lattice (solid curve) and blackbody (dashed curve) output emission spectra, showing that the intracavity intensity enhancement does not result in higher peak output intensities from an active photonic lattice compare to those from an equivalent blackbody.

# *Voltage Tunable Two-color Superlattice Infrared Photodetectors*

*by* **J. L. Reno**

**Motivation**—Voltage tunable two-color infrared detectors have many important applications such as remote temperature sensing and chemical analysis. It is particularly useful to have two-color detectors that respond in the 3−5 μm midwavelength infrared (MWIR) and the 8−12 μm long-wavelength infrared (LWIR) ranges, which are atmospheric transmission windows. Quantum well infrared photodetectors (QWIPs) with voltage tunable peaks are attractive for two-color detection because these two-terminal devices, when integrated with time-multiplexed readout circuits, greatly simplify the production of high-uniformity focal plane arrays (FPAs).

**Accomplishment**—We have demonstrated voltage tunable two-color superlattice (SL) detectors, where the peak wavelength switches from the LWIR to the MWIR range upon reversing the polarity of applied bias. The active region of these superlattice infrared photodetectors (SLIPs) consists of multiple periods of two short-period SLs designed for MWIR and LWIR detection. These SLIPs rely on two types of blocking layers to achieve voltage tunable operation: a thick undoped barrier for low-energy dark electrons and a thick doped layer for high-energy photoelectrons. The first detector, which consists of AlGaAs/GaAs SLs for both LWIR and MWIR detection, demonstrates wavelength switching from 9.5 μm under large positive bias to 6 μm under negative bias and has a background-limited temperature of 55 K for 9.5 μm detection and 80 K for 6 μm detection. The second detector (results shown in the figures), which contains AlGaAs/GaAs SLs for LWIR detection and strained InGaAs/GaAs/AlGaAs SLs for MWIR detection, exhibits wavelength switching from the 8−12 μm band under positive bias to the 3−5 μm band under negative bias. The background-limited temperature of this detector is 70 K for LWIR detection and 110 K for MWIR detection. This SLIP is the first ever voltage tunable MWIR/LWIR detector with performance comparable to those of optimized one-color QWIPs. We have also demonstrated that corrugated-QWIPs are capable of coupling normally incident light for two-color application.

**Significance**—Using different SL pairs, one can obtain different two-color combinations with bandwidths tailored to suit specific applications, which indicates the usefulness of our design for large-format FPAs.

**Sponsors for various phases of this work include:** Nuclear Weapons/Science & Technology

**Contact:** John L. Reno, Semiconductor Material & Device Sciences, Dept. 1123
Phone: (505) 844-9677, Fax: (505) 844-3211, E-mail: jlreno@sandia.gov

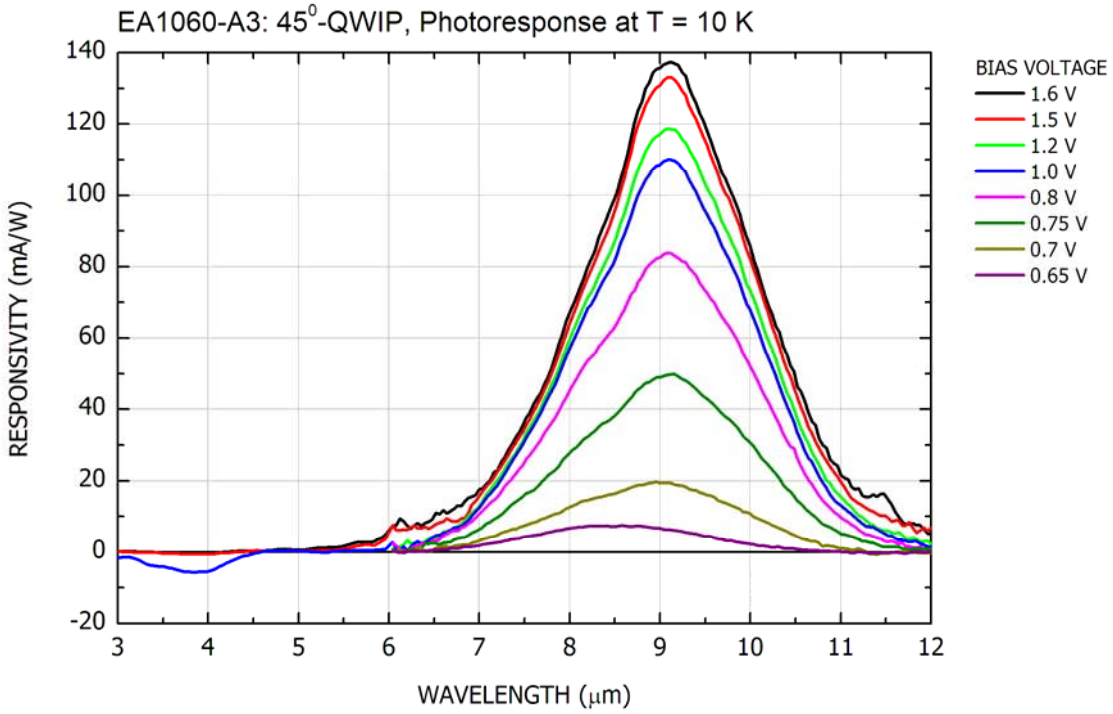


**Figure 1.** Responsivity in the LWIR under positive bias voltage.

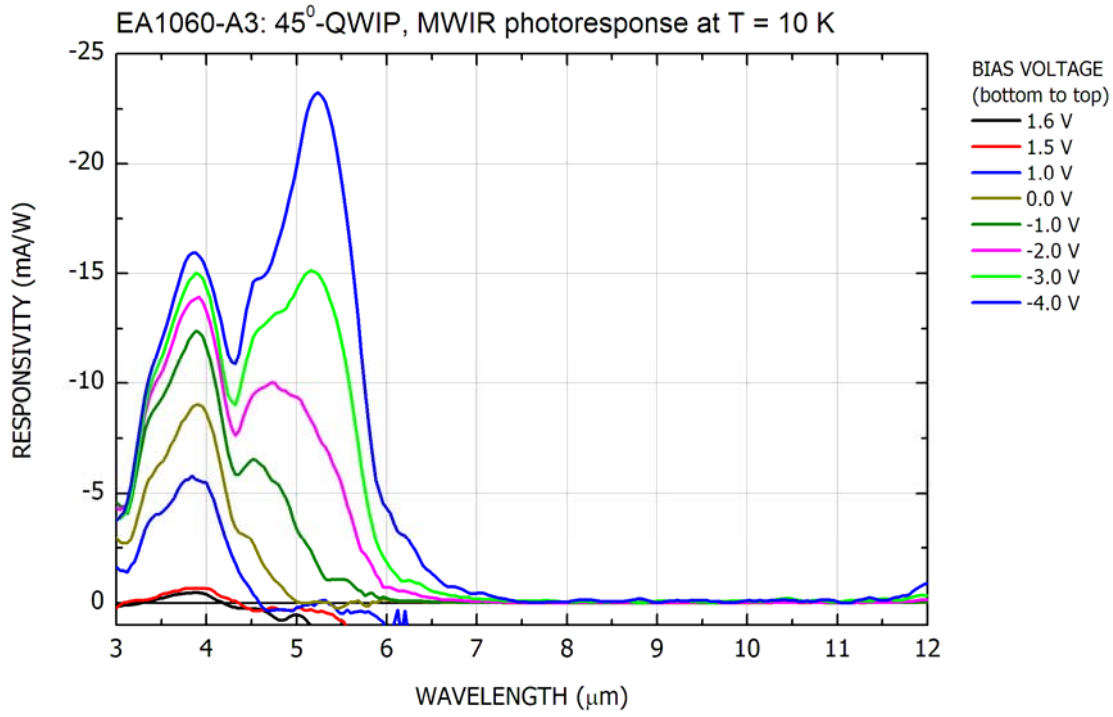


**Figure 2.** Responsivity in the MWIR under negative bias voltage.

# *Quantum Dot Infrared Photodetectors (QDIPS)*

*by* **J. G. Cederberg**

**Motivation**—Quantum Dot Infrared Photodetectors (QDIPs) utilizing electronic transitions of self-assembled quantum dots (SAQD) are candidates for infrared detection from 3 to 30 μm (40-400 meV). Electrons in the populated conduction band of the SAQD are photoexcited to a higher energy state (Fig. 1). Potential advantages of QDIPs over existing detectors lies in the zero-dimensional characteristics of SAQD: sensitivity to normal incidence radiation, increased responsivity due to increased excited carrier lifetime, and higher temperature operation due to reduced overlap of the SAQD density of states with the Fermi distribution. Under the influence of an electric field the photoexcited carriers are detected as a photocurrent (Fig. 1). The three-dimensional confinement of the SAQD modifies the symmetry selection rules allowing the SAQD to couple to normal incidence radiation. The increased carrier lifetime in SAQD (tens of nanoseconds compared with tens of picoseconds for quantum wells) is attributed to reduced carrier-phonon coupling, termed the "phonon bottleneck". Higher operating temperature should result from the reduced overlap of the SAQD density of states with the carrier Fermi function.

**Accomplishment**—In collaboration with Prof. Sanjay Krishna, with the University of New Mexico's Center for High Technology Materials, an InAs SAQD QDIP has been demonstrated. The device shows tunable photocurrent response between 7.7 and 9.9 μm with response persisting up to 90 K. (Fig. 2) The device incorporates strain balancing techniques to minimize strain in the layers that result in performance degrading defects in the material. InAs SAQD are buried by compressively strained $In_{0.15}Ga_{0.85}As$ forming a dots-in-a-well (DWELL) structure. The compressive strain is balanced by tensile $GaAs_{0..8}P_{0.2}$. This demonstration provides a path to increasing the detectivity of QDIPs by increasing the number of SAQD layers in the structure. Almost all the devices investigated to date have utilized a small number of repeat periods (typically 10 or less) to limit the introduction of dislocations into the active region. This represents a path to higher performing mid-wavelength and long wavelength IR sensors.

**Significance**—Infrared sensing has long been a distinguishing technology for military and intelligence communities. QDIP sensors can positively impact this technology by providing detectors with higher operating temperatures or with functionality that is not presently achievable. Since QDIPs are fabricated in III-V materials, they have the potential to be monolithically integrated with other optical and electronic components for engineering sensing systems. These systems also have applications in chemical identification for environmental monitoring and process control. This demonstration highlights the unique applications for SAQD in optoelectronics.

**Sponsors for various phases of this work include**: Laboratory Directed Research & Development

**Contact:** Jeffrey G. Cederberg, Advanced Materials Sciences, Dept. 1126
Phone: (505) 284-5456, Fax: (505) 844-3211, E-mail: jgceder@sandia.gov

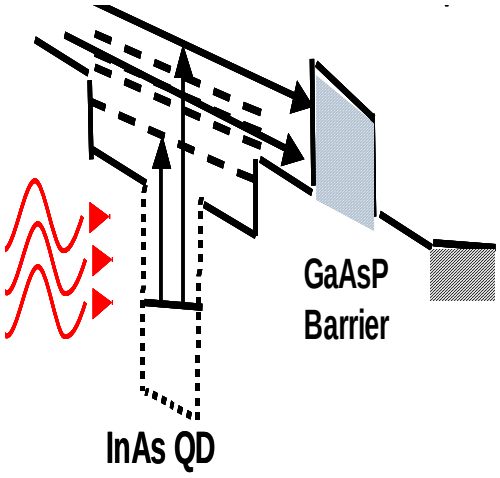


**Figure 1.** A single period of the conduction band diagram for a strain balanced QDIP device.

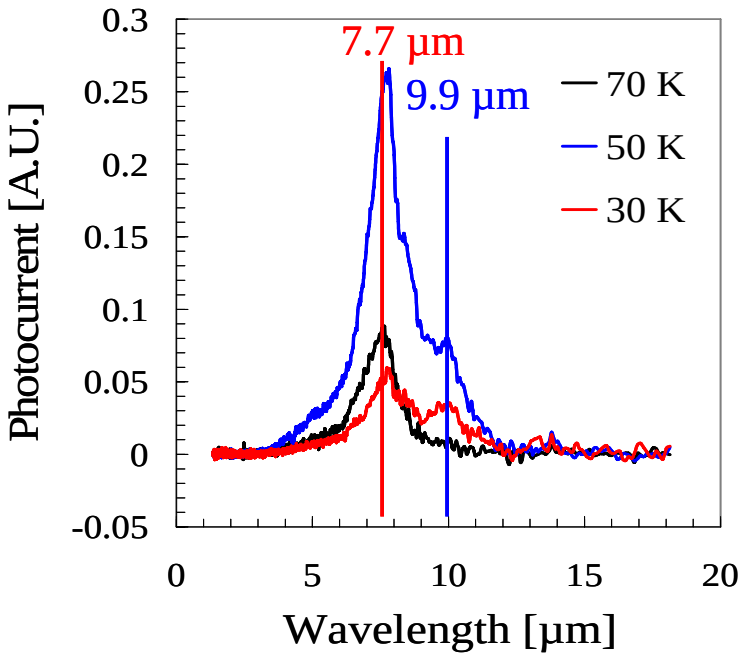


**Figure 2.** Photocurrent response from an InAs SAQD strain balanced QDIP.

# *Single Quantum Well Terahertz Plasmon Detectors*

*by* **E. A. Shaner, M. Lee, M. C. Wanke, A. Grine, and J. L. Reno**

**Motivation**—The terahertz portion of the electromagnetic spectrum, *i.e.*, frequencies roughly around $10^{12}$ Hz, lies in a technological gap between conventional electronics, which function at lower frequencies, and conventional photonics, which work at higher frequencies. This gap is a consequence of fundamental considerations regarding electron transit times and band gaps in metals and semiconductors. Despite this, there is a great deal of interest in THz generation and detection as it possibly enables, among other things, a variety of defense- and security-related applications ranging from covert inspection for concealed weapons to the stand-off detection of chemical hazards and energetic materials. To get around basic electronic limitations on the frequency range of THz detectors, we have been exploring the use of low-dimensional plasmon charge excitations driven by THz radiation.

**Accomplishment**—The basic detector is a depletion mode field-effect transistor (FET) structure fabricated from high mobility modulation-doped single- or double-quantum well GaAs-AlGaAs heterostructures (Fig. 1). As shown, the device consists of source and drain electrical contacts along with a grating gate to couple in THz radiation. Plasmons are collective charge density oscillations that resonate at frequencies orders of magnitude higher than can be reached by conventional electronics. The resonant frequency of a plasmon is set by the carrier density in the quantum well. The function of the gate in the structure shown is therefore to tune the electron density in the device and thus adjust the resonant plasmon frequency to match the THz radiation illuminating the device. Initial investigations of grating-gate detectors were performed using double-quantum wells. In that work, the basic principles of detection using plasmons were uncovered. It was found that the grating-gate detector exhibited a photoresponse when the plasmon frequency under the grating gate was tuned to the frequency of the incident illumination. This electrically tunable 'spectrometer on a chip' capability is not found in other THz detectors (or in more conventional detectors used in the visible regime, for that matter).

Recent work on grating-gate detectors has shown that the same electrically tunable photoresponse arises in detectors made from single-well material (Fig. 2). Several new detector geometries were investigated, including sub-wavelength detectors and a 'split grating-gate' detector. The 'split grating-gate' detector utilizes an intentionally built-in nonlinearity that increases detector responsivity by several orders of magnitude while still retaining tunability.

**Significance**—In double layer devices, one needs to be concerned with mechanisms, such as interlayer tunneling, that are not easily understood when combined with plasmon excitations. The realization of single-well grating-gate detectors immediately simplifies both device fabrication and modeling by removing the second well.

From a practical standpoint, single well devices are more like conventional FETs that are widely used in electronics. Thus, integration of other useful components, such as on-chip signal amplifiers, becomes possible.

**Sponsors for various phases of this work include:** Laboratory Directed Research & Development

**Contact:** Eric A. Shaner, Semiconductor Material & Device Sciences, Dept. 1123
Phone: (505) 284-5636, Fax: (505) 8443211, E-mail: eashane@sandia.gov

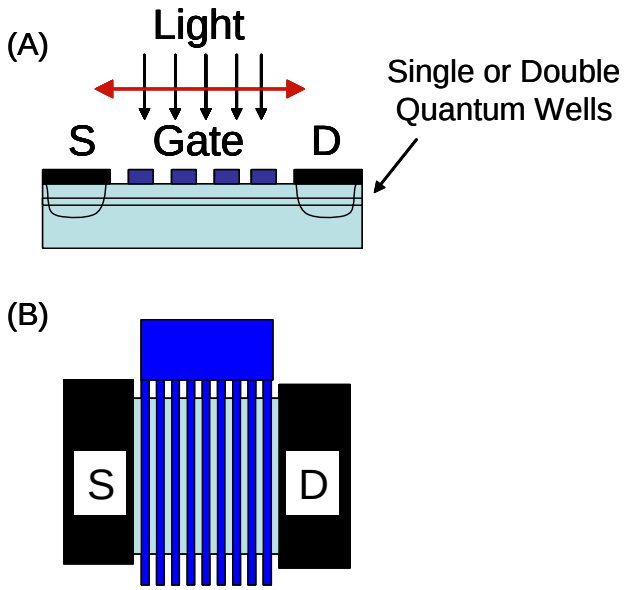


**Figure 1.** Basic geometry of the grating-gated plasmon THz detector. Device cross-section and illumination conditions are shown in (A). The detector operates at normal incidence with the electric field polarized across the grating. Part (B) shows the top down view of the detector. Gratings used range from 2mm x 2mm down to 0.2 mm x 0.2 mm in area and have a 4 μm period with a 50% duty cycle *(i.e.* 2 μm gold + 2 μm gap).

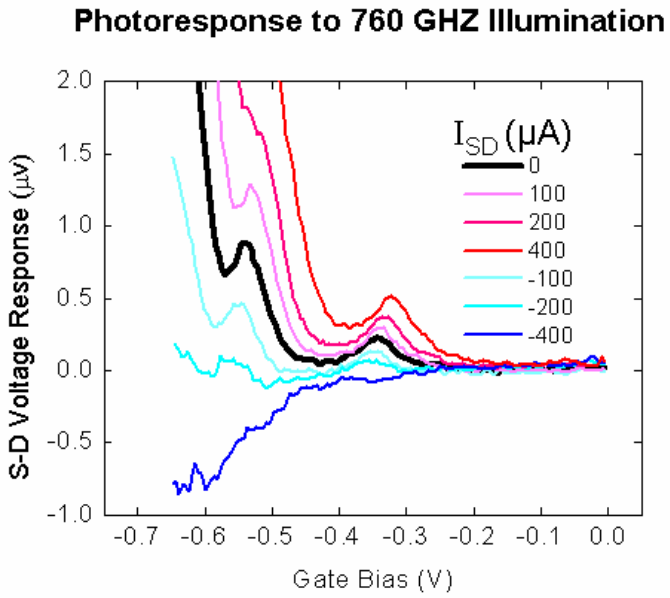


**Figure 2.** Typical photoresponse of a single-well plasmon detector to 0.76 THz. The black trace shows a photovoltaic response (zero source-drain current). Resonant peaks are observed at -0.35V and -0.55V gate bias. Positive currents add a positive photoconductive response component, and negative currents add a negative photoresponse that competes with the photovoltaic signal.

# *Gas-phase Absorption Spectrum of 2, 4 DNT Using THz Time-domain Spectroscopy*

*by* **R. J. Foltynowicz**

**Motivation—**Terahertz (THz) spectroscopy is emerging as a powerful technique to identify and characterize molecular species. Due to recent advances in femtosecond lasers and optical materials, the THz radiation band from 0.1 to 10 THz is now routinely accessible. Spectroscopically, this is a new and unexplored portion of the spectrum that is rich in unique molecular information. In addition, the propagation properties of THz radiation through the atmosphere are potentially attractive for remote explosives sensing applications.

From our previous studies on the propagation of THz radiation through the atmosphere, we learned that the atmosphere is not as opaque as we thought. There are many THz transmission windows within the atmosphere. However, to capitalize on the THz transmission properties of the atmosphere for explosive vapor sensing, it is important to determine if spectra exist for these molecules in these windows. Therefore, our research interests lie in characterizing gas-phase explosive materials to guide the development of novel THz devices for remote explosives sensing applications.

**Accomplishment—**Recently, we have measured the first known gas-phase absorption spectrum of the explosive 2, 4 dinitrotoluene (DNT) from 0.4 to 2.7 THz using THz time-domain spectroscopy. Figure 1 shows the characteristic signature of 2, 4 DNT. The absorption lines in the 2, 4 DNT spectrum are rotational states of the molecule. The high density of lines can be attributed to the large moments of inertia of DNT which lead to a reduction in the frequency spacings between transitions.

The experimental setup used to make this measurement is shown in Fig. 2. The THz generation is performed by optical rectification of an 800 nm femtosecond laser pulse in a <110> ZnTe crystal. This process generates a broadband THz pulse with a ~1ps period. The THz beam is detected via electro-optic sampling, which exploits induced polarization changes of the probe beam due to the THz interaction within a ZnTe crystal sensor. The polarization changes are proportional to the strength of the THz electric field and hence we measure the electric field strength of the THz radiation as a function of delay time. Currently, the detector bandwidth is 0.40 to 2.7 THz with an instrument spectral resolution of 1 GHz (0.03 $cm^{-1}$).

The explosive material used was initially a solid that was heated to 150$^{o}$ C in a vacuum cell. At this temperature, most of the explosive material is converted into the gas phase. The equilibrium, static pressure for the experiment was 253 mTorr and the spectral resolution of our measurement was 8 GHz.

**Significance**—From our previous measurements of atmospheric water, we established a map of the background absorptions from the atmosphere as well as transmission windows. Having this information allowed us to concentrate our molecular identification in these transmission windows. We measured the spectral signature of 2, 4 DNT and found resonances in the transmission windows of the atmosphere. In addition, these lines are unique compared to the water transitions. These data will guide the development of THz sensors and detectors to develop a system that can detect explosive vapors remotely.

**Sponsors for various phases of this work include:** Nuclear Weapons/Science & Technology, Laboratory Directed Research & Development, and Work for Others/Transportation Security Adminsitration

Contact: Robert J. Foltynowicz; Lasers, Optics, & Plasma Sciences; Dept. 1128
Phone: (505) 844-8148, Fax: (505) 844-5459, E-mail: rjfolty@sandia.gov

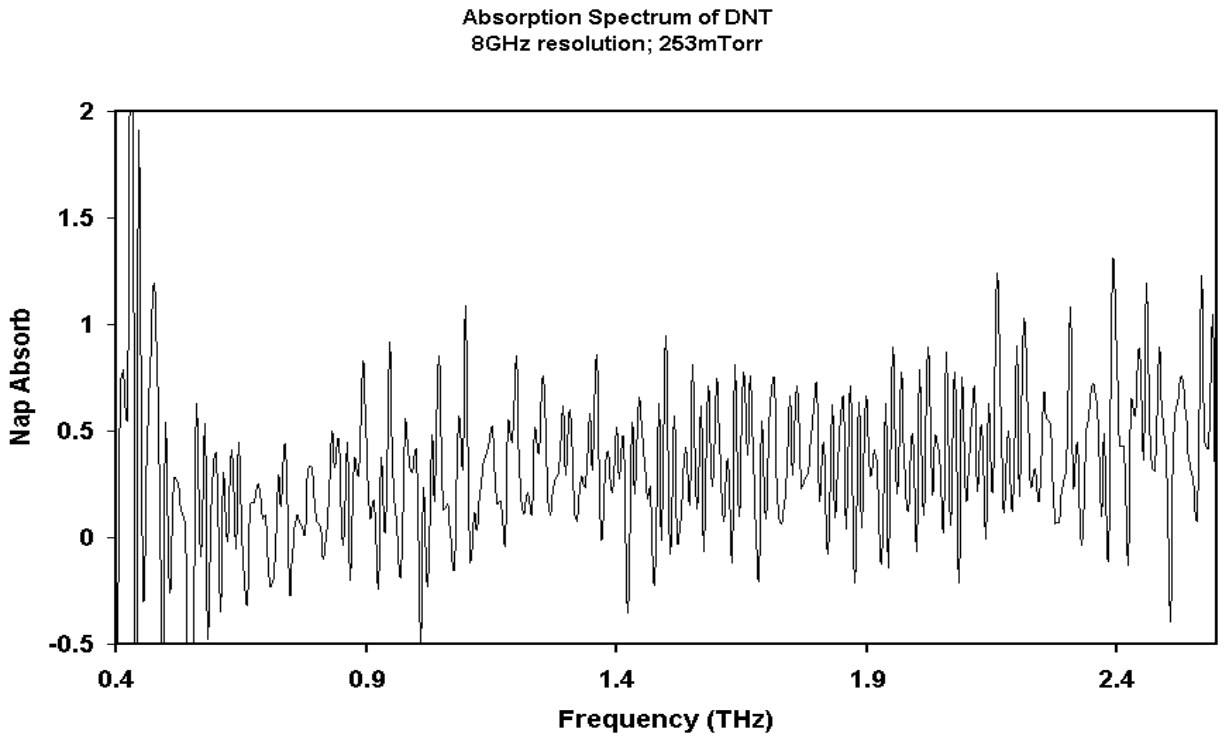


**Figure 1**. Absorption spectrum of gas-phase 2, 4 DNT from 0.4 to 2.7 THz.

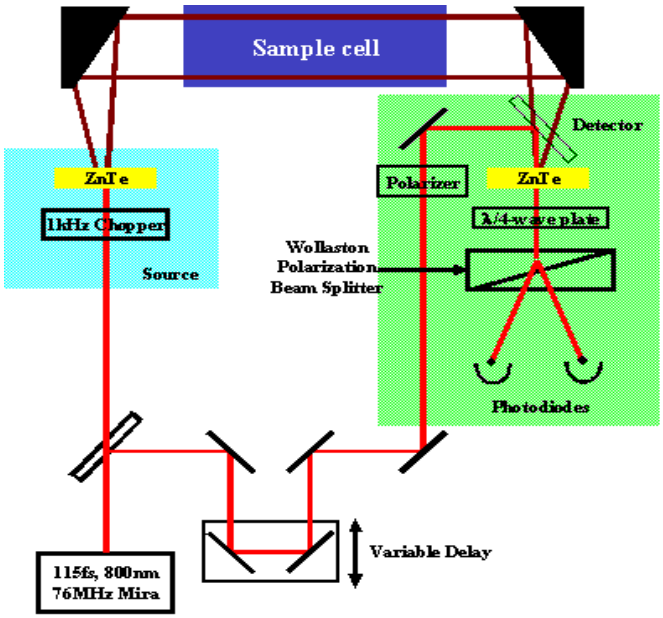


**Figure 2**. Diagram of the THz time-domain spectrometer. Femtosecond laser pulses chopped at 1KHz pump a <110> ZnTe crystal to produce THz radiation. The THz beam travels through the sample cell and collinearly propagates with an 800nm probe beam with horizontal polarization through a ZnTe sensor. The THz electric field strength is detected via polarization changes induced in the probe beam by the THz beam inducing a change in the birefringence of the ZnTe sensor.

# Materials in Extreme Environments: Radiation, Plasma, & Shock

# *Ion Photon Emission Microscope for Radiation Effects Microscopy*

*by* **B. L. Doyle, Michael Mellon (Quantar Technology, Inc.), Floyd Del McDaniel (University of North Texas), and Paolo Rossi (University of Padua, Italy)**

**Motivation—**Semiconductor and micro-electronic circuits and devices used in space and weapons are subjected to bombardment by high-energy cosmic ray ions. These interactions frequently result in reliability problems and unpredictable behavior.

Historically, laboratory-based, ion-induced radiation effects studies on semiconductors and devices have been performed using spatially-broad beams flooding the sample, generated from a high-energy, lab-based particle accelerator. Single-Event-Upset (SEU) cross-sections are then measured as a function of the ionizing power of the beam. While these approaches have been extremely valuable and productive for overall device characterization, they frequently do not enable the spatial pinpointing of the specific devices within a circuit involved in radiation sensitivity problems.

The goal of this research was to develop a new approach that could use the broad ion beams from an accelerator or radioactive source to pinpoint where Single Event Effects occur on a chip.

**Accomplishment—**With the Ion Photon Emission Microscope, or IPEM, spatially-resolved information is obtained from use of a single-event-counting, position-sensitive detection system. This detector determines the X-Y position of a single ion strike occurring among many in the broad incident ion beam, using an auxiliary photon-generating thin fluorescent film (ion-to-photon converter) located in the plane of the sample, a standard optical microscope and a Mepsicron™ single photon position sensitive detector. Figure 1 shows a schematic of the IPEM.

When this ion-strike spatial location is time-correlated with a specific observed SEU or charge collection problem event in the device under test, a detailed and quantitative map of radiation sensitivity is produced, which is of much greater interpretive and diagnostic value than are the traditional broad beam tests. Figure 2 shows an example of the IPEM imaging charge collection in an operational amplifier being studied for Single Even Gate Rupture with Lockheed Martin. An extended sample area can be analyzed and mapped without any point to point scanning, leading to potentially more rapid and comprehensive measurements. Also, since photons are being imaged, the analysis of the part or circuit can take place in air, ameliorating the need to put the samples into a vacuum chamber. Such in-air analyses are becoming common for Single Event Effects testing at large cyclotron facilities such as that at Texas A&M and Michigan State Universities.

**Significance**—The IPEM team won an R&D-100 Award in 2005 for this invention, and the unit is being marketed by Quantar Technology, Inc., as the 2600-IPEM Analyzer. We plan to develop an IPEM to operate at the Texas A&M Cyclotron lab for ultra high energy - heavy ion radiation effects microscopy in the near future.

**Sponsors for various phases of this work include:** Nuclear Weapons/Readiness in Technical Base & Facilities

**Contact:** Barney L. Doyle, Radiation Solid Processing, Dept. 1111
Phone: (505) 844-7567, Fax: (505) 844-7775, E-mail: bldoyle@sandia.gov

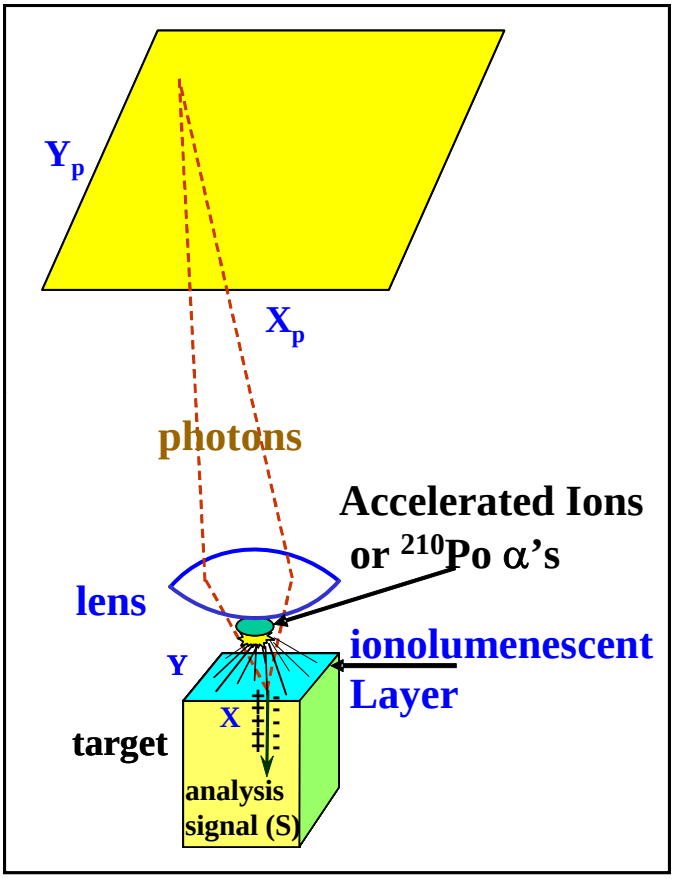


**Figure 1.** A schematic of the IPEM operating principle. The ion beam from a radioactive source or accelerator is placed as the target. The sample can be in either vacuum or external to the ion-source vacuum. Then, a very thin fluorescent film is placed over the DUT surface. This film produces one or multiple simultaneous photons in response to the passage of each incident ion from the source. These photons are then projected at high magnification through a conventional optical microscope onto a specialized, X-Y position-sensitive, single-photon-counting, microchannel-plate photon detector. Because this detector is single-event-counting, the event can be time-correlated with an upset event that may occur in the device under test (DUT). Spatial resolution (device spatial identification) is currently limited to approximately 1-2 micron FWHM. Between 50,000 and 100,000 detected ion strikes per second can be processed leading to relatively rapid data map development.

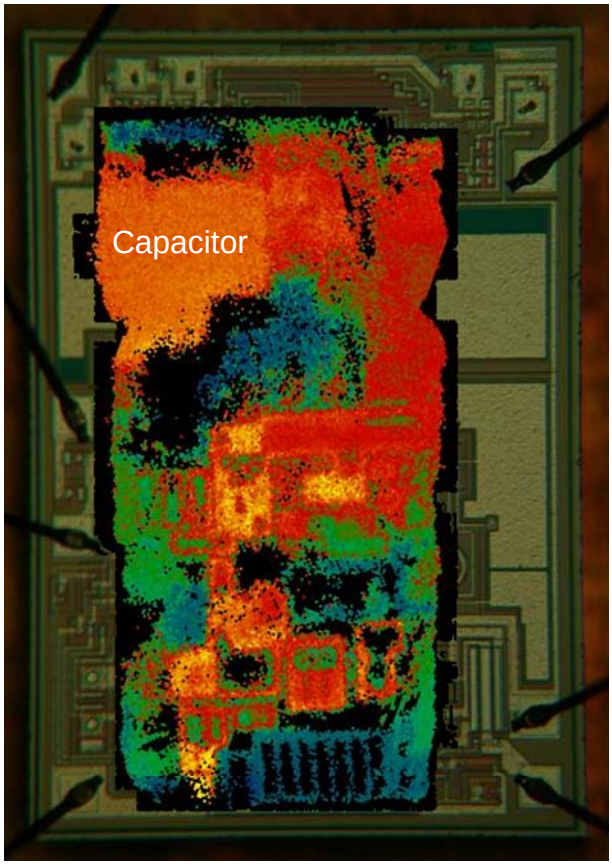


**Figure 2.** An example of IPEM-Ion Beam Induced Charge (IBIC) is shown in this figure, where the IBIC image is plotted on top of a photo of the die. This die is 2x3mm, and several IPEM-IBIC images were overlayed to produce this charge collection map. The sample is an operational amplifier that is being studied jointly with Lockheed Martin Corporation for Single Event Gate Rupture. While the alpha particles cannot induce a gate rupture, this IBIC image is useful to identify regions of high charge collection, and clearly identifies the large capacitors of the op amp, one which is labeled in the figure. The uniformity of the IBIC signal across these capacitors shows that they were manufactured correctly.

# *DLTS and Gain Measurements of Bipolar Transistors Following Ion Irradiation*

*by* **R. M. Fleming, C. H. Seager and D. V. Lang**

**Motivation**—As an alternative to testing at the Sandia Pulsed Reactor (SPR), now slated for shutdown, the QASPR program (Qualification Alternatives to SPR) has been initiated to model the time-dependent performance of devices and circuits following transient neutron irradiation. Experimental input to modeling will come from measurements of defects in the devices by deep-level transient spectroscopy (DLTS) and measurements of device performance. Data from a number of facilities will be used to establish damage equivalence between the alternate radiation sources and SPR.

**Accomplishment**—An apparatus has been constructed at the Ion Beam Lab that allows irradiation of devices at 35 K and the automated acquisition of DLTS, gain, and photocurrent data as the device is warmed. This apparatus will be replicated for use in other facilities such as the SPR. Since the time-dependence of device performance is desired and DLTS is not a real-time probe, the time dependence of the defect concentrations will be extracted from the temperature dependence of the DLTS signal following isochronal anneals. The initial studies will be on silicon bipolar transistors.

The first DLTS data from the ion-beam apparatus are shown in Fig. 1 where we plot the signal from the base/collector junction of a 2N2222 npn transistor following irradiation with 28 MeV $Si^{4+}$ ions. Ten-minute isochronal annealing temperatures as well as the energy levels of common silicon defects are indicated. A prominent, broad feature is seen in the range 140 – 240 K that corresponds to a distribution of states in the gap about 0.3 eV below the conduction band. Most of the broad feature anneals out by 300 K, but a shoulder remains to about 400 K. A second feature of these data is that the carbon interstitial peak appears only after annealing at 250 K, which is much later than expected. Since this peak arises from silicon interstitial motion, we can conclude that motion of the silicon interstitial is inhibited under the conditions of our experiment.

Gain measurements are shown in Fig. 2 where we show Gummel plots measured at 300 K. A recovery of gain is seen after the 550 K anneal, which is accompanied by the loss of DLTS signal from the shoulder mentioned above and from defects identified as vacancy-donor and perhaps boron interstitial. Since DLTS is most sensitive to defects in the base/collector and gain is strongly affected by defects in the base/emitter junction, a full understanding of the response of the transistor to defects will require measurements of both npn and pnp transistors.

**Significance**—Although defects in silicon have been extensively studied for three decades, these data represent several new aspects. First, the bulk of the previous data were on uniformly damaged silicon, typically using electrons. Here we concentrate on damage by neutrons or ions which are likely to produce clusters of defects as well as different species of defects. Second, the previous studies were done following room temperature irradiation, and the intermediate information on defect evolution was lost. Here, using a new and unique apparatus, we show the intermediate phases of defect evolution. Finally, unlike earlier work, we measure the defects in devices rather than test structures, and we can therefore correlate defect measurements with device performance.

**Sponsors for various phases of this work include:** Nuclear Weapons Program

**Contact:** Robert M. Fleming, Semiconductor Material & Device Sciences, Dept. 1123
Phone: (505) 284-8460, Fax: (505) 844-1197, E-mail: rmflemi@sandia.gov

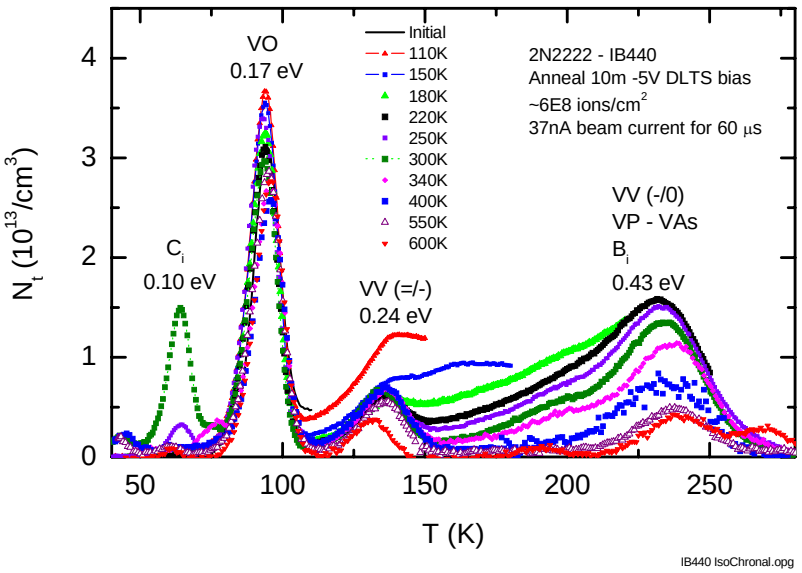


**Figure 1.** DLTS following 35K irradiation and 10 minute isochronal anneals at the temperatures indicated Energy levels referenced to the conduction band of common silicon defects are shown.

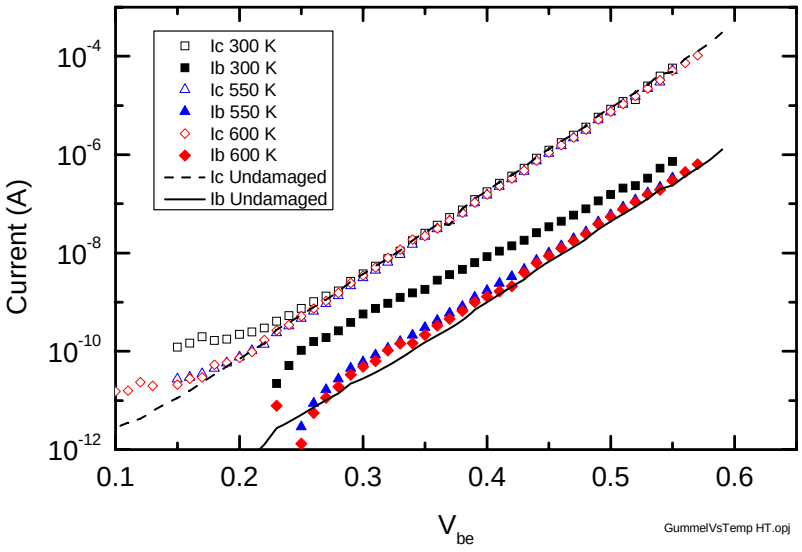


**Figure 2.** Base and collector current versus $V_{be}$ for an undamaged device and following 300, 550 and 600 K anneals. A significant gain recovery is seen after the 550 K anneal.

# *Modeling the Silicon Interstitial: Why the Self-interstitial is Invisible*

*by* **N. A. Modine and D. V. Lang**

**Motivation**—One of the most enduring mysteries in the field of semiconductor defects is to explain why no one has observed the isolated self-interstitial defect in silicon. This defect, along with the silicon vacancy, is one of the primary defects created in silicon material and devices by high-energy electrons, ions, or neutrons. However, numerous experiments over the past 50 years have failed to directly observe the silicon self-interstitial.

**Accomplishment**—We have applied our state-of-the-art computational capabilities to model the silicon self-interstitial, and our results explain why it has escaped direct detection for so many years. In p-type silicon, various indirect experiments suggest that the interstitial escapes detection because it is highly mobile at temperatures as low at 4.2K in the presence of ionizing radiation. This was qualitatively rationalized many years ago by the so-called Bourgoin-Corbett mechanism of athermal defect migration. Figure 1 shows our calculated diffusion coefficient as a function of temperature in p-type material with varying rates of electron-hole recombination at the defect. Our calculations identify a specific mechanism of athermal diffusion that is a modification of the standard Bourgoin-Corbett mechanism. This process results in the temperature invariance of our calculated diffusion coefficient at low temperatures or high ionization levels.

In n-type silicon, we can explain why the self-interstitial defect has also escaped detection, in spite of indirect evidence that athermal motion is not taking place. It is known by observing the creation of carbon interstitials from mobile silicon interstitials via the well-known "kick-out" mechanism that silicon self-interstitials do not move in n-type material until at least 150-175K. Thus one might expect the self-interstitial to be observable by Electron Paramagnetic Resonance (EPR) or Deep-Level Transient Spectroscopy (DLTS) experiments below this temperature. However, in spite of numerous attempts, this important defect has remained invisible. Figure 2 shows our stability results for various charge states and configurations of the self-interstitial as a function of Fermi energy. Two important and previously unrecognized properties of the silicon interstitial are predicted. First, the silicon self interstitial is "negative-U" or very nearly "negative-U" for both positive and negative charge states, i.e., only charge states with pairs of electrons or holes trapped at the defect are likely to occur in significant populations. The absence of unpaired spins explains the negative results of EPR experiments. Second, there is a wide region of stability of the $2^-$ charge state below the conduction band edge, and the defect moves at a temperature lower than the DLTS peak corresponding to thermal emission of trapped electrons. Thus the silicon self-interstitial is not observed in a DLTS spectrum, in agreement with numerous negative results. This is an interesting property of the defect, since it implies that—unlike most other defects—there is a lower thermal barrier for moving the defect than there is for emitting a trapped carrier.

**Significance**—All of these predicted properties that explain the "invisible" nature of the silicon interstitial are key metrics that give us confidence in the accuracy of our defect modeling capabilities that are critical inputs to the Qualification Alternatives to Sandia Pulse Reactor (QASPR) project.

**Sponsors for various phases of this work include:** Nuclear Weapons Program

**Contact:** Normand A. Modine, Nanostructure & Semiconductor Physics, Dept. 1112
Phone: (505) 844-8412, Fax: (505) 844-1197, E-mail: namodin@sandia.gov

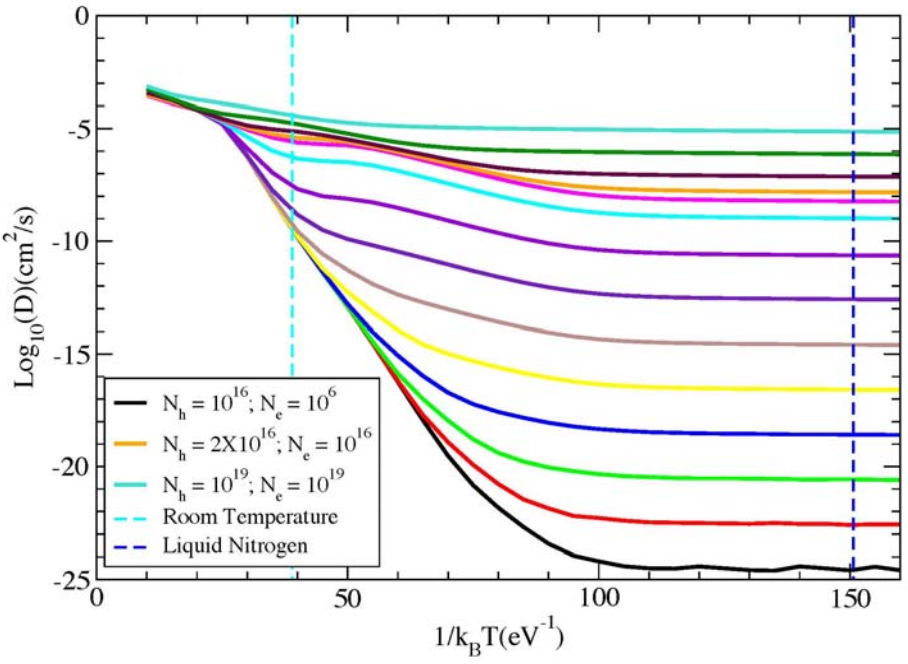


**Figure 1.** Diffusion coefficients as a function of inverse temperature obtained by incorporating diffusion barriers calculated using the Local Density Approximation (LDA) to the Kohn-Sham Density Functional Theory into a Kinetic Monte-Carlo simulation. Results are for a non-equilibrium p-type system with $10^{16}$ ionized acceptors and a variable number of additional electron-hole pairs.

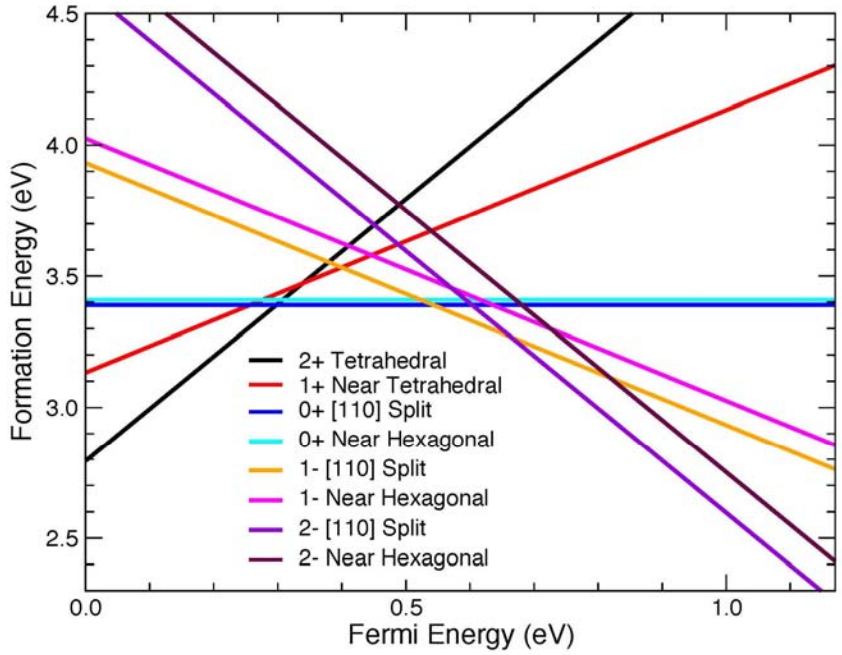


**Figure 2.** Thermodynamic stability diagram obtained from LDA calculations. The electronic Fermi energy is referenced to the valence band edge. The charge and configuration of the interstitial with the lowest formation energy is thermodynamically stable at a given Fermi energy.

# *Science-Based Modeling of Pulse-Irradiated Transistors in the QASPR Program*

*by* **S. M. Myers and W. R. Wampler**

**Motivation**—Impending shutdown of the Sandia Pulse Reactor (SPR-III) will require that electronics be qualified for fast-transient neutron irradiation by using alternative experimental facilities less representative of potential threat environments. QASPR (Qualification Alterna-tives to Sandia Pulse Reactor) was initiated in Oct. 2005 to establish the required new qualification protocols. Success will hinge upon the development of substantially improved, science-based models for neutron-irradiated Si bipolar devices that can bridge the greater gap between testing and threat conditions. This is challenging due to the numerous defect reactions occurring within irradiated Si and the fact that neutrons produce atomic displacements in clusters. In the present effort, we are carrying out modeling calculations to explore the defect behavior and its influence on bipolar devices, and are thereby determining how the physics will ultimately be implemented in QASPR models.

**Accomplishment**—Silicon bipolar transistors exposed to neutron irradiation were modeled using a new, 1-D finite-element code. The transistor base was treated by an approximation whereby the potential and majority-carrier concentration – but not the minority-carrier concentration – are constrained along a plane within the neutral region of the base. Explicit account was taken of the formation of vacancies (charge states -2,-1,0,+1,+2) and Si interstitials (-2,-1,0,+1,+2), their migration and field-drift, their recombination, and their reactions to form VV(-2,-1,0,+1), $B_I$(-1,0,+), VB(0,+1), VP(-1,0), VO(-1,0), $B_I$B(-1,0), $B_I$O(0,+1), and $C_I$(-1,0,+1). Here V is the vacancy, the subscript I denotes interstitial atoms, and P, B, O, and C are the dopants and principal impurities.

Figure 1 shows the time-dependent base current computed for a commercial N-P-N transistor (Microsemi 2N2222) exposed to a pulse of MeV neutrons in the fast-burst reactor at White Sands Missile Range. This calculation captures the principal features of the device response, including a positive photocurrent during the irradiation pulse that falls off as defect recombination centers accumulate; a subsequent negative current caused by electron-hole recombination at the defects; and a drop-off in the latter current arising from defect annealing.

The consequences of defect formation in clusters (not included above) were examined using a second new finite-element code. This program again included the aforementioned defect processes, but now treated a sub-micrometer sphere of Si containing a cluster, with radial symmetry assumed. These calculations reveal two key effects of the clustering: first, reactions among the vacancies and interstitials are much more rapid due to their proximity; and, second, local electrostatic fields (band-bending) arising from defect charging in the cluster alter the rates of capture for conduction electrons and holes. The latter effect is illustrated in Fig. 2, which shows how the steady-state flow of carriers into the defect-containing volume differs between the cases of clustered and randomly dispersed divacancies. Means of including these clustering effects in the device model are under investigation.

**Significance**—These exploratory calculations, along with comparisons to experiment, are providing the basis for design of the defect-physics package that will ultimately be used in QASPR device models.

**Sponsors for various phases of this work include**: Nuclear Weapons Program

**Contact:** Samuel M. Myers, Nanostructure & Semiconductor Physics, Dept. 1112
Phone: (505) 844-6076, Fax: (505) 844-7775, E-mail: smmyers@sandia.gov

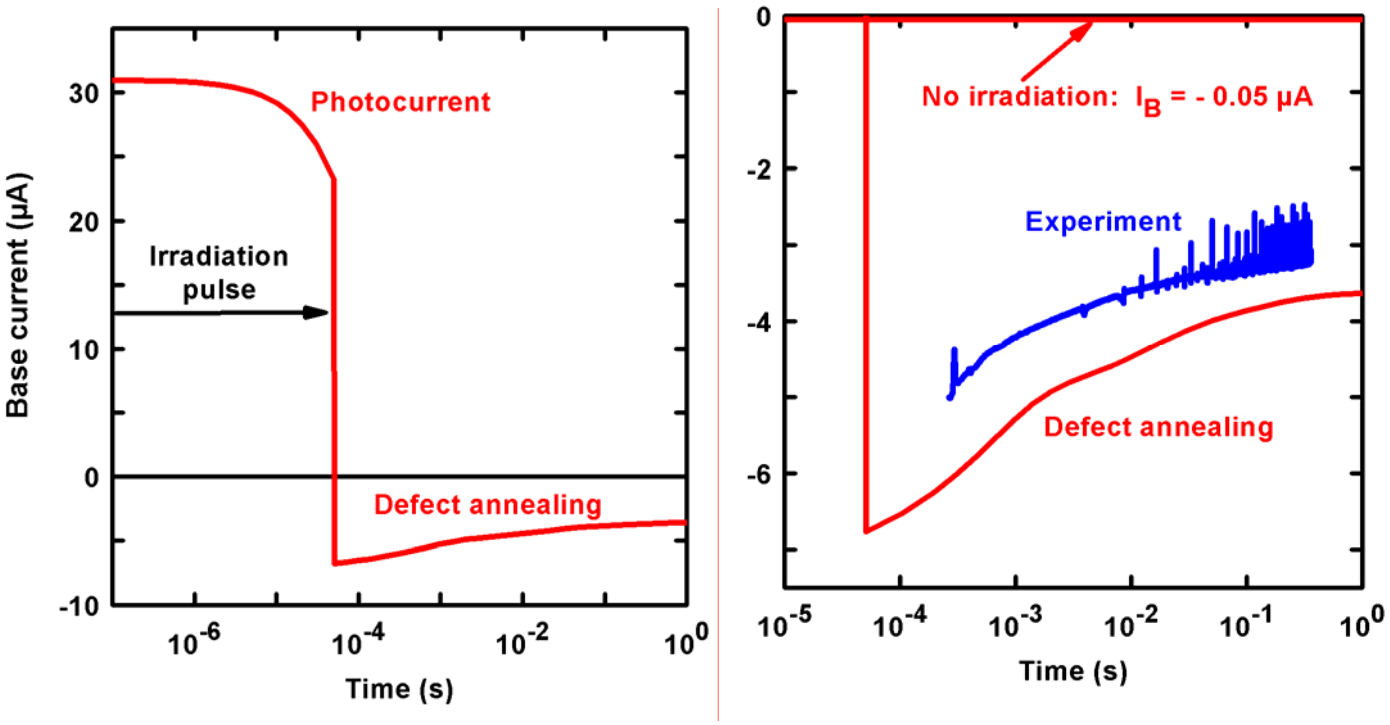


**Figure 1.** Model-predicted base current versus time (in red) for a Si N-P-N bipolar transistor subjected to a 50-μs burst of $6\times10^{13}$ neutrons/cm$^2$ with $V_{EB}$ = 0.5 volts and $V_{BC}$ = 3.0 volts. The right-hand panel is expanded from the left. (The poorly known carrier-capture cross sections for the neutral vacancy were equated to $10^{-14}$ cm$^2$ for better agreement with experiment.)

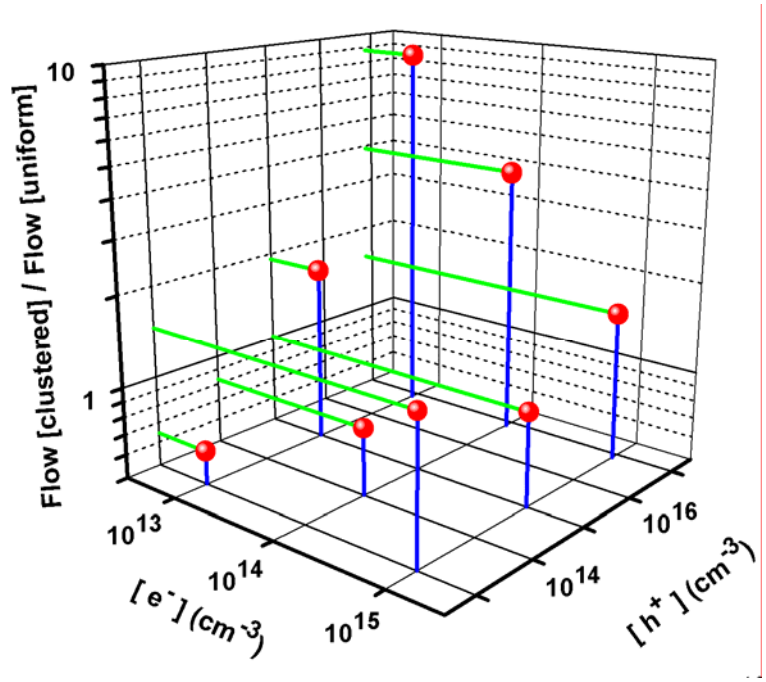


**Figure 2.** Ratio of carrier annihilation rates by a constant number of divacancies with and without clustering, for a range of local conduction-electron and hole concentrations typical of an operating N-P-N transistor. The clustering increases the local defect concentration by ×8000.

# *Strain Fields Around the Tracks of High-Energy Ions in Quartz*

*by* **D. M. Follstaedt, A. K. Norman, B. L. Doyle and F. D. McDaniel**

**Motivation**—Ion beam treatments modify the properties of materials, usually producing little change in dimensions, <~1 μm. However, irradiation of amorphous films by high energy ions can change lateral film dimensions by 10's of percent. Models based on local expansion of rapidly heated material along the ion path (called a "thermal spike") are being developed to explain the phenomenon. The expansion is modeled as straining the matrix around molten track centerline, which is the microscopic basis for the lateral expansion. Amorphous $SiO_2$ (a-$SiO_2$) is a widely studied prototype material that is being understood with the models. While latent ion tracks can be identified in a-$SiO_2$ by transmission electron microscopy (TEM), strain is not readily detected in amorphous materials. Thus, a critical part of the models has not been experimentally verified.

**Accomplishment**—We have examined the tracks of 374 MeV $^{197}Au^{26+}$ and 241 MeV $^{127}I^{18+}$ in α-quartz with TEM. Quartz has the same $SiO_2$ composition but has a hexagonal crystal structure. These high-energy ions transfer large amounts of energy to electrons along their tracks, 24 and 19 keV/nm, respectively, which are sufficient to produce melting and form amorphous latent track centerlines. We have found strain fields around the tracks with symmetry and lateral extent like those expected when amorphous $SiO_2$ is fitted with the model.

The high-energy ions were produced with the tandem accelerator and sent into the radio-frequency quadrupole booster in Sandia's Ion Beam Materials Research Laboratory to increase their energies to 1.9 MeV/amu. Thinned quartz specimens were irradiated and examined by TEM with low beam intensities to minimize damage. Higher ion fluxes were obtained for $^{127}I^{18+}$ beams to produce a dense array of tracks as seen in Fig. 1. Tracks are more readily identi-fied by tilting the specimen to view their projected length, as shown. The oscillatory contrast along the track is due to the strain in the matrix around the amorphous centerline. Figure 2a shows a $^{197}Au^{26+}$ track with the strain extending radially 16 nm beyond the amorphous centerline, which is 4 nm in radius. Radial strain is expected to extend several times the centerline radius from the expansion model.

The strain contrast changed in images taken with other diffraction conditions. Whereas in Fig. 2a the diffraction vector has a component orthogonal to the track projection, Fig. 2b was obtained with the diffraction vector parallel to the projection. In this case, the contrast does not extend as far outward and is also present along the centerline. When considered within TEM contrast theory, these differences are consistent with radial strain around the track centerline. Our findings with several diffraction vectors taken together imply cylindrical symmetry around the centerline for the radial strain, as assumed in the expansion model.

**Significance**—Energy transfer to electrons, track melting, and elastic response of the matrix are similar in quartz and a-$SiO_2$, however the amorphous phase expands less on melting. Nonetheless, finding strain fields with the expected properties in such a closely related crystalline phase provides an additional experimental basis for confidence in the modeling of the expansion of a-$SiO_2$. Amorphous track centers had been found in quartz, but strain around them was not reported.

**Sponsors for various phases of this work include:** Laboratory Directed Research & Development

**Contact:** David M. Follstaedt, Radiation-Solid Interactions, Dept. 1111
Phone: (505) 844-2102, Fax: (505) 844-7775, E-mail: dmfolls@sandia.gov

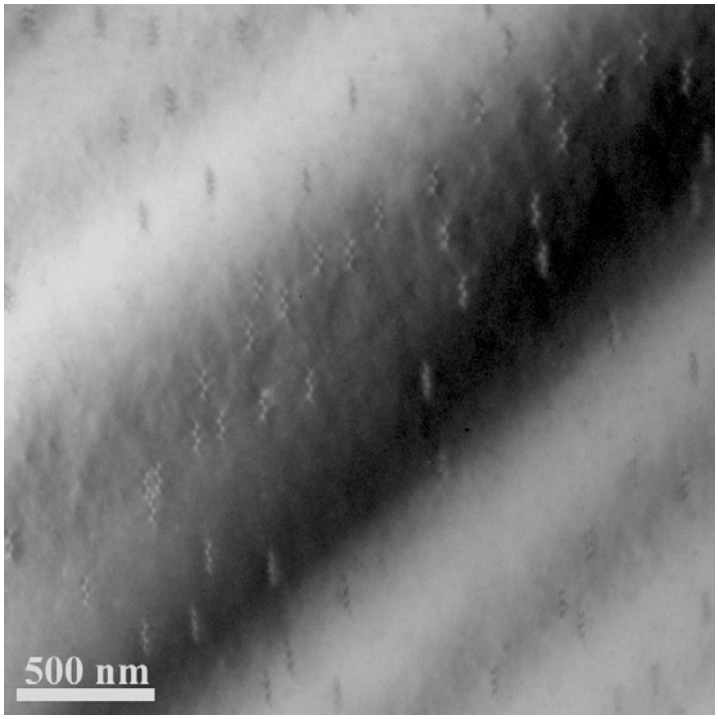


**Figure 1.** Bright-field TEM image of 241 MeV $^{127}$I tracks in α-quartz, obtained at 300 kV using **g** = (11-20) diffraction conditions with the specimen tilted 13º from normal. (Our thanks to P. Kotula, 1822, for assistance with images taken at 300 kV.)

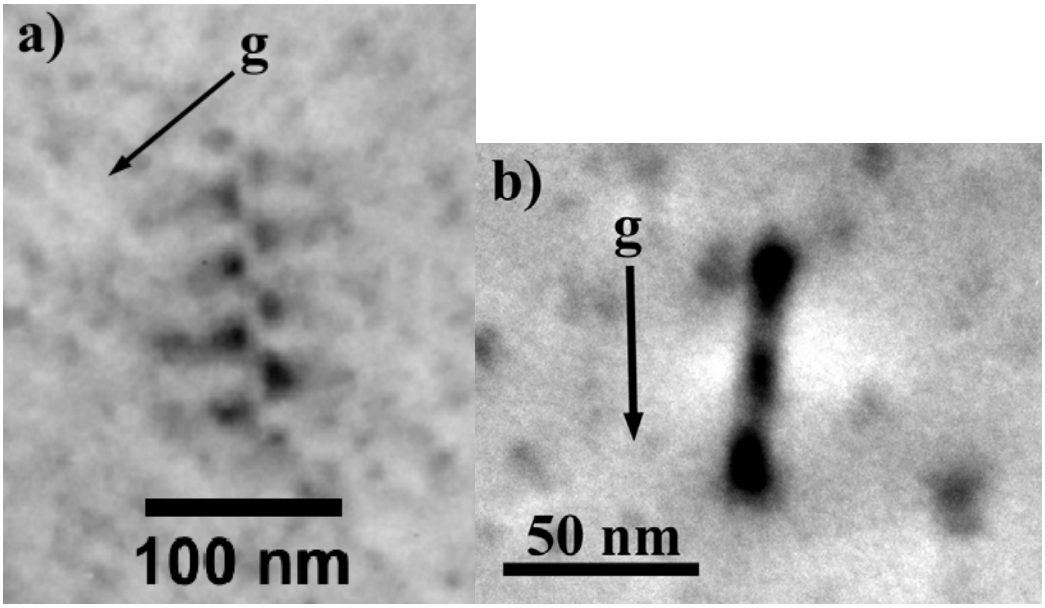


**Figure 2.** a) Bright-field TEM image of 374 MeV Au track in α-quartz, obtained at 200 kV with **g** = (1-100) diffraction conditions and the specimen tilted 35°. b) Bright-field image of 374 MeV Au track, obtained at 200 kV but with the diffraction vector parallel to projected track length. Note the 2x enlargement of b); the lateral width of contrast in b) is therefore narrower than that in a). In addition, the contrast in b) lies along the track centerline whereas that in a) has a clear centerline.

# *Theory of Charge Induction in MOS Structures*

*by* **G. Vizkelethy, D. K. Brice, and B. L. Doyle**

**Motivation—**Silicon-On-Insulator (SOI) circuits have been considered less sensitive to single event effects (SEE) than devices made using bulk technology. It was believed in the past that charge is collected only from the active layer above the buried oxide (BOX) but not from the substrate below the BOX. Recently, as the BOX thickness decreased significantly SOI SRAMS were found to be more sensitive to SEE than expected. Model experiments showed that there is significant charge collection from below the BOX. Here we present an analytical model based on the Gunn-theorem to describe ion induced charge collection in MOS (Metal-On-Semiconductor) devices.

**Accomplishment—**At first we have to emphasize that although the term "charge collection" is widely used it is incorrect. Charge is never collected but rather induced. When a high energy heavy ion hits a device electron-hole pairs are generated. Those electron-hole pairs that were created in a fielded region (such as a p-n junction) start drifting apart and will induce charge on the electrodes of the device. A fraction of the electron-hole pairs that were created in a field free region will eventually diffuse to the fielded region and will drift through it. According to the Gunn-theorem the current induced by a moving charge $q$ on the $i^{th}$ electrode of the device is $I_i = -q\mathbf{v}\,\partial\mathbf{E}/\partial V_i$ where $\mathbf{v}$ is the velocity of the moving charge $\partial\mathbf{E}/\partial V_i$ and is the differential of the electric field with respect to the voltage on the $i^{th}$ electrode while the voltage is kept constant on all the other electrodes. Applying the Gunn-theorem and the basic equations of electrostatics it can be shown that the induced charge in and MOS capacitor is

$$\frac{q_c}{q_d} = \frac{\lambda/\varepsilon_{Si}}{\lambda/\varepsilon_{Si} + x_{ox}/\varepsilon_{ox}} \text{ with } \lambda = \langle x \rangle + Q \cdot \partial \langle x \rangle / \partial Q$$

where $Q$ is the total charge per unit area, $<x>$ is the distance from the oxide-substrate interface averaged over the charge distribution. An MOS capacitor can be in three states. In accumulation, when the majority carriers pile up the interface, in depletion when fixed impurity atoms are ionized creating a depletion layer, and in inversion where the depletion layer width is saturated and minority carriers pile up at the interface. From the above equation it is obvious that $\lambda$ is significantly different from zero only in the depletion and inversion regime; therefore, we can expect charge collection in these regimes only as the experiments showed. Figures 1 and 2 show the dependence of the charge collection on the bias and BOX thickness measured with IBIC (Ion Beam Induced Charge) and calculated using the above model. The calculated curves qualitatively agree with the measurements, but they reach saturation at much lower biases than the experimental ones. It might be due to the trapped interface charge and the charge accumulating during at the interface during the charge collection process. These will be included later in the model.

**Significance**—SOI promises devices less sensible to SEE than those made using bulk technology. It is important to understand how the ion induced charge collection works in these devices. The above analytical model provides and easy and fast way to calculate the collected charge in MOS structures.

**Sponsors for various phases of this work include:** Nuclear Weapons/Readiness in Technical Base & Work for Others/Facilities and Defense Threat Reduction Agency

**Contact:** Gyorgy Vizkelethy, Radiation-Solid Interactions, Dept. 1111
Phone: (505) 284-3120, Fax: (505) 844-7775, E-mail: gvizkel@sandia.gov

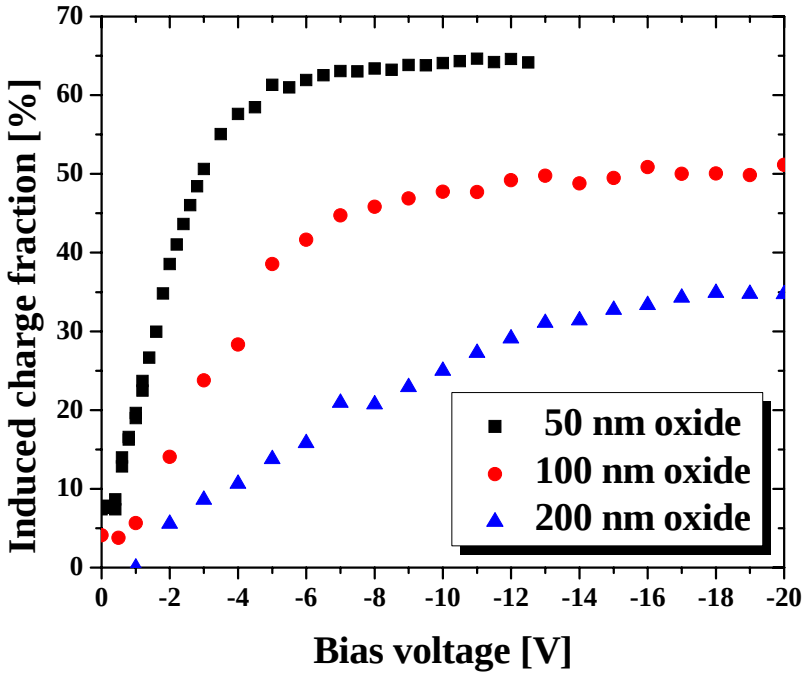


**Figure 1.** Measured induced charge fraction using IBIC.

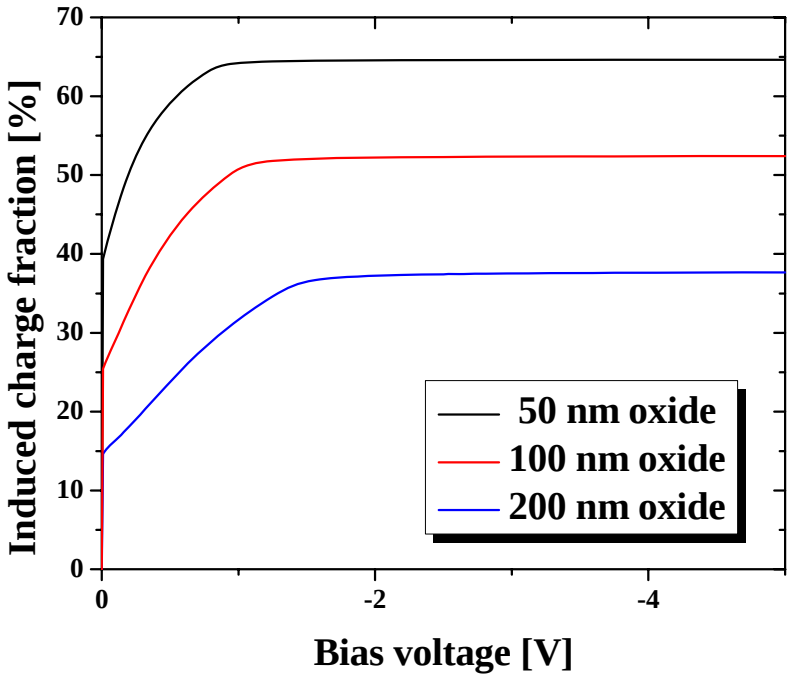


**Figure 2.** Calculated induced charge fraction.

# *Carbon Transport and Deposition in Tokamaks*

*by* **W. R. Wampler**

**Motivation**—Carbon-based materials are commonly used for plasma facing components in tokamaks because of their ability to survive high transient heat loads. However, chemical erosion of such materials by the fusion plasma produces hydrocarbons which dissociate in the plasma boundary and redeposit elsewhere onto the vessel wall. In tritium fueled tokamaks, codeposition of tritium with carbon can lead to large inventories of retained tritium. Models to simulate erosion, transport and deposition are needed for design of fusion reactors and their operating conditions, which will avoid excessive tritium retention. However, the complexity of the physical processes necessitates experiments in tokamaks to guide the model development.

**Accomplishment**—Such experiments are being conducted at the DIII-D tokamak in San Diego in a collaboration between Sandia and General Atomics. $^{13}CH_4$ is injected into lower single null plasmas as illustrated in Fig. 1. This plasma geometry, and location of injection far from the divertor, were chosen to simulate methane originating from plasma interactions with the graphite main chamber wall. Graphite tiles were subsequently removed and analyzed at Sandia to determine the spatial distribution of $^{13}C$ deposition. $^{13}C$ coverage was measured using $^{13}C(^{3}He,p)^{15}N$ nuclear reaction analysis. The experiment has now been conducted twice, the first time with low power low density (L-mode) plasmas and more recently with high power high density (H-mode) plasmas. These measurements show the $^{13}C$ is deposited primarily at the divertor as shown in Fig. 2, with much lower $^{13}C$ coverage elsewhere (not shown), though analysis of tiles outside the divertor region is still in progress for the second experiment. $^{13}C$ deposition at the inner divertor is similar for these two plasma conditions. Between the two strike points, deposition was low for L-mode but high for H-mode plasmas.

**Significance—**The results show that methane entering the plasma from the main chamber wall is not redeposited near its point of origin, as some models predicted, but instead is ionized and carried by the plasma to the divertor. The observed asymmetry between deposition at inner and outer divertors indicates that carbon is swept towards the inner divertor by a fast flow in the plasma boundary.

The difference in deposition between L-mode and H-mode results from the different plasma conditions in the divertor. With L-mode the divertor plasma is detached (low temperature, high density) at the inner leg but attached (high temperature, low density) at the outer leg. With H-mode the region of detached plasma includes both inner and outer legs of the divertor. Carbon deposition evidently occurs from detached divertor plasma, whereas erosion dominates where plasma is attached.

These results have important implications for the next large fusion energy research device, the International Thermonuclear Experimental Reactor (ITER). The single-null detached H-mode plasmas in DIII-D are similar to proposed ITER plasma conditions. Detached plasmas were chosen to reduce erosion and heat flux in the ITER divertor. The results from the DIII-D $^{13}C$ injection experiments suggest that in ITER, hydrocarbons from the main chamber would deposit in the divertor contributing to the in-vessel tritium inventory. The choice to use a metal wall in ITER's main chamber will greatly reduce the rate of hydrocarbon production and hence reduce the rate of tritium retention thereby allowing more efficient use of tritium and extending the operational life of the device.

**Sponsors for various phases of this work include**: DOE Office of Fusion Energy Sciences

Contact: William R. Wampler, Radiation-Solid Interactions, Dept. 1111
Phone: (505) 844-4114, Fax: (505) 844-7775, E-mail: wrwampl@sandia.gov

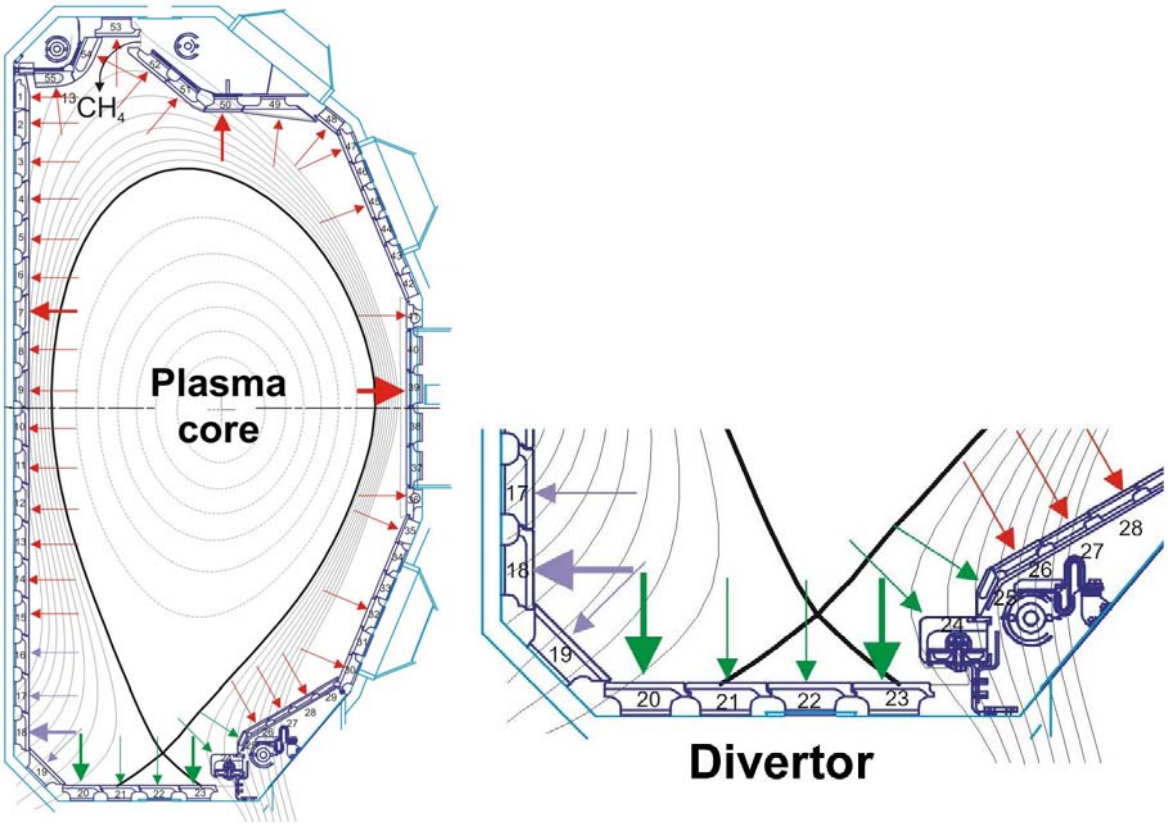


**Figure 1.** Diagram of the DIII-D tokamak with lower single null plasma configuration. $^{13}CH_4$ is injected at the top of the main chamber. The heavy black line shows the last closed magnetic flux surface. Boundary plasma flows along outer field lines which intersect surfaces in the divertor.

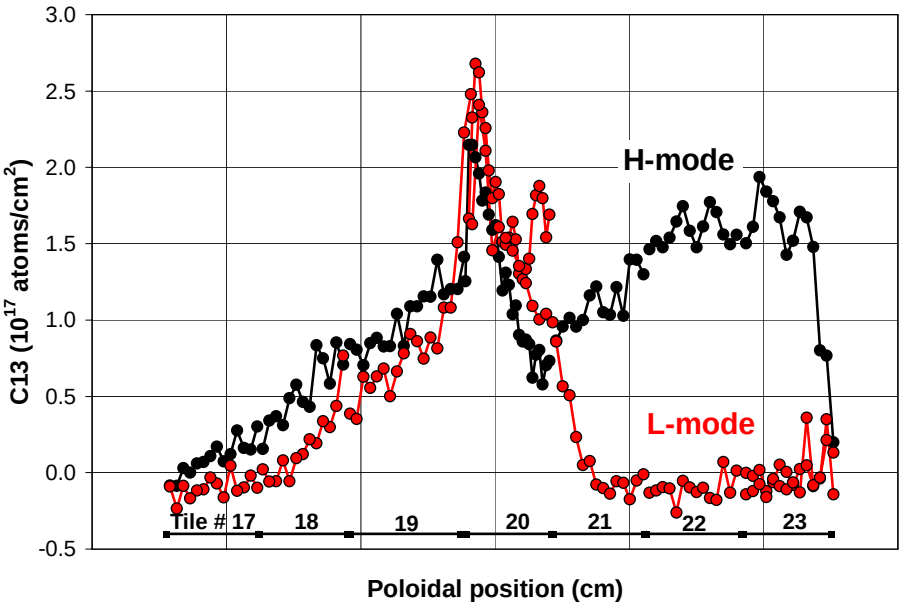


**Figure 2.** Measured coverage of carbon 13 in the divertor region.

# *Shock Studies to Optimize ALOX Encapsulants*

*by* **R. E. Setchell, S. T. Montgomery, M. U. Anderson, and D. E. Cox**

**Motivation—**Alumina-filled epoxy (ALOX) is used as an encapsulant in explosively driven pulsed power supplies. The shock loading experienced by the active elements in these devices, and consequently the overall device performance, is strongly influenced by the shock compression and release properties of the encapsulant. Previously we examined these properties in a specific, baseline composition. This material, which contains 43% by volume alumina particles, displays a complex behavior which includes unusually high release-wave velocities (Fig. 1). Our recent studies have examined ALOX materials with modified compositions with the goal of optimizing shock properties for encapsulation applications. To date we have examined changes in the alumina volume fraction, the alumina particle size and shape, and the host epoxy.

**Accomplishment—**To obtain useful insights using a minimum number of gas gun experiments, each composition was examined in a 1-D, symmetric-impact configuration at a fixed impact velocity. This provided a compressive wave profile, Hugoniot properties, and a release-wave velocity for each material at states of equal particle velocity, corresponding to nearly equal states of strain. Only minor differences were seen when the alumina volume fraction was held constant while varying the alumina particle characteristics and the host epoxy. Significant differences were seen when the alumina fraction was lowered in steps from the 43% baseline value down to 0%. Figure 2 shows measured shock and release velocities as functions of the alumina volume fraction. The release velocity decreases faster than the shock velocity with decreasing alumina, thus the ratio of these velocities decreases as well. This ratio is a measure of how rapidly downstream unloading events can overtake and attenuate a leading shock wave, which can be important in encapsulation applications. This trend was examined in more detail using the configuration shown in Fig. 3. In these 1-D "thin pulse" experiments, impactor and target dimensions were chosen to allow a release wave to overtake and attenuate the impact-generated shock wave before it can reach the window interface. The impactor material and dimensions, the impact velocity, and the target dimensions were held constant while the alumina fraction was varied in the target ALOX samples. Figure 4 shows the results of these experiments. In addition to the transmitted wave profiles, the figure lists the predicted impact stress and the measured average wave velocity for each case. Even though the impact stress decreased significantly as the alumina fraction was decreased, the peak particle velocity of the wave transmitted into the window progressively increased. The reduction in release velocity more than compensates for the reduced impact stress, with the transmitted wave experiencing less attenuation.

**Significance**—The initial symmetric-impact experiments examined how basic shock compression and release properties vary with ALOX compositional changes. The rapid reduction in the ratio of release and shock velocities as alumina fraction was decreased prompted additional "thin pulse" experiments. These experiments showed a surprising and important effect of alumina volume fraction in an encapsulant required to transmit a shock wave to a second material following a fixed, short-duration input stimulus. Reducing the alumina volume fraction appears to be a useful way to optimize ALOX shock properties.

**Sponsors for various phases of this work include:** Nuclear Weapons/Science & Technology

**Contact:** Robert E. Setchell, Radiation-Solid Interactions, Dept. 1111
Phone: (505) 844-3847, Fax: (505) 844-4045, E-mail: resetch@sandia.gov

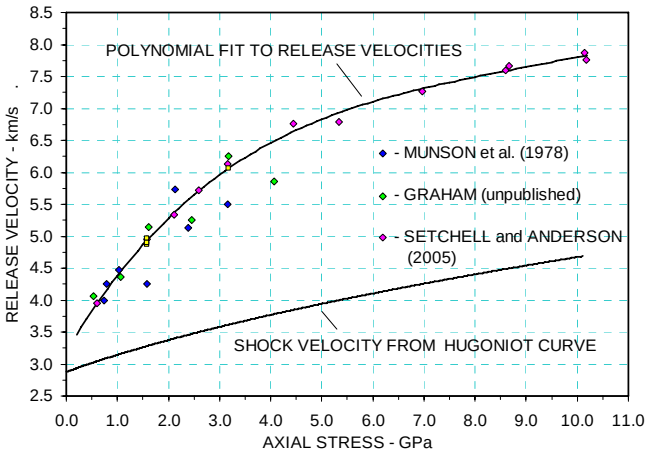


**Figure 1.** Baseline ALOX velocities for shock waves and release waves as functions of axial stress in the shocked state.

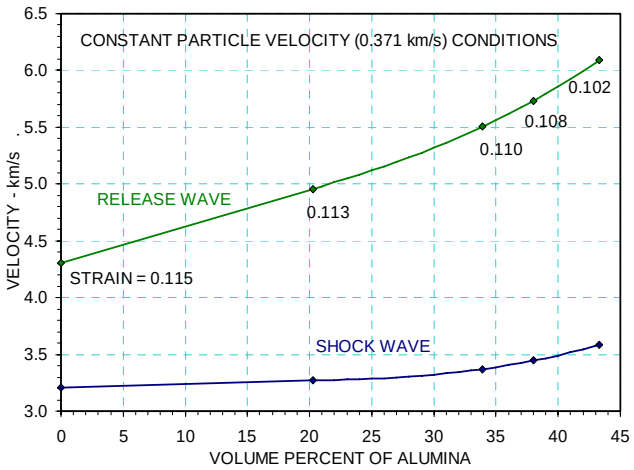


**Figure 2.** Velocities for shock waves and release waves as a function of the alumina volume fraction. All data are for a shocked state having a fixed particle velocity, corresponding to nearly equal states of uniaxial-strain.

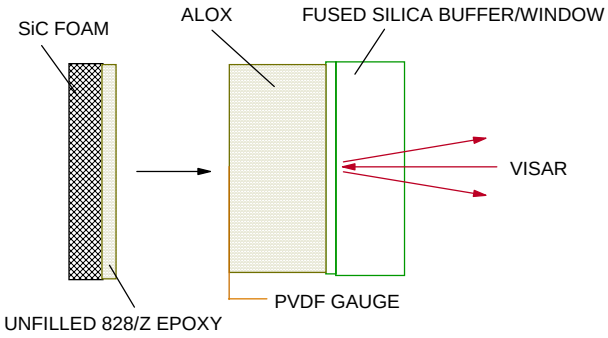


**Figure 3.** Configuration used for "thin pulse" uniaxial-strain experiments on ALOX.

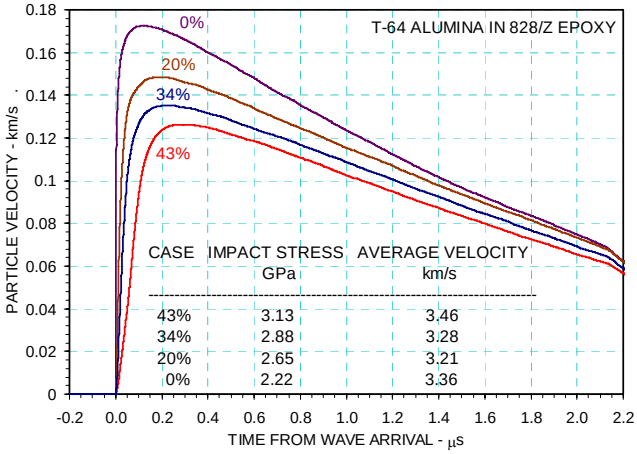


**Figure 4.** Wave profiles recorded in ALOX "thin pulse" experiments for materials with different alumina volume fractions. The impact velocity in every experiment was 1.05 km/s.

# Recent Awards & Prizes

# Recent Awards & Prizes

## National and International Awards

2005 — **American Academy of Arts and Sciences Election:** "For outstanding contributions in her profession." (Julia Phillips)

2004 — **National Academy of Engineering (NAE) Election:** "For leadership and distinguished research in the epitaxy of dissimilar materials." (Julia Phillips)

2003 — **National Associate of the National Academies (NAS, NAE, Institute of Medicine, NRC):** Awarded for "extraordinary service to the National Academies." (Julia Phillips)

2002 — **Plasma Prize for Science and Technology** presented by the American Vacuum Society, Plasma Science and Technology Division, for innovative development of diagnostics and insightful fundamental studies of low temperature plasmas and their successful application to the advancement of plasma technologies. (Greg Hebner)

— **National Academy of Engineering (NAE) Election**: For originating the field of strained-layer superlattices and related structures, which has led to revolutionary advances in electronics and optoelectronics." (Gordon Osbourn)

## DOE Basic Energy Sciences, Material Science Awards

2002 — **BES "Chunky Bullet Shootout":** Winner for "Ultrasensitive Chemical Sensors for Counter Terrorism Applications." (Jim Martin and Bob Anderson)

## Other Awards

2005 — **R&D100 Award:** "For the development of Ion Photon Emission Microscope (IPEM)." (Barney L. Doyle, Michael Mellon, Floyd D. McDaniel, and Paolo Rossi)

— **Materials Research Society (MRS) "Science as Art" Competition First Prize Award:** "For Garden of ZnO Nano-Yuccas." (Julia Hsu, Tom Sounart, Neil Simmons, Jom Boigt, and Jun Liu)

2004 — **American Vacuum Society (AVS) Fellow Appointment:** "For developing innovative optical, microwave, and electrical diagnostics of plasma sources." (Greg Hebner)

— **Optical Society of America (OSA) Fellow Appointment:** "For contributions to the field of nonlinear optics." (Arlee V. Smith)

— **R&D100 Award**: "Cantilever Epitaxy and Growth of Low-Dislocation Gallium Nitride." (Inventors: C. I. H. Ashby, D. M. Follstaedt, C. C. Mitchell and J. Han; Developers: A. A. Allerman, K. H. A. Bogart, K. Cross, A. J. Fischer, K. Fullmer, L. Griego, D. D. Koleske,

N. A. Missert, M. P. Moran, A. K. Norman, A. Ongstad, G. M. Peake, P. Provencio and J. Sergeant)

— **Wilbur Lucius Cross Medal Recipient** – highest award of the Yale University Graduate School Alumni Association: Cited for "scientific achievements, leadership in research management, outstanding service to the nation, and inspiration as a role model for young women in science and engineering." (Julia Phillips)

2003 — **2003 President's Silver Quality Award:** "Weapon Program Phase 7 Process Development" Team. (David Walsh)

— **APS Fellow Appointment:** Elected Fellow of the American Physical Society (APS) "for his pioneering and continued contributions to the metal-organic chemical vapor deposition of compound semiconductors, especially strained layer superlattices and Bragg reflectors for use in optoelectronic devices for industrial applications." (Bob Biefeld)

— **AAAS Fellow Appointment:** Elected Fellow of the American Association for the Advancement of Science (AAAS) for his "research advances, particularly the development and exploitation of interfacial force microscopy, leading to fundamental understanding of the interaction of solid surfaces with the environment." (Jack Houston)

— **Humboldt Research Award** for early experimental research on electrical discharge excimer lasers and for recent accomplishments on the microscopic theory of semiconductor lasers. (Weng Chow)

2002 — **APS Fellow Appointment:** Elected Fellow of the American Physical Society (APS) "for pioneering work in applying scanning probe microscopy techniques to elucidate the nanometer scale electronic and optical properties of novel materials – in particular the physics related to defect." (Julia Hsu)

— **AAAS Fellow Appointment:** Elected Fellow of the American Association for the Advancement of Science (AAAS) for her "seminal research on growth and properties of magnetic, superconducting, and optical thin films and for leadership in the management of interdisciplinary research." (Julia Phillips)

— **APS Fellow Appointments:** Elected Fellows of the American Physical Society (APS) for:

— contributions to the fundamental understanding of the gas-phase and surface chemical processes in the chemical vapor deposition of semiconductor materials. (Michael E. Coltrin)

— outstanding contributions to the physics of tunneling in two dimensional electronic materials, including fractional quantum Hall and double quantum well systems. (Jerry A. Simmons)

— pioneering studies of atomic-scale, kinetic, and thermodynamic aspects of the morphology of Si surfaces and significant innovations in scanning tunneling microscopy. (Brian S. Swartzentruber)

— **Horizon Award** presented by the New Mexico Commission on the Status of Women and the U. S. Department of Labor Women's Bureau: The recipient of this award must be a New Mexico resident who has contributed significantly to the acceptance and advancement of women in Science, Math, Engineering, and Technology. (Julia Phillips)

— **Humboldt Research Award** in recognition of research accomplishments in the area of polymer modeling, which will be used to further collaborations with colleagues in Germany. (Gary Grest)
— **Publication in "All Star" collection** of 25 significant and most cited articles that appeared in ECS journals since 1940. (M. E. Coltrin, R. J. Kee, and J. A. Miller)
— **Sandia Fellow Appointment**: By distinguishing himself and Sandia through his technical novations in several very important fields, including strained-layer technology, the application of biological vision and pattern recognition systems to computer-based sensor systems, and collective intelligence and self-organizing systems. (Gordon Osbourn)
— **Weapon Award of Excellence**: The CY 2001 Weapons Award of Excellence winners included two teams at Sandia Laboratories led by Center 1100:
  — (1) The Neutron Tube Production R&D Team for applying scientific tools and methods to improve yield and reliability of Neutron Tubes. (Paul A. Miller, Team Lead, et al.)
  — (2) The Photonic Driver Team for developing a Photonic Driver capability for microscale shock wave physics research. (Bob Setchell, Team Lead, et al.)

## Patents Awarded

**2005**

**— Patent 6,866,560**
Title: Method for Thinning Specimen
Originator: David M. Follstaedt and Michael P. Moran
**— Patent 6,844,378**
Title: Method of Using Triaxial Magnetic Fields for Making Particle Structures
Originator: James E. Martin, Robert Anderson, and Rodney Williamson

**2004**

**— Patent 6,790,476**
Title: Strong Adhesion and Wetting of Metals to Oxide Surfaces
Originator: Dwight Jennison
**— Patent 6,775,314**
Title: Distributed Bragg Reflector Using AlGaN/GaN
Originator: Stephen Lee
**— Patent 6,775,054**
Title: Image Rotating 4-Mirror Ring Optical Parametric Oscillator
Originator: Arlee Smith and Darrell Armstrong
**— Patent 6,718,821**
Title: Multi-Axis Force-Feedback Sensor with Laser Interferometer Displacement Detection
Originator: Jack Houston

**— Patent 6,627,048**
Title: Laser Interferometry Force-Feedback Sensor for an Interfacial Force Microscope
Originator: Jack Houston and William L. Smith

**2003**
**— Patent No. 6,665,329**
Title: Broadband Visible Light Source Based on ALLNGAN Light Emitting Diodes
Originator: Mary H. Crawford
**— Patent No. 6,647,034**
Title: Method To Improve Optical Parametric Oscillator Beam Quality
Originator: Arlee V. Smith
**— Patent No. 6,647,033**
Title: Optical Parametric Oscillators with Improved Beam Quality
Originator: Arlee V. Smith, and William J. Alford
**— Patent 6,627,048**
Title: Reductive Precipitation of Metals Photosensitized by Tin and Antimony Porphyrins
Originator: John A. Shelnutt
**— Patent 6,608,846**
Title: Bistable Laser with Multiple Coupled Active Verticle-Cavity Resonators
Originators: Arthur J. Fischer, Weng W. Chow, Kent D. Choquette
**— Patent 6,600,761**
Title: Semiconductor Laser with Multiple Lasing Wavelengths
Originators: Arthur J. Fischer, Weng W. Chow, Kent D. Choquette
**— Patent 6,599,362**
Title: Substrate Texturing for Cantilever Epitaxy of III-N and Other Materials
Originators: Carol I. Ashby, Christine C. Mitchell, David M. Follstaedt, Jung Han (Yale University)
**— Patent 6,570,333**
Title: A Method for Generation of Surface Plasma Using Radio-frequency Power Across Pairs of Insulator Conductors where the Plasma Can Cover a Variety of Flat or Curved Surfaces, such as Aircraft Surfaces in High-altitude Flight Operation
Originators: Paul A. Miller, Ben P. Aragon
**— Patent 6,567,454**
Title: Coupled-resonator Vertical-cavity Lasers with Two Active Gain Regions
Originators: Arthur J. Fischer, Weng W. Chow, Kent D. Choquette
**— Patent 6,552,338**
Title: Ion Photon Emission Microscope
Originators: Barney L. Doyle
**— Patent 6,504,859**
Title: Light Sources Based on Semiconductor Current Filaments
Originators: Weng Chow, et al.
**— Patent 6,479,919**
Title: Solid-state Nuclear-to-electric Energy Conversion: Beta-voltaic Cells of Icosahedral Borides
Originators: Terrence L. Aselage, David Jacob Emin

**— Patent 6,406,931**
Title: Conductivity Control of GaN Using LT AIN Buffer Layers
Originators: Jeffrey J. Figiel, Jung Han (Yale University)

**2002**
**— Patent 6,406,931**
Title: Conductivity Control of GaN Using LT AIN Buffer Layers
Originators: Jeffrey J. Figiel, Jung Han
**— Patent 6,393,038**
Title: Frequency-doubled Vertical External Cavity Surface Emitting Laser
Originators: William J. Alford, Mary H. Crawford, Andrew A. Allerman, Thomas D. Raymond
**— Patent 6,391,393**
Title: Nonvolatile, Dual Level, Magnetic Storage Media
Originators: James E. Martin, Chris P. Tigges, Robert A. Anderson, Eugene L. Venturini
**— Patent 6,375,759**
Title: Batch Fabrication of Precision Miniature Permanent Magnets
Originators: Terry J. Garino, Eugene L. Venturini, Todd R. Christenson
**— Patent 6,365,428**
Title: Buried Distributed Bragg Reflector for Planar Waveguide Applications
Originators: Walter J. Zubrzycki, Gregory A. Vawter, Andrew A. Allerman

# Government Advisory Boards & Professional Societies/International Committees/Journals

## Government Advisory Boards

**Argonne National Laboratory**
— Materials Science Division External Review Committee; Julia Phillips, Chair; 2003

**Department of Energy, Office of Basic Energy Sciences**
— Scientific User Facilities Division Committee of Visitors; Julia Phillips, member; 2004
— Review of Nanoscience Research Center Operational Plans; Julia Phillips, member; 2004
— Materials Sciences and Engineering Program Committee of Visitors; Julia Phillips, member; 2003
— Workshop on Issues in Nanomechanics; Charles Barbour, Panel Chair; 2003

**Lawrence Berkeley National Labs (LBNL) Committee**
— Accelerator and Fusion Research/Directors Review Committee; Barney Doyle, member; 2003

**National Academy of Engineering**
— U. S. Frontiers of Engineering Program: Julia Phillips, Chair, 2005-2008; Mary Crawford, participant, 2005; Julia Hsu, participant, 2003
— Draper Prize Committee; Julia Phillips, member; 2005-2007

**National Research Council**
— Board on Physics and Astronomy; Julia Phillips, member; 2000-2006
— National Materials Advisory Board; Julia Phillips, Chair; 2002-2004
— Review Panel, State of Ohio Centers of Innovation; Neal Shinn, member; 2004
— U.S. Liaison Committee for the International Union of Pure and Applied Physics; Julia Phillips, member; 2000-2002
— Committee on Materials Research for the Defense-After-Next; Julia Phillips, member; 1999-2002

**National Science Foundation**
— Advisory Committee, Mathematics and Physical Sciences Directorate; Julia Phillips, member; 2000-2003

## Professional Societies/International Committees/Journals

**American Association for the Advancement of Science (AAAS)**
— Council; Julia Phillips, member; 2003-2005
— Physics Section Nominating Committee: Julia Phillips, member, 2003-2004; Chair, 2005
— Physics Section; Julia Phillips: Chair-elect, Chair, Past Chair; 2003-2005

**American Association for Crystal Growth**
— 15th American Conference on Crystal Growth and Epitaxy; Bob Biefeld, Co-chair; 2002

**Air Force Office of Scientific Research (AFOSR)**
— Plasma-assisted Combustion AFOSR Review Panel; Greg Hebner and Paul Miller, members; 2004

## Professional Societies/International Committees/Journals Cont'd

**American Physical Society (APS)**
— Division of Condensed Matter Physics (DCMP): Julia Phillips, Vice-Chair, 2005; Chair-Elect, 2006; Chair, 2007
— Forum on Industrial & Applied Physics (FIAP): Mark Lee, Vice-Chair, 2005; Chair-Elect, 2006; Chair, 2007
— Committee on Meetings; Mark Lee, member; 2003-2006
— Maria Goeppert Mayer Award Committee; Julia Phillips, Chair; 2002
— Division of Materials Physics (DMP) Executive Committee; Julia Hsu, Member-at-Large; 2004-2006
— March Meeting; Brian Swartzentruber, Symposium Organizer; 2004

**American Vacuum Society (AVS)**
— 53rd International Symposium; Neal Shinn, Vice Chair; 2006
— Distinguished Lecture Series Committee; Neal Shinn, Chair; 2004-2006
— Board of Directors; Neal Shinn, member; 2003-2006
— 39th Annual Meeting of the New Mexico Chapter; Kate Bogart, Symposium Chair; 2003
— Chapters, Divisions, Groups Committee; Neal Shinn, member; 2002-2004
— Surface Science Division; Neal Shinn, Chair; 2001-2002

**American Society for Microbiology (ASM) International**
— Events Committee; Dan Barton, member; 2003-present
— Electronic Device Failure Analysis Society (EDFAS): Dan Barton, Board of Directors member, 1998-present; Vice-President, 2005

**Army Research Office (ARO) Multi University Research Initiative (MURI)**
— Technical Advisory Committee; Mark Lee, member; 2001-2002

**Electrochemical Society**
— Symposium; Nancy Missert, Organizer; 2006
— Individual Membership Committee; Nancy Missert, member; 2003-2006
— Student Travel Grant, Corrosion Division; Nancy Missert, Coordinator; 2005-2006
— Nash Miller Award Committee; Nancy Missert, member; 2005

**Gaseous Electronics Conference (GEC)**
— 56th Annual Meeting; Greg Hebner: Chair-elect, Chair, Past Chair; 2003-2006

**Industrial and Professional Advisory Council for the Engineering Science and Mechanics Department at Penn State University**
— Neal Shinn, member; 2003-2006

**Institute of Electrical and Electronics Engineers (IEEE)**
— Transactions on Plasma Science, 4th issue on Images in Plasma Science; Greg Hebner, Guest Editor; 2004-2005

## Professional Societies/International Committees/Journals Cont'd

— Transactions on Device and Materials Reliability (TDMR); Dan Barton, Guest Editor; 2002 - present
— International Reliability Physics Symposium; Dan Barton, Management Committee member; 2001-present

**International Conference on Defects in Semiconductors**
— Alan Wright; International Advisory Board, Co-organizer; 2005-2007

**International Conference on Ion Beam Analysis**
— Gyorgy Vizkelethy and Barney L. Doyle, Chairmen; 2003
— International Committee; Gyorgy Vizkelethy and Barney L. Doyle, members; 2003

**International Conference on Nuclear Microscopy Technology and Applications**
— International Committee, Barney L. Doyle; 1990-2004

**International Journal of PIXE (IJPIXE)**
— Editorial Board, Barney Doyle; 1996-present

**International Union for Vacuum Science, Technique, and Applications (IUVSTA)**
— Surface Science Electoral College; Neal Shinn, United States Representative; 2001-2007
— Surface Science Division: Neal Shinn, Chair, 2004-2007; Secretary, 2001-2004
— Surface Science Program, 16th International Vacuum Congress; Neal Shinn, Program Committee member; 2004

**Ion Beam Modification of Materials Conference**
— International Committee; Charles Barbour, member; 1996-present

**Journal of Chemical Physics**
— Jim Martin, Editorial Board; 2003-2006

**Journal of Crystal Growth**
— Bob Biefeld, Associate Editor for the Journal of Crystal Growth for subject areas: "Epitaxial Growth and Nanostructures"; 2004-2006

**Journal of Vacuum Science and Technology**
— Neal Shinn, Associate Editor; 2002-present

**Materials Research Society (MRS)**
— Board of Directors: Jerry Floro, member, 2002-2004; Julia Hsu, member, 2005-2007
— Membership Committee: Sean Hearne, member, 2004-2006; Charles Barbour, Chairman, 2001-present
— Membership Web Advisory Committee; Sean Hearne, member; 2005-2006
— Electronic Services Task Force; Sean Hearne, member; 2005

## Professional Societies/International Committees/Journals Cont'd

— External Relations and Volunteer Involvement (ERVI) Committee; Jerry Floro, Chair; 2004
— Task Force on Meeting Program/Board of Directors Interactions; Julia Phillips, Chair; 2003
— Task Force on Government Agencies Committee; Charles Barbour, member; 2002
— Meetings: Charles Barbour, Chair, Spring 2006; Julia Hsu, Chair, Fall 2004
— Symposium: Neal Shinn, Organizer, Spring 2006; John Sullivan, Organizer, Spring 2006; Sean Hearne, Organizer, Fall 2002

**Microelectronics Reliability (Elsevier Journal)**
— Editorial Advisory Board; Dan Barton, member; 2000 - present

**NASA Review Panel**
— Bob Biefeld, member; 2002

**New Mexico State University**
— Alan Wright, Physics Advisory Board member; 2002-2004

**Nuclear Instruments and Methods in Physics Research, Section B: Beam Interactions with Materials and Atoms**
— Barney Doyle, Editorial Board; 2003-2006

**Physical Review E**
— Gary Grest, Senior Editor; 2002-present

**Radiation Effects in Insulators Conference**
— Charles Barbour, International Committee member; 1997-present

**Solid State Communications**
— Julia Hsu, Editorial Board; 2005-present

**The Minerals, Metals, and Materials Society (TMS)**
— Electronic Materials Committee; Julia Hsu, member; 2000-2006
— Electronic Materials Committee: Bob Biefeld, member, 2002-present; Secretary, 2002-2004

**Twelfth International Conference on Metal-Organic Vapour Phase Epitaxy**
— Bob Biefeld, Organizing Committee member; 2002

**US-Organometallic Vapor Phase Epitaxy Workshop**
— Bob Biefeld, Organizing Committee member; 2002

# Resources & Capabilities

# Resources & Capabilities
# Physical, Chemical, & Nano Sciences Center

## — Diagnostics and Characterization —

### Atomic-Level Imaging and Spectroscopy

We have developed technical capabilities in:

- Atomic Force Microscopy (AFM) for imaging, force profiling, electrical measurements, and manipulation of individual biomolecules in fluid environments with simultaneous fluorescence detection,
- Atom Probe Microscopy (APM) with pulsed laser desorption capability,
- Field Ion Microscopy (FIM) with single atom resolution and accurate temperature control to 1 Kelvin,
- Interfacial Force Microscopy (IFM) with feedback for accurate, simultaneous normal and frictional force profile measurements for the quantitative study of adhesion, tribology, and nanomechanics,
- Low Energy Electron Microscopy (LEEM) with nanometer spatial resolution and real-time spectroscopic imaging capability at sample temperatures from 300K to over 1000K,
- Piezo Force Microscopy (PFM) for measuring piezoelectric coefficient, imaging ferroelectric domains, and spatial variation in piezoelectric properties, and
- Scanning Tunneling Microscopy (STM) with the ability to track the diffusion of single atoms on surfaces.

### Chemical Vapor Deposition (CVD)

Our experimental tools for investigating CVD include optical probes (such as reflectance-difference spectroscopy and emissivity correcting pyrometry) for gas-phase and surface processes, a range of surface analytic techniques, molecular beam methods for gas/surface kinetics, and flow visualization techniques. These tools are integrated in a unique manner with research CVD reactors and with advanced chemistry and fluid models.

### Electrochemical Scanning Probe Microscopy

We have developed the ability to study nanoscale changes at surfaces during oxidation and dissolution of metal surfaces under electrochemical control using scanning tunneling microscopy. These studies can be performed in a variety of electrolytes in order to determine the mechanisms governing passive film growth.

### Growth Science Laboratory

Capabilities for in situ characterization of materials during thin film deposition, molecular beam epitaxial growth, and low energy ion beam simulated growth, include intensity profile sensitive reflection high energy electron diffraction (RHEED) for surface structure, energy dispersive x-ray reflectrometry for in situ surface and interface structure, multibeam wafer curvature for strain, and Auger electron spectroscopy for surface composition.

### Ion Accelerator Nuclear Microprobe

We have facilities for nuclear microscopy and radiation effects microscopy based on a 6 MV tandem Van de Graaff ion accelerator. We generate ion species from hydrogen to gold for both radiation effects research and quantitative high-energy ion beam analysis of materials containing light elements (hydrogen to fluorine) using heavy ion elastic recoil detection (ERD) and heavy elements using high-energy backscattering spectrometry, and Heavy Ion Backscattering (HIBS). An external Micro Ion Beam Analysis (X-MIBA) capability enables multi-elemental analysis and ion irradiation of samples, which are vacuum incompatible or extraordinarily large. The Sandia Nuclear Microprobe with micrometer size high-energy ion beams is

used to study materials and devices. Special emphasis is given to the evaluation of the radiation hardness of microelectronic devices using three new advanced diagnostic techniques invented at Sandia: Single-Event-Upset Imaging, Ion-Beam-Induced-Charge-Collection Imaging (IBICC), and time-resolved IBICC. A recent development is the Ion Electron Emission Microscope (U. S. Patent No. 6,291,823 and 2001 R & D-100 Award winner), which can perform radiation microscopy using very highly ionizing particles without focusing the ion beam.

### KMAP X-ray Diffractometer

Based on double crystal x-ray diffractometry in combination with position sensitive x-ray detection, our KMAP x-ray diffraction analysis is used to determine the lattice constant, strain relaxation, composition, layer orientation, and mosaic spread for a large variety of advanced epitaxial semiconductor material systems.

### Laser and Optical Spectroscopies

Our capabilities in characterizing semiconductor materials by photoluminescence and magnetoluminescence extend down to low temperatures by optical laser imaging and laser microscopy, by laser excitation spectroscopy, and by the time-resolved measurements of optical emission. We also have developed a high lateral resolution, near-field scanning optical microscopy (NSOM) capability with time and frequency resolution.

### Lasers and Optics

We provide characterization and advanced understanding in the area of solid-state lasers and non-linear optics, especially as coherent sources of broadly tunable light in rugged, compact geometries. We also have established expertise in long-term and transient radiation effects characterization of optical materials. Capabilities include the widely used (approximately 2000 users worldwide) SNLO (Sandia Non-Linear Optics) code, which is a lab-tested code for predicting the performance of non-linear optical components. In the area of integrated optical materials, our laboratories produce new types of photosensitive materials (processing patent applied for) for directly-writeable waveguides and reconfigurable optical interconnects.

### Low-Temperature Plasma Analysis

We have state-of-the-art capabilities for the analysis of low-temperature plasmas as found in commercial processing reactors. These include emission spectroscopy, electrical characterization, laser and microwave-based measurements of species concentrations, in situ electric field measurements, and others. Sandia is the only lab that combines new diagnostics, relevant process chemistries (complex mixtures), and massively parallel (MP) computer models for simulation of continuous and transient plasmas.

### Materials Microcharacterization

Our capabilities in this area include optical microscopy, scanning, electron microscopy, analytical transmission electron microscopy, double crystal x-ray diffraction, ion beam analysis of materials (RBS, channeling, ERD, PIXE, NRA), Hall measurements, microcalorimetry, photoluminescence, light scattering, electronic transport, deep level spectroscopy, magnetization, and dielectric and magnetic susceptibilities.

### MEMS-based Tensile Testing

We have developed the capability to perform pure uni-axial loading of metal MEMBS test structure in situ and ex situ of a TEM. The technique has been demonstrated using Al, Ni and Cu, but is applicable to a wide range of other materials.

### Nanoelectronics Laboratory

We have the capabilities for fabrication of nanoscale quantum device structures, together

with capabilities for ultra-low-noise measurement of transport from 0.3 Kelvin to ambient at high magnetic fields.

### Scanning Cathodoluminescence Microscopy

We have developed the ability to measure and image cathodoluminescence from insulators and semiconductors on the submicron scale in order to understand how defects influence the emission of light from the ultraviolet to the visible. Individual spectra are also obtained at controlled locations in order to identify heterogeneities.

### Scanning Probe Metrology

We have developed a unique wide-field scanning Interfacial Force Microscope with calibrated force detection for the dynamic measurement of normal and lateral forces of micro-electrical-mechanical system components in operation.

### Simultaneous Measurement of H, D, and T in Materials

We have designed and implemented a new ion beam analysis (IBA) system to simultaneously measure the absolute quantities of H, D, and T in materials using an elastic recoil detection (ERD) technique. The technique uses an E-dE detector arrangement, or particle telescope, to provide for accurate separation of the H, D, and T signals. The system can also simultaneously acquire information about medium and high Z elements in the sample using Rutherford backscattering spectrometry (RBS). Measurement of other light elements is possible using the nuclear reaction analysis (NRA) technique, which is isotope specific. The system will have an accuracy of $< 2\%$ for measuring the composition of solids.

### Vision-Science Laboratory

The vision science laboratory consists of state-of-the-art hardware and software capabilities for carrying out video inspection, multi-spectral image analysis, and sensor-based pattern recognition. These capabilities are used in applications ranging from microsensor-based chemical detection and recognition to automated video/SEM inspection of semiconductor materials and circuits. This is a new approach to pattern recognition, coupling perception-oriented research with machine algorithms.

## — Synthesis and Processing —

### 400 keV and 180 keV Ion Implanters

These systems are equipped with a variety of sources (gas, sputter, and metal vapor). This facility provides ion species from hydrogen to bismuth that can be used for studying fundamental irradiation mechanisms and selective chemical doping in semiconductors, metals, ferroelectrics and superconductors. The 180 keV Implanter is capable of both ambient and high temperature implants up to 600°C and ion currents up to 50 micro-A.

### Biomaterials Laboratory

The Biomaterials Laboratory possesses equipment to perform numerous molecular biology and biochemistry research including genomic DNA, RNA, and plasmid isolation from a variety of sources (e.g., bacteria, viruses, and eukaryotic tissues and ells). DNA sequences can be cloned into a variety of organisms, permitting the manipulation and modification of DNA and protein sequences, structure, and function. Cloned DNA sequences can be genetically engineered using reverse transcription, the polymerase chain reaction and site-directed mutagenesis. Native and recombinant proteins also can be expressed, purified, characterized, and functionalized in this laboratory.

### Crystal and Thin Film Growth

Capabilities in this area include pulsed laser deposition chambers, a high vacuum metal deposition chamber, a thin film oxide deposition chamber, a diamond-like carbon deposition chamber, a hot filament chemical vapor deposition chamber, and various apparatus for single

crystal growth. Our capabilities for stress relief of diamond-like carbon films and structures produced by pulsed laser deposition are not available elsewhere.

### Electron Cyclotron Resonance (ECR)

This plasma facility has been built for studying fundamental processes governing the growth of oxide and nitride dielectric films used in optoelectronics and used as hard coatings. This is the only system in the U.S., which combines ECR plus e-beam evaporation.

### High Pressure and Shock Wave Physics and Chemistry Laboratories

Our capabilities in this area include large volume static high pressure apparatus which can be operated at temperatures ranging from 2 to 700 K and in magnetic fields, as well as gas gun and explosive loading facilities with state-of-the-art, time-resolved diagnostics. Recovery fixtures have been developed for use with the gas gun and explosive shock loading facilities that allow unique material synthesis over broad ranges of shock pressures and temperatures.

### Metal-Organic Chemical Vapor Deposition (MOCVD)

We maintain research facilities with capabilities in MOCVD of III-V compound semiconductor materials including GaN-based materials and self-assembled quantum dots. These capabilities include research reactors designed specifically for studies of CVD chemistry, fluid dynamics, the development of advanced in situ diagnostics, and the development of advanced semiconductor heterostructures and devices.

### Molecular Beam Epitaxy (MBE)

We have research semiconductor growth laboratories for ultra-pure and ultra-flexible MBE growth of III-V materials. In addition, we have research systems for Group IV semiconductor growth.

### Monolayer Deposition of Organic Films

We have a Langmuir-Blodgett facility for controlled deposition of mono- and multi-layer organic films. The facility includes two computer-controlled troughs, in situ fluorescence microscopy, vibration isolation, and a dust-free down flow work area.

### Nanocluster Laboratory

We have developed and patented a process based on the use of inverse micelles for the synthesis of large quantities of monodisperse clusters of metals, semiconductors, and oxides.

### Soft Nanolithography

Soft nanolithography refers to patterning techniques that complement UV and electron beam lithography. These approaches avoid the chemical and radiation exposure often used in conventional lithography processing, making soft nanolithography particularly useful for bio, organic, and molecular materials. Current capabilities include micro-contact printing, nanotransfer printing, and dip-pen nanolithography.

### Stress Evolution During Electrodeposition

We have developed the capability to measure stress evolution during thin film electrodeposition and have used it to measure stress during patterned and unpatterned film growth. Our studies range from fundamental mechanisms that create stress during island coalescence to materials-specific systems, such as electrodeposited Ni, Cu, Sn, Ag and their alloys.

### Synthetic Organic Laboratory

Novel lipids, surfactants, and other small molecules are prepared in this laboratory via synthetic organic techniques. The laboratory is also capable or forming and characterizing self-organized structures (e.g., liposomes, micelles, self-assembled monolayers, LB films) generated with the newly synthesized molecules in pure or mixed molecular systems.

## — Theory and Simulation —

### Chemical Processes

We have extensive capabilities, including massively-parallel computation, to model complex chemically reacting flows such as occur in chemical vapor deposition manufacturing processes. Our numerical simulations can include the coupled gas-phase and gas-surface chemistry, fluid dynamics, heat, and mass transfer to provide predictive models of a chemical process.

### Electronic Structure and Linear Scaling

We have developed state-of-the-art massively parallel electronic structure algorithms, based on ab initio pseudopotentials and plane-wave/Gaussian basis functions. These codes are used to develop a fundamental understanding of physical phenomena and materials, including compound semiconductor band structure, diffusion of point defects, dopants and impurities, optoelectronic properties of extended defects, adsorbate interactions on surfaces, bonding at metal-oxide interfaces, and enhanced reactivity of nanoparticles. To allow the investigation of more complex systems and phenomena, we have developed new computationally efficient algorithms, e.g., self-consistent linear scaling density functional theory and variable and real-space gridding.

### Low-Temperature Plasmas

We have extensive capabilities in massively parallel codes to simulate the time and space evolution of low-temperature plasmas, focusing on new theoretical techniques for achieving rapid convergence and on direct comparisons with experimental results.

### Molecular Dynamics Simulation

Large scale, classical molecular dynamics simulations using the massively-parallel code LAMMPS (Large-scale Atomic/Molecular Massively Parallel Simulator) are being used to model a wide variety of systems. These classical simulations cover the length and time scale intermediate between quantum and continuum calculations. Systems of current interest include adhesion and friction in self-assembled monolayers, degradation of polymer adhesives, wetting and spreading of multi-component fluids and transport in polymer membranes for fuel cells. Modifi- cations of the algorithm to include particle rotation and friction have been implemented to study granular materials.

### Optical and Wave Propagation

We have developed advanced simulation codes for understanding wave propagation in optical parametric oscillators and amplifiers for the purpose of designing highly efficient, tunable laser sources. We also have capabilities in novel optical designs, including resonators for compact laser geometries. These capabilities are coupled to in-house micro-optics construction facilities and state-of-the-art optics testing.

# Physical, Chemical, & Nano Sciences Center - FY05 Budget

# Physical, Chemical, & Biomolecular Sciences Center FY04 Budget - By Customer

## Capital ($1.6M)

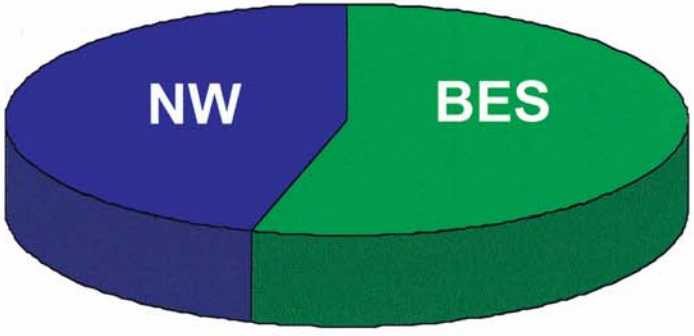


## Operating ($36.9M)

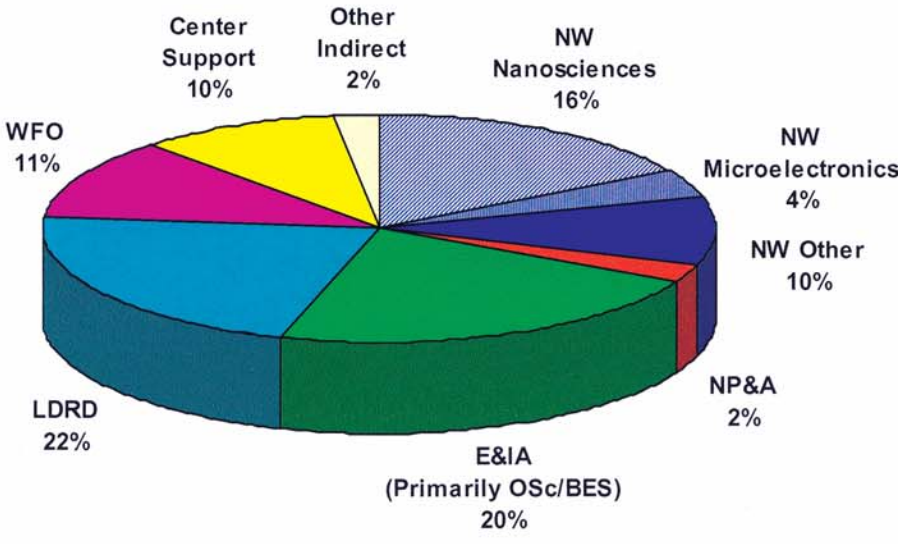


| | | | | | | | |
|---|---|---|---|---|---|---|---|
| NW | Nuclear Weapons | NP&A | Nonproliferation & Assessments | E&IA | Energy & Infrastructure Assurance | OSc | Office of Science |
| BES | Basic Energy Sciences | LDRD | Laboratory Directed Research & Development | WFO | Work for Others | | |

**SAND2005-XXXXP**: *Research Briefs* for the Physical, Chemical, & Nano Sciences Center is published by Sandia National Laboratories, a multiprogram laboratory operated by Sandia Corporation, a Lockheed Martin Company, for the United States National Nuclear Security Administration and the Department of Energy under Contract DE-AC04-94AL85000.

Printed 2005